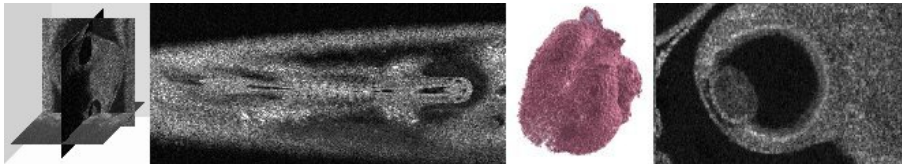




9TH MICCAI CONFERENCE

MICCAI Workshop on: Biophotonics Imaging for Diagnostics and Treatment

6 October, 2006



Bjarne Kjær Ersbøll
Thomas Martini Jørgensen (Editors)

Kgs. Lyngby 2006
IMM-TECHNICAL REPORT-2006-17



9TH MICCAI CONFERENCE

MICCAI '06
Workshop on Biophotonics Imaging
for Diagnostics and Treatment

October 6, 2006
Proceedings

Editors:

Bjarne Kjær Ersbøll
Thomas Martini Jørgensen

Sponsors:

Biophotonics Network, Denmark
BIOP Graduate School
Risø National Laboratory
Technical University of Denmark

Technical University of Denmark
Informatics and Mathematical Modelling
Building 321, DK-2800 Kgs. Lyngby, Denmark
Phone +45 45253351, Fax +45 45882673
reception@imm.dtu.dk
www.imm.dtu.dk

IMM-TECHNICAL REPORT: ISSN 1601-2321
ISBN: 87-643-0116-8

Preface

Biophotonics can be defined as the study of the interaction of light with biological material. With the recent advances in biomedical science, our understanding of the mechanisms of human health and disease has extended into the regime of cellular and molecular structure and function. The ability to image, analyze, and manipulate living tissue at this level (and to do so in a minimally- or noninvasive manner) has become essential for continued progress in biomedical research and development. Light is unique in that it can be utilized to perform exactly these functions; and as a consequence biophotonics is widely regarded as the basis for the next generation of clinical tools and biomedical research instruments.

With bioimaging the impact and amount of information contained in visual data is going to be huge. For this reason, imaging remains one of the most powerful tools in biomedical research.

Contents

- 1 Hyperspectral image analysis: Some applications in biotechnology and their prospective solutions
Mark Berman et al., CSIRO, Australia
- 7 Quantifying composition of human tissues from multi-spectral images using a model of image formation
Ela Claridge et al., School of Computer Science, The University of Birmingham, UK
- 15 Multispectral recordings and analysis of psoriasis lesions
Line H. Clemmensen and Bjarne Ersbøll, IMM, DTU, Denmark
- 19 Creating surface chemistry maps using multispectral vision technology
Jens Michael Carstensen et al., Videometer A/S, Denmark
- 29 Optical imaging of the embryonic heart for a better understanding of congenital heart defects
Talât Mesud Yelbuz, Dept. of Pediatric Cardiology and Intensive Care Medicine, Hannover Medical School, Hannover, Germany
- 33 Stereo reconstruction of the epicardium for optical fluorescence imaging
Desmund Chung et al., Department of Medical Biophysics, University of Toronto, Canada
- 41 Biomedical applications of terahertz technology
Vincent Wallace, Teraview, United Kingdom
- 43 The physical principles of chemical recognition in terahertz spectral imaging
Peter Uhd Jepsen and Stewart J. Clark, COM, DTU, Denmark

- 51 A bidimensional signal processing approach to vesicle trafficking analysis in 3D+T fluorescence videomicroscopy
Ikhlef Bechar and Alain Trubuil, Unité de Mathématiques et Informatique Appliquées, INRA Jouy-en-Josas, France
- 61 Characterization of pre- and postoperative macular holes from retinal OCT images
Jakob Thomadsen et al., Netcompany IT and Business Consulting, Denmark
- 69 Texture and wavelet based lesion classification using color images
Artur Chodorowski et al., Signals and Systems, Chalmers University of Technology, Sweden
- 75 Preliminary clinical results for the *in vivo* detection of breast cancer using interstitial diffuse optical spectroscopy
Anthony Kim et al., Sunnybrook Research Institute, Dept of Medical Biophysics, Toronto, Canada
- 83 Optical coherence tomography in dermatology
Jakob Thomsen et al., OPL, Risø National Laboratory, Denmark
- 93 The intrinsic dimension of multispectral images
Cicero Mota et al., Departamento de Matematica, Universidade Federal do Amazonas, Manaus, Brazil

Hyperspectral Image Analysis: Some Applications in Biotechnology and Their Prospective Solutions

Mark Berman¹, Alope Phatak², and Pascal Vallotton¹

¹ CSIRO Mathematical and Information Sciences, Macquarie University Campus,
North Ryde NSW 2113, Australia, mark.berman@csiro.au

² CSIRO Mathematical and Information Sciences, Leeuwin Centre, 65 Brockway Rd,
Floreat WA 6014, Australia

Abstract. The automated identification and mapping of the constituent materials in a hyperspectral image is a problem of considerable interest. A significant issue is that the spectra at many pixels in such an image are actually mixtures of the spectra of the pure constituents. We review methods of “unmixing” spectra into their pure constituents, both when a “spectral library” of the pure constituents is available, and where no such library is available. Our own algorithms in both these areas will be exemplified in the presentation with biological and pharmaceutical examples.

1 Introduction

Every material has a distinctive spectrum that tells us about its chemistry. A spectrum is the mathematical and visual representation of the amount of light that the material reflects, absorbs, transmits, scatters or fluoresces at hundreds or thousands of wavelengths. Usually, a spectrum can be represented as a reasonably smooth curve. Hyperspectral images produce a spectrum at each pixel in an image. So hyperspectral images enable us to **map** variations in chemistry.

The first hyperspectral scanners, built in the 1980’s and 1990’s, were designed for airborne applications, primarily for mineral, environmental and military applications. However, in recent years, hyperspectral microscopes and cameras have been developed and are being used for **terrestrial** applications in areas such as medical diagnostics, burns analysis and skin cancer, biosecurity, pharmaceuticals, forensics and in agribusiness.

A significant issue in hyperspectral imaging is that the spectra at many pixels in an image are actually mixtures of the spectra of pure constituents. In this paper, we will review methods (proposed mainly in the remote sensing and chemometrics literatures) of “unmixing” spectra into their pure constituents, both when a “spectral library” of the pure constituents is available, and where no such library is available. Many real world applications lie between these two extremes, i.e. some, but not all, of the constituents are unknown. This review will include some of our own methods, most of which were originally developed

for mineral applications (both airborne and terrestrial), but that have in recent years been further developed in response to various applications in biotechnology.

In Section 2, we discuss the basic linear mixture models on which most unmixing algorithms are based. Biological and pharmaceutical applications of algorithms associated with some of these models will be given in the presentation. In Section 3, we propose future research directions, as well as discussing new types of biophotonic data to which these techniques (or modifications thereof) are likely to be amenable.

2 Outline of Underlying Models and Algorithms

To help motivate what follows, Fig. 1 shows 16 images (each of size 512×384 pixels) of a mouse lung with a tumor labelled with green fluorescent protein. The objective is to identify the location of the tumor. The fluorescence was excited by blue light (450-490 nm) and the images were collected at 10 nm intervals from 500 to 650 nm (i.e. in the green and red part of the visible spectrum) using an early version of CRI's MaestroTM small animal fluorescence imaging system.

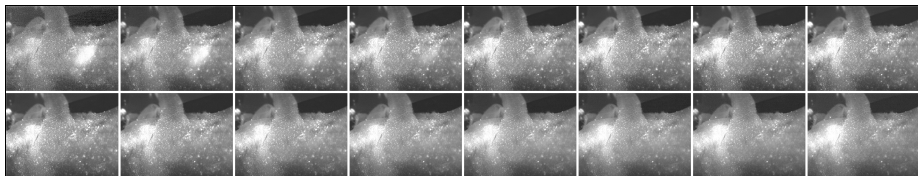


Fig. 1. 16 images (500 - 650 nm) of a mouse lung with a GFP-labelled tumor

The most common approaches to analysing hyperspectral data such as these are based on a linear mixture model. Let \mathbf{X}_i denote the spectrum of d observations at pixel i (in the example, $d = 16$). Assume that data are linear mixtures of M constituents. Then the mixture model is:

$$\mathbf{X}_i = \sum_{k=1}^M w_{ik} \mathbf{E}_k + \epsilon_i, i = 1, \dots, N, \quad (1)$$

where N is the number of pixels (in above example, $N = 512 \times 384 = 196,608$), \mathbf{E}_k is the spectrum of the k th pure constituent, ϵ_i is an error term (usually assumed to have a common within-class covariance matrix, Σ), and the w_{ik} 's are weights, usually constrained to be **non-negative**. In the mouse lung example, pure constituents might include cancerous and non-cancerous tissue, and background regions outside the body. Often it is implicitly assumed that Σ is proportional to the identity matrix. However, spectra are highly correlated locally so that this is an incorrect assumption.

2.1 Unmixing When a Spectral Library is Available

When many pure samples are available to construct a spectral library (i.e. all the \mathbf{E}_k 's are known), and both M and d are reasonably small, Σ may be estimated reliably by the average **sample** within-class covariance matrix, $\hat{\Sigma}$. Linear discriminant analysis can then be used to estimate the w_{ik} 's. This is most conveniently done in Canonical Variate space (McLachlan, 1992, Section 3.9.2), for then Σ is transformed to the identity matrix and the problem becomes a least squares problem. The least squares problem with the non-negativity constraint on the weights can be solved using **quadratic programming** techniques (Nocedal and Wright, 1999, Chapter 16).

In many practical examples, one or more of the above conditions are violated. For instance, in several examples that we shall present, $d > 100$, so that reliable estimation of Σ is problematic. In this case, $\hat{\Sigma}$ can be penalised towards an estimator that is more appropriate for smooth curves such as spectra (Hastie et al, 1995). In mineral and tablet identification, M can also be very large (> 100). However, for any individual pixel, the number of **positive** w_{ik} 's (i.e. the number of components in the mixture) will be small (usually < 5). In this case, one approach is to find the best-fitting subset of size L ($L = 1, 2, 3, 4$ say) (Miller, 1990, Chapter 2 and Section 3.6), and to use statistical tests to decide which L produces the "best" overall fit.

The example shown in Fig. 1 records spectra in the visible part of the spectrum. At higher wavelengths (i.e. above 1000 nm), the spectra of many materials have distinctive "absorption features". These are of intermediate frequency. They sit on top of a low frequency baseline, which may be variable, due to other materials in the mixture or particle scattering. Usually, the baseline is a nuisance feature which must be taken into account. A common approach is to smooth the spectra, and then to fit (1) to their second derivatives (Næs et al, 2002, Section 10.2); effectively this removes a linear trend from the spectra. A more sophisticated approach models the background as a low frequency cubic spline (Wahba, 1990). This can be represented as a linear sum of basis functions. So (1) can be extended to include these basis functions, and all the parameters of the combined linear model can be fitted simultaneously (Berman et al, 1999).

2.2 Unmixing When a Spectral Library is Not Available

In this case, neither the w_{ik} 's, nor the \mathbf{E}_k 's (the spectra of the pure constituents) are known. The model is now "underdetermined" unless additional constraints are added. For instance, it is clear from (1) that the model is scale invariant, because we can multiply the w_{ik} 's by any constant and divide the \mathbf{E}_k 's by the same constant, and the model is unchanged. There are also less obvious invariances, such as rotation invariance. In the chemometrics literature, such indeterminacies are usually dealt with by imposing constraints such as the unimodality of spectra (when appropriate), the non-negativity of spectra, or the so-called "convex geometry" constraint (Jaumot et al, 2005):

$$\sum_{k=1}^M w_{ik} = 1, w_{ik} \geq 0, k = 1, \dots, M. \quad (2)$$

These constraints mean that the w_{ik} 's can be interpreted as **proportions**. Least squares fitting of (1), subject to some or all of these constraints, is usually carried out in the original space or possibly principal component space. Note that the implicit assumption here is that Σ is proportional to the identity matrix.

If there is no error in (1), then (1) and (2) together tell us that the data lie inside a “simplex” in an $(M - 1)$ -dimensional subspace, and that the M endmembers form its vertices. We call this an M -simplex. When $M = 3$, the simplex is a triangle; when $M = 4$, it is a tetrahedron.

In the remote sensing literature, the aim is often to find (approximately) this subspace and then to fit a simplex with M vertices to the data in this subspace. The subspace usually used is the Minimum Noise Fraction (MNF) space (Green et al, 1988), also called Noise-Adjusted Principal Component space (Lee et al, 1990). The MNF transform can be thought of as a surrogate for the Canonical Variate transform. It uses spatial information to estimate Σ implicitly. Methods of estimating the simplex include those of Craig (1994), which finds the **minimum** volume M -simplex **enclosing** all the data, Winter (1999), which finds the **maximum** volume M -simplex constrained to lie **within** the data, and our own ICE algorithm (Berman et al, 2004, 2005), which usually finds a solution between these two extremes.

In the presentation, we will compare ICE with the methods of Craig, Winter and Jaumot on several data sets.

3 Future Research Directions and Possible Applications

The analyses of the example data sets that we will present highlight several areas for future research. These include: (i) the incorporation of spatial context into the unmixing procedure (whether a spectral library is available or not); this is based on the assumption that most neighbouring pixels in a scene will have a similar composition; (ii) the incorporation of a low frequency baseline to deal with particle scattering when a spectral library is absent; and (iii) the incorporation of non-negativity constraints on the spectra into ICE; this is a little delicate technically, because the constraints are in spectral space, while the optimisation is carried out in MNF space.

In terms of applications, the technology promises to dramatically increase multiplexing capabilities for biophotonics; in particular in the context of fluorescence cell imaging (Ehrhardt, 2003). Due to the spectral overlap of different fluorophores, it is rare nowadays to be able to monitor more than 4 different colours (i.e. proteins, DNA strands, viruses etc.) simultaneously. With the advent of new hyperspectral microscopes and algorithms such as our own, it should become possible to separate tens of different cell components. This will help to

provide deeper insight into infective, apoptotic, transport, homeostatic or migrative mechanisms. The benefits of hyperspectral imaging are particularly compelling for live cell microscopy; while there are currently no less than 10 different fluorescent proteins suitable for this application, only a couple can be separated using conventional fluorescence filters.

Improvements in technologies such as Raman microscopy will offer new exciting opportunities for advanced unmixing algorithms (Cheng et al, 2002). Raman signals provide label-free information about the cell chemistry. First results indicate that different organelles can be identified by their Raman signature. This capability will find applications for in situ metabolomics, cancer detection, pathogen identification and location proteomics. It is likely that algorithmic improvements, such as those that we have developed, will play a role towards fulfilling these objectives.

References

1. McLachlan, G.: *Discriminant Analysis and Statistical Pattern Recognition*. John Wiley & Sons, New York (1992)
2. Nocedal, J., Wright, S.: *Numerical Optimization*. Springer, New York (1999)
3. Hastie, T., Buja, A., Tibshirani, R.: Penalized discriminant analysis. *Annals of Statistics* **23** (1995) 73–102
4. Miller, A.: *Subset Selection in Regression*. Chapman and Hall, London (1990)
5. Næs, T., Isaksson, T., Fearn, T., Davies, T.: *A User-Friendly Guide to Multivariate Calibration and Classification*. NIR Publications, Chichester, UK (2002)
6. Wahba, G.: *Spline Models for Observational Data*. SIAM, Philadelphia (1990)
7. Berman, M., Bischof, L., Huntington, J.: Algorithms and software for the automated identification of minerals using field spectra or hyperspectral imagery. In: *Proceedings of the 13th International Conference on Applied Geologic Remote Sensing, Vancouver*. Volume 1. (1999) 222–232
8. Jaumot, J., Gargallo, R., de Juan, A., Tauler, R.: A graphical user-friendly interface for mcr-als: a new tool for multivariate curve resolution in MATLAB. *Chemometrics and Intelligent Laboratory Systems* **76** (2005) 101–110
9. Green, A., Berman, M., Switzer, P., Craig, M.: A transformation for ordering multispectral data in terms of image quality with implications for noise removal. *IEEE Transactions on Geoscience and Remote Sensing* **26** (1988) 65–74
10. Lee, J., Woodyatt, A., Berman, M.: Enhancement of high spectral resolution remote sensing data by a noise-adjusted principal components transform. *IEEE Transactions on Geoscience and Remote Sensing* **28** (1990) 295–304
11. Craig, M.: Minimum-volume transforms for remotely sensed data. *IEEE Transactions on Geoscience and Remote Sensing* **32** (1994) 542–552
12. Winter, M.: Fast autonomous spectral endmember determination in hyperspectral data. In: *Proceedings of the 13th International Conference on Applied Geologic Remote Sensing, Vancouver*. Volume 2. (1999) 337–344
13. Berman, M., Kuiveri, H., Lagerstrom, R., Ernst, A., Dunne, R., Huntington, J.: ICE: A statistical approach to identifying endmembers. *IEEE Transactions on Geoscience and Remote Sensing* **42** (2004) 2085–2095
14. Berman, M., Phatak, A., Lagerstrom, R.: ICE: A statistical approach to identifying endmembers in biomedical hyperspectral images. In: *SPIE Proceedings*. Volume 5694., San Jose, U.S.A. (2005) 62–73

15. Ehrhardt, D.: GFP technology for live cell imaging. *Current Opinion in Plant Biology* **6** (2003) 622–628
16. Cheng, J., Jia, Y.K., Zheng, G., Xie, X.: Laser-scanning coherent anti-Stokes Raman scattering microscopy and applications to cell biology. *Biophysical Journal* **83** (2002) 502–509

Quantifying composition of human tissues from multispectral images using a model of image formation

Ela Claridge, Dzena Hidovic-Rowe, Felipe Orihuella Espina, Iain Styles

School of Computer Science, The University of Birmingham, Birmingham B15 2TT, U.K.
{E.Claridge,D.HidovicF.O.Espina,I.B.Styles}@cs.bham.ac.uk

Abstract. This paper describes a novel method for quantitative interpretation of multispectral images. By constructing an optical model of a tissue and by modelling the image formation process we predict the spectral composition of light remitted from the tissue. The parameters characterising the tissue are varied to represent the entire range of tissue instances. The modelling of image formation is used in place of statistical modelling in which training is performed using measured data with known parameterisation. In this way the method overcomes a common problem in medical imaging where “ground truth” data can be impossible to obtain. The paper shows application of the method to the recovery of histological parameters characterising the skin, the eye and the colon.

1 Introduction

Colour plays an important role in the clinical diagnosis of many conditions. However, the receptors in the clinician’s eye, as well as the sensors in a standard RGB camera, provide only a limited representation of the visible spectrum. Research in medical spectroscopy has shown that spectral data can yield information beyond what is possible by observation or photography. One well known example is pulse oximetry which uses two spectral measurements to determine blood oxygenation. Although very useful, spectroscopy is inherently one-dimensional and lacks the ability to show spatial variations, which are an important diagnostic factor. Abnormalities often show themselves as unexpected patterns or distortions of regular features and colours.

Multispectral imaging can combine these two important indicators: spectral signatures and spatial variations. Suitable imaging systems exist, but interpretation of multispectral data is an open problem. One common approach is spectral classification whose objective is to distinguish between the spectra of normal and abnormal tissues. Based on the classification, false-coloured “diagnostic” images are then presented to a clinician. However, there is a well recognised lack of enthusiasm amongst the clinicians for such “black box” systems. Our earlier research has shown that images which reveal information on the basis of which diagnosis can be formed with high confidence, are much more acceptable.

Light which enters the tissue interacts with its components, and through these interactions (mainly absorption and scatter) the spectral composition of light is altered in a characteristic way. Thus remitted light bears an imprint of tissue properties. How can we derive information related to these properties from the spectra? If the parame-

ters describing composition of the imaged tissue were known a priori, the spectral information could be correlated with these known parameter values using statistical analysis (e.g. multivariate techniques). A statistical model constructed through training using this “ground truth” data could be then used to estimate the parameter values associated with the image spectra. However, most tissues are too complex and the parameters of interest, for example the level of blood supply, cannot be easily determined. Moreover, linear methods are not very appropriate in this domain because the light scatter in tissue makes the relationships between the tissue composition and its spectra highly non-linear.

In recent years we have developed a methodology which overcomes the problem caused by the lack of the “ground truth” data. Instead of training a model on known measured spectral data, we train it on the spectral data generated by a physics-based model of image formation applied to an optical model of a tissue. We construct a non-linear multi-dimensional model, parametrised by those tissue components which have been found to affect the spectral variability. Fortuitously, we have found that usually the same parameters carry diagnostically relevant information. Moreover, the analysis of spectral variability as a function of the parameter changes allows us to define a small number of spectral bands which contain the bulk of information pertaining to the parameters. Following image acquisition in these chosen bands, the parameters are recovered from the multispectral image data through the “model inversion”. The recovered parameter values are represented in the form of parametric maps, one for each parameter. The maps show both spatial variations and variations in the magnitude of the parameters, and have been found useful in diagnosis.

We have applied this method of quantitative parameter recovery to multi-spectral images of the skin [5], the eye [6] and the colon [2]. This paper draws on that earlier work, explains the general principles of our method and shows examples of the clinical applications.

2 Image formation model

Tissue model. Although in this paper we concentrate on human tissues, our methodology is applicable to any material which is composed of a number of optically homogenous layers occurring in a known and pre-determined order. The generic requirements are that each layer’s composition and the optical properties of its components must be known across a range of wavelengths, as must be the typical ranges of the layer thickness and component concentrations. Optical responses from all the layers under consideration must be detectable.

Typical tissue components of interest are pigments (e.g. haemoglobins in the blood) and structural fibres (e.g. collagen), membranes and cells. Their optical properties are specified by the wavelength dependent factors: the refractive index, the absorption coefficient, the scatter coefficient and the anisotropy factor. These properties are treated as the model “constants” and have to be specified a priori. The model variables are typically the quantities of the above components which vary from one instance of the tissue to another, for example haemoglobin concentration, thickness of

a collagenous layer or density of collagen fibrils. These variables are the parameters which we would like to recover from multispectral images of the tissue.

Light interaction model. A spectrum remitted from a tissue is the result of interaction of incident light with the tissue components. Any absorbers (pigments) will attenuate light at specific wavelengths, and the degree to which light is attenuated will depend in part on the pigment concentration. Any scatterers will selectively alter paths of the incident photons at different wavelengths and in this way change the shape of the remitted spectra. These interactions can be modelled and for a given tissue composition (as defined above) the corresponding diffuse reflectance spectrum can be computed by solving a light transport equation, normally using an approximate method (e.g. Kubelka-Munk). In this work we use Monte-Carlo method [4], a stochastic approach which simulates the interactions of a large number of photons (of the order of 10^{4-5}) with tissue. It does so by computing the probability that a photon of a specific wavelength is reflected, absorbed or scattered in a given tissue layer. A reflectance curve is generated by carrying out simulations for all the wavelengths.

Imaging system model. The final step in the model of image formation is the process of image acquisition. The tissue is illuminated using a light source with a given spectral profile ($I_0(\lambda)$). The remitted light is then separated into narrow-band spectral components, normally using filters with known transmission properties ($F_n(\lambda)$). The filtered light is recorded by a camera whose sensors (e.g. CCD) have a particular quantum efficiency characteristics ($Q(\lambda)$). The imaging model can be expressed as

$$\{ \int I_0(\lambda) F_n(\lambda) Q(\lambda) d\lambda \}_{n=1, \dots, N} \quad (1)$$

3 Tissue reflectance model: the ground truth

Given the optical model of a tissue and a method for modelling of the light interaction we can predict the spectra remitted from the real tissue. Further on, given a model of the imaging system, including spectral filter definitions, we can predict values in the multispectral image data. This *forward model of image formation* provides us with the means of relating tissue parameter magnitudes to image values. In section 4 we shall describe the methods for carrying out the inverse process, that is obtaining the parameter magnitudes from image values. In this section we shall outline the algorithm for computing the tissue reflectance model and discuss the essential details related to its implementation.

Building the model. A generic algorithm for constructing the tissue reflectance model is shown below. In the essence, for a given tissue it computes the range of all possible reflectance spectra, and then their multispectral representations. In order to implement this algorithm we have to choose which tissue components (parameters) to represent in the model; and for each parameter we have to define its range and sampling (discretisation). In the last step we have to define the filters which implement

the transition from spectra to image values through the application of the imaging system model (Eq. 1).

```

given
  incident light  $I_0$ 
  the number and the order of distinct optical layers
  the optically active components within each layer
  absorption and scatter coefficients for all the components
for all values of parameter  $p_1$ 
  for all values of parameter  $p_2$ 
  . . .
  for all values of parameter  $p_k$ 
    compute Reflectance_Spectrum  $\langle r_1, \dots, r_M \rangle =$ 
      Light_Interaction_Model( $I_0, p_1, \dots, p_k$ )
    compute multispectral image vector  $\langle Y_1, \dots, Y_N \rangle =$ 
      convolve( $\langle r_1, \dots, r_M \rangle, \textit{Imaging_System_Model}$ )

```

Tissue related parameters. Each tissue has specific and unique composition in terms of the optical layers, their arrangement and quantities. This information is normally obtained from histology textbooks. The composition of superficial tissues is limited to a relatively small number of absorbing pigments and scatter-originating connective tissues. Their optical properties can be found from research publications (e.g. see [8]).

Some quantities stay constant; some quantities vary, but have little effect on the spectra. Prior to making a commitment to a particular parameterisation it is useful to carry out preliminary modelling for *all* the known parameters in order to determine their role as a variable or as a constant: the more of the variable parameters the more complex the model and the subsequent parameter recovery. The choice of granularity for parameter discretisation is not critical as normally the spectra change smoothly as a function of the parameter changes. We have found empirically that having around 5 ± 1 discrete values within a given range gives satisfactory results.

Spectrum related parameters. By acquiring multi-spectral images we represent a continuous spectrum by a set of discrete values. As the image acquisition is implemented through bandpass filtering, it is necessary to define the number and the spectral locations of the filters, and for each filter its bandwidth and transmittance. A simple solution is to choose uniform sampling throughout the entire visible range. However, this may lead to increase in computational effort. We have implemented a method for optimal filter selection which defines a small number of filters, M (for N variable parameters $M=N$ or $M=N+1$) with the objective to minimise the error with which the parameters can be recovered from image values. The method also ensures that with the chosen filters there is a one-to-one, unique, correspondence between all the parameter vectors and all the image vectors. The details are given in [1,5].

Formalised description of the model. The tissue reflectance model is constructed for N variable parameters which have been found to affect the shape of the remitted spectra. Each specific instance of tissue can thus be defined by an N -dimensional parame-

ter vector $\mathbf{p}=\langle p_1, \dots, p_n \rangle$. The range of each parameter is discretised to k_n levels, giving in total $K=k_1 \times k_2 \times \dots \times k_n$ parameter vectors which, together, define *all the possible instances* of the given tissue (within given discretisation). Through modelling of the light interaction with tissue and of the image acquisition process we associate with each parameter a spectrum and an M-dimensional image vector $\mathbf{i}=\langle i_1, \dots, i_M \rangle$. The parameter vectors together with the image vectors form the tissue reflectance model: $\mathbf{i} = f(\mathbf{p})$. This model is used in the next step to derive parameters from multispectral images of tissue.

4 Image interpretation

The model captures the relationship between the tissue parameters and the corresponding image vectors. In this sense it is equivalent to a statistical model obtained by training using images with known ground truth. We now can proceed with the main objective of this work, which is to find the parameters given multispectral image values. We shall refer to this process of parameter recovery as the “model inversion”. In general, this is a very difficult task, especially when the model is highly non-linear. We have explored three different inversion methods, as described below.

Direct spectral matching. The simplest method of inversion is to find a model spectrum which best matches the given measured spectrum. The parameters used to generate the model spectrum are then assumed to correspond to the parameters which represent the measured spectrum. The method of finding the best match was implemented as a distance minimisation problem. In addition to the parameter values, this method can return additional useful quantities, for example the scale factor, which is a function of the distance between the camera sensor and the imaged tissue and which helps to appreciate the shape of the colon surface.

Model inversion via multidimensional interpolation. As the forward model is constructed using a numerical solution to the radiative transport equation, it is not possible on its basis to formulate an analytical inverse function which would return the parameters given the spectra. We can exploit the fact that, formally, the model is a vector-valued function on a vector domain ($\mathbf{i} = f(\mathbf{p})$, see Sec. 3). If a given measurement vector $\hat{\mathbf{i}}$ corresponds exactly to a model image vector \mathbf{i} , the parameter vector \mathbf{p} can be obtained via a simple look-up. In all other cases we need to find an approximate solution. Given that the mapping between image vectors and parameter vectors is unique, and the density of the data points is sufficiently high, we can employ the inverse function theorem and compute parameter vector $\hat{\mathbf{p}}$ for an arbitrary measurement vector $\hat{\mathbf{i}}$ using a truncated Taylor expansion.

Neural network. Using the discretised model we have trained a two-layer, radial-basis neural network. The image vectors generated by the model were used as inputs, and the corresponding model parameter vectors were provided as the target outputs

[7]. After training, the input to the network were the measurement vectors obtained from the image, and the output were the estimated parameter vectors.

5 Experimental results

The parameter recovery methods described above were applied to a range of multispectral medical images [2,5,6]. In this section we show examples of applications for three tissues: the skin, the eye and the colon.

Before showing the results we briefly outline a typical image acquisition process. Multispectral imaging is implemented using a liquid crystal tuneable filter VarSpec (C.R.I., USA) which allows the selection of narrow Gaussian shaped filters of half-width 5-7nm in the range from 400 to 700nm. The filter is mounted on front of a high sensitivity monochrome camera Retiga Exi 1394 (QImaging, Canada). The individual spectral images forming the multi-spectral data set are acquired serially. The acquisition time is chosen to ensure that the images are correctly exposed.

Prior to quantitative interpretation the acquired image data is pre-processed to remove the effects of the image acquisition system. Individual images are normalised to an exposure time of one second, a gain of one and offset of zero. Spectrum at each pixel is then deconvolved with the imaging model spectrum to give a “pure” tissue reflectance spectrum which can then be compared to the model spectrum.

Skin. The skin imaging work was carried out with the purpose of early detection of skin cancers, and in particular malignant melanoma. The skin model comprises three layers, and variable parameters include the haemoglobin concentration, melanin concentration in the epidermal and the dermal layers, and the thickness of the dermis [5,6]. Only small areas of the skin are imaged and for this reason the imaged skin area can be assumed to be flat and thus to get uniform illumination. This removes the need to carry out spatial normalisation of the illuminant, resulting in a fairly simple model where spectra are represented by four optimally selected spectral bands [5]. The four parameters are derived from the model using linear interpolation. Figure 1 shows an example of quantitative parametric maps of a skin cancer. The parameter recovery method has been used clinically for several years and it has proved to be a powerful tool for cancer diagnosis and other applications [3].

Eye. We have developed a four-layer model of the eye structure, parametrised by five parameters: the concentration of the haemoglobins and the melanins (separately) in different layers, and the concentration of the macular pigment. The back of the eye (ocular fundus) is imaged through an ophthalmic microscope (called a fundus camera). The passage of light through the eye, including the pupil, and the curvature of the fundus, make it impossible to determine the spatial distribution of the incident light. For this reason the model uses the normalised spectral representation (image quotients [5,7]). Each spectrum is represented by six narrow spectral bands, one of which acts as a normalising factor. As the eye cannot stay still during image acquisition, the images in the individual spectral bands have to be registered prior to the parameter extraction. Inconsistent illumination caused by the movement sometimes

causes problems with the parameter recovery, and is the subject of work in progress. The two parameters of clinical interest, the levels of the retinal blood and the levels of the macular pigment, are derived from the image data using neural networks. Figure 2 shows the examples of the parametric maps of retinal blood and Macular Pigment.

Colon. The colon has three optically distinct layers. The layers are parameterised by haemoglobin concentration and its saturation, and by three parameters characterising the connective tissue: the size of collagen fibres, their density and the layer thickness. As the colon surface is uneven, an additional parameter estimates the distance between the point on the surface and the CCD sensor and acts as a scaling factor on the magnitude of each spectrum. The images are obtained from ex-vivo colon samples and 33 narrow band spectra are recorded. The parameters are recovered using the direct spectral matching. Figure 3 shows the parametric maps of the colon in which clear differences between the normal and the cancerous tissue can be seen.

6 Discussion and conclusions

This paper has described a novel method of quantitative interpretation of multispectral images and showed its application to the recovery of histological parameters from images of the skin, the eye and the colon. The novelty of the method lies in the way it constructs and encodes the relationship between the parameters of interest and the image data. In traditional statistical methods such relationships are constructed experimentally. This requires the availability of the “ground truth”, which most often is a physical entity (object) for which parameter values are known. The object properties, such as for example its spectral reflectance, are measured and related to the known parameters through a statistical model. In our work, which involves imaging of living human tissues, it is virtually impossible to obtain the ground truth through measurements. In their place we have constructed a virtual experimental set-up which is based on a detailed model of image formation. The optical model of tissue provides the required ground truth for the subsequent inversion process through which the quantitative tissue parameters can be recovered.

One disadvantage of our method is that it requires a great deal of a priori information, including detailed parametrisation of tissue properties, as well as the development of high-fidelity light propagation models. However, if quantitative results are required, the effort in researching parameters and refining models is worthwhile.

As the method is based on physics, it is genuinely quantitative. The images shown in this paper provide visual representation of the recovered data, but behind the pixels there are true physical quantities for concentration, density and thickness of the tissue components. We believe that such results provide objective information about tissues, even in the presence of inevitable errors, and are more clinically valuable than, for example, classification based on spectral data.

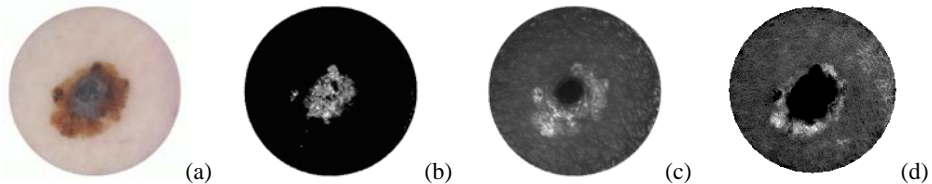


Fig. 1. (a) Colour image of a skin cancer melanoma; parametric maps showing levels of (bright=more) (b) dermal melanin, (c) collagen thickness and (d) dermal blood

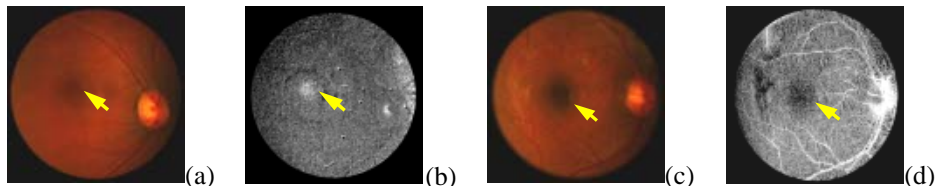


Fig. 2. (a) and (c): RGB images and their parametric maps (bright=high level) showing (b) Macular Pigment; arrow points to fovea where elevated levels of MP can be seen. (d) retinal blood; retinal vessels can be clearly seen; arrow points to fovea with decreased levels of blood

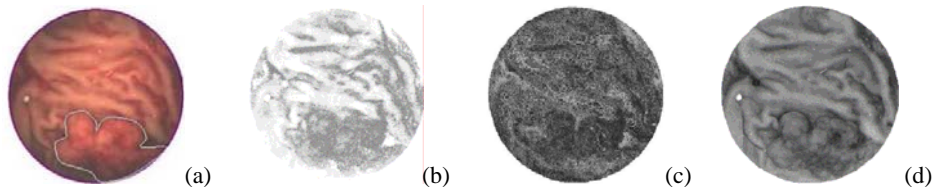


Fig. 3. (a) RGB image of the colon with cancerous area outlined; parametric maps showing levels of (dark=high level) (b) haemoglobin in mucosa, (c) thickness of mucosa and (d) the scaling factor (proportional to the elevation)

References

1. Claridge E, Preece SJ (2003) An inverse method for the recovery of tissue parameters from colour images. *Information Processing in Medical Imaging (IPMI)*, LNCS 2732, 306-317.
2. Hidovic D, Claridge E (2005) Model based recovery of histological parameters from multi-spectral images of the colon. *Medical Imaging 2005. Proc. SPIE Vol. 5745*, 127-137.
3. Moncrieff M, Cotton S, Claridge E, Hall P (2002) Spectrophotometric intracutaneous analysis - a new technique for imaging pigmented skin lesions. *BJD* 146(3), 448-457.
4. Prahl SA et al. (1989). A Monte Carlo model of light propagation in tissue. *SPIE Insitute Series IS 5*, 102-111.
5. Preece SJ, Claridge E (2004) Spectral filter optimisation for the recovery of parameters which describe human skin. *IEEE PAMI*, 26(7), 913-922.
6. Styles IB et al. (2005) Quantitative interpretation of multispectral fundus images. *Medical Imaging 2005: Proc. SPIE Vol. 5746*, 267-278.
7. Styles IB et al. (in print) Quantitative analysis of multispectral fundus images. *Medical Image Analysis*.
8. *Tissue Optics* (1994) SPIE Milestone Series Vol. MS 102, Tuchin VV (Ed.).

Multi-spectral recordings and analysis of psoriasis lesions

Line H. Clemmensen and Bjarne K. Ersbøll

Informatics and Mathematical Modelling, Technical University of Denmark, DK-2800 Lyngby, Denmark. `lhc@imm.dtu.dk` and `be@imm.dtu.dk`

Abstract. An objective method to evaluate the severeness of psoriasis lesions is proposed. In order to obtain objectivity multi-spectral imaging is used. The multi-spectral images give rise to a large p , small n problem which is solved by use of elastic net model selection. The method is promising for further studies of larger data sets including more patients than the four regarded here.

1 Introduction

Traditionally, evaluation of psoriasis lesions are performed subjectively by trained staff using the PASI (*psoriasis area and severity index*, [1]). This evaluation form is limited with regards to large-scale studies. In 2001 SAPASI (*self-administrated PASI*) was proposed where the evaluation is performed by the patients themselves [2]. This study concluded that objective methods for clinical evaluation of psoriasis is needed.

The ratings of the four patients considered here have been performed according to the severity index of the PASI. It's scale is from 0 (none) to 4 (maximum). The severity of the lesions are measured by the degree of erythema and the degree of infiltration of the lesions. Erythema is the redness of the skin caused by dilatation and congestion of the capillaries. This is often a sign of inflammation or infection. Infiltration refers to the thickness of the psoriasis lesion¹.

To obtain an objective method of evaluation multi-spectral imaging is considered. Each multi-spectral image consists of nine spectral bands. Hence, a large amount of data is present for each of the few observations. Such constitutions are referred to as large p , small n problems. To analyze the problem at hand we use *least angle regression - elastic net* which introduces a sparsity into the solution and in this way selects a subset of features [3].

2 Method

This study considers four patients each with two lesions imaged. Two to five images have been acquired of each lesion area. This amounts to a total of 26 images. The lesions have been valuated in the range from 0 to 2, i.e. the variance

¹ Psoriatic skin is thicker than healthy skin, [1].

regarding the severity index is small within the four patients. The segmentation of the ROIs (*regions of interest*) of the inflammations and the scales of the lesions is illustrated in Figure 1.

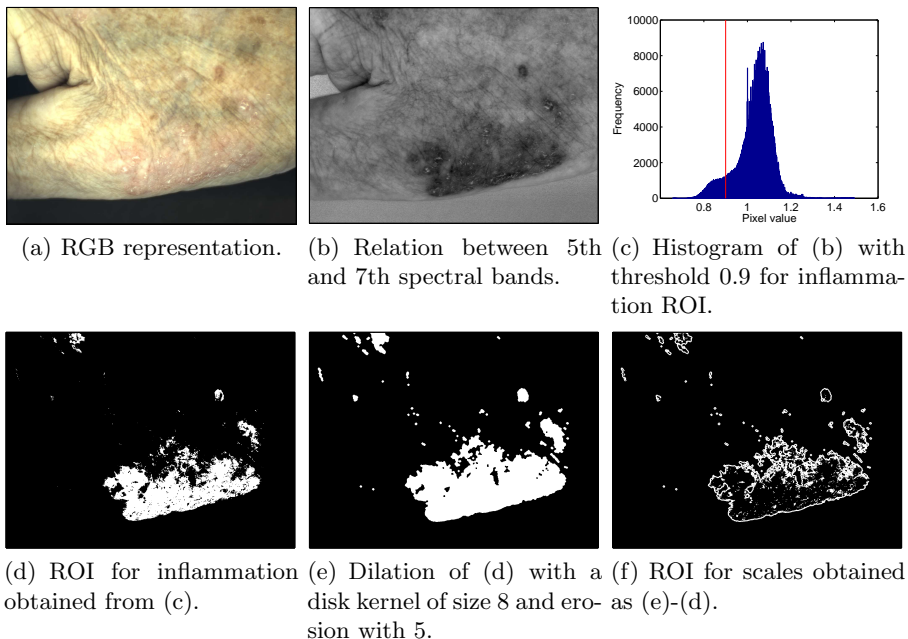


Fig. 1. Illustration of the segmentation of the ROIs in the images. The pairwise relation between the 5th (amber) and 7th (red) spectral bands, (b) is used since this emphasizes the red inflammations. Two ROIs are segmented: One containing the inflammation (d) and another containing the scales (f).

From the original spectral bands and from the pairwise ratios between the spectral bands the following features are extracted from both the inflammation ROI and the scale ROI: The 1st, 5th, 30th, 50th, 70th, 90th, 95th, and 99th percentiles. This amounts to 1458 features.

LARS-EN (*least angle regression - elastic net*) model selection, proposed in [3], combines Ridge regression [4] and Lasso model selection [5,6] and hereby obtains sparse solutions with the computational effort of a single ordinary least squares fit. This method is used to analyze the large p , small n problem at hand.

3 Results and discussion

Patient number three is not included in the analysis since both the RGB image and the further analysis imply that this is an outlier. The analysis is performed

using LARS-EN with leave-one-out cross-validation [7]. Only two features are needed to describe the degree of erythema and of infiltration, respectively. The results are illustrated in Figure 2. The variables give a good ordering of the evaluations. Furthermore, the standard deviations for the training and the test are: 0.4/0.5 and 0.5/0.6 for erythema/infiltration.

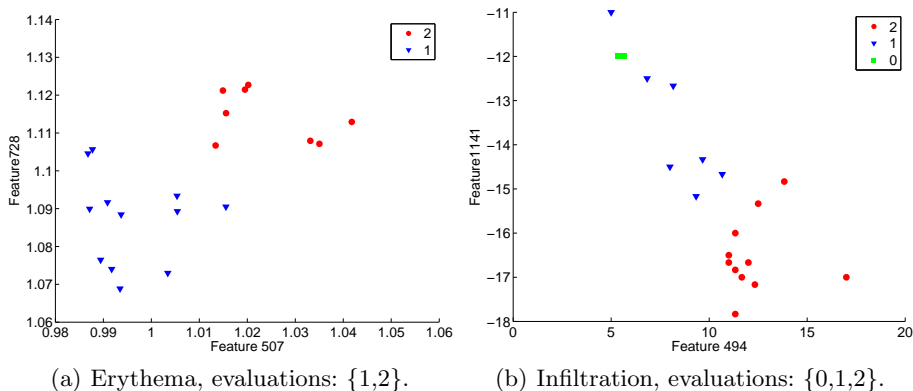


Fig. 2. Scatter plots of the two most frequently selected variables with leave-one-out cross-validation for erythema and infiltration, respectively.

Summing up, the results are promising as variables are selected which give a good ordering of the patients according to the severity index ratings. Furthermore, the standard deviations of the leave-one-out cross-validation are relatively small for only two variables. The next step will be to evaluate the method on larger data sets.

4 Acknowledgements

The authors would like to thank dermatologist Dr. Lone Skov at Gentofte Hospital, Denmark for her cooperation and for performing the severity index evaluations of the four patients.

References

1. Fredriksson, T., Petersson, U.: Severe psoriasis - oral therapy with a new retinoid. *Dermatologica* **157** (1978) 283–41
2. Szepietowski, J.C., Sikora, M., Pacholek, T., Dmochowska, A.: Clinical evaluation of the self-administered psoriasis area and severity index (sapasi). *dermatovenerologica - alpina, pannonica et adriatica* **10**(3) (2001) 1–7
3. Zou, H., Hastie, T.: Regularization and variable selection via the elastic net. *J. R. Statist. Soc. B* **67**(Part 2) (2005) 301–320

4. Hoerl, A.E., Kennard, R.W.: Ridge regression: Biased estimation for nonorthogonal problems. *Technometrics* **12** (1970) 55–67
5. Tibshirani, R.: Regression shrinkage and selection via the lasso. *J. R. Statist. Soc. B* **58**(No. 1) (1996) 267–288
6. Efron, B., Hastie, T., Johnstone, I., Tibshirani, R.: Least angle regression. Technical report, Statistics Department, Stanford University (2003)
7. Hastie, T., Tibshirani, R., Friedman, J.: *The Elements of Statistical Learning*. Springer (2001)

Creating surface chemistry maps using multispectral vision technology

Jens Michael Carstensen, Michael Edberg Hansen
Informatics and Mathematical Modelling
Technical University of Denmark, building 321
DK-2800 Kgs. Lyngby, Denmark
{jmc, meh}@imm.dtu.dk
<http://www.imm.dtu.dk>

Jens Michael Carstensen, Niels Chr. Krieger Lassen, Per W. Hansen
Videometer A/S
Lyngsø Allé 3
DK-2970 Hørsholm, Denmark
{jmc,nckl}@videometer.com
<http://www.videometer.com>

Abstract

An imaging concept for acquiring high quality multispectral images is presented. Information in the multispectral images is focused on properties originating in the surface chemistry through an integrating sphere illumination. This enables the creation of very detailed surface chemistry maps with a good combination of spectral and spatial resolution. A few illustrative examples are presented.

1. Introduction

Imaging and machine vision have now for several decades been an obvious choice for the characterization of non-homogeneous materials. Geometric measurements like counting and assessment of size and size distribution is now implemented as inexpensive off-the-shelf systems. The same goes for detection of highly standardized patterns like machine printed characters, bar codes and datamatrix codes. Many systems can also do shape measurement and - to some degree - color measurements. However, doing proper radiometric measurements – including color measurements – with vision systems requires effective handling of a number of critical issues that arises from the inherent properties of such systems

- The pixel values is typically a composite of many different optical effects, like diffuse reflectance, specular reflectance, topography, fluorescence, illumination geometry, spectral sensitivity etc. The precise composite will typically depend on pixel position.

- The systems have to deal with heterogenous materials which disables making useful assumptions – like smoothness - about the above effects.
- The combination of geometry and radiometry in every measurement adds a great deal of complexity, but also offers a huge measurement potential.

An effective way of dealing with these issues is a twofold strategy

- Carefully design the vision system with respect to the task at hand. Optimize illumination geometry. Focus on reproducibility and traceability of the measurements.
- Provide the necessary redundancy in the imaging system to enable meaningful statistical analysis of the image data.

There are two powerful means of obtaining an effective redundancy: using multiple wavelengths or spectral sensitivity curves, and using multiple multiple illumination geometries. In the first situation we talk about *multispectral vision* and in the second situation we talk about *multiray vision*. While multispectral techniques mainly focus on surface chemistry and color in a general sense, multiray techniques are more oriented towards physical surface properties like shape, topography, and gloss. A wellknown technique for estimation shape from shading, *photometric stereo*, is a special case of multiray vision. Multispectral vision and mulriray vision can obviously be combined to further enhance redundancy.

Multispectral vision technology is the topic of this paper.

2. Multispectral imaging

Figure 1 shows an illumination principle that is highly suitable for reflectance measurements. The camera is looking through an integrating sphere and the sample or object is placed in an opening on the opposite side of the sphere. The object then receives a very uniform and diffuse light. Shading effects, shadows, and gloss-related effects are minimized. Further the geometry of the illumination system is relatively simple to apply in an optical model. This means that the errors that are inherent in the system can be estimated and corrected for. One of the important error sources is the systematic error of self-illumination. The sample will contribute to its own illumination since light is reflected back into the sphere from the sample. A red object will thus receive more red light and a blue object will receive more blue light. This effect can at first sight be surprisingly large, due to the properties of the integrating cavity. However, modeling and correction for such effects is possible and highly enhanced the applicability of the system. The system has to be geometrically and spectrally calibrated as well. The implementations of this patented technology has shown that it is possible to make highly accurate and reproducible multispectral vision measurements with relatively inexpensive systems.

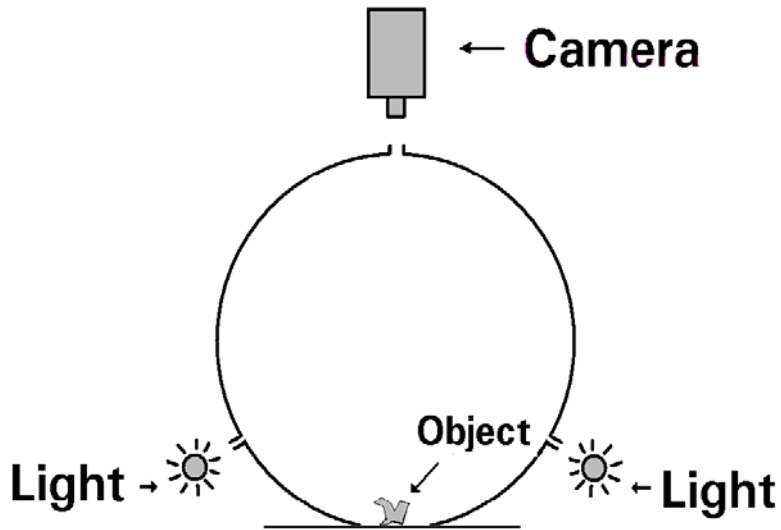


Figure 1: Principle of imaging with integrating (Ulbricht) sphere illumination. The illumination of the object will come from reflections from the white coating on the inner surface of the sphere. This illumination will be very uniform and diffuse if the size of the lower opening is not too large compared to the diameter of the sphere.



Figure 2: VideometerLab is one of the implementations of the multispectral vision technology. The right image shows the positioning of the different diodes.

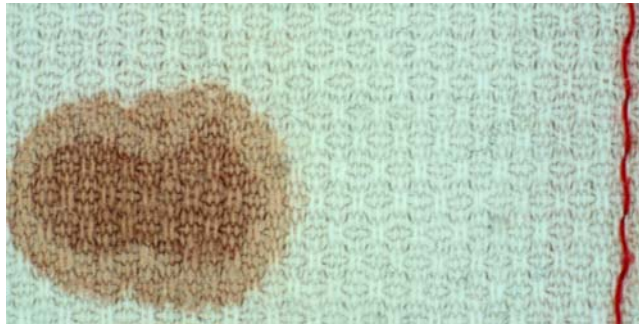
The multispectral measurements are easily obtained by strobing light emitting diodes (LED) with different spectral characteristics. Figure 2 shows the illumination system of a laboratory system for multispectral vision measurements. With standard off-the-shelf inexpensive systems measurements in the range 380-1000 nm can be done with high resolution. UV systems and NIR/IR systems above 1000 nm are also available basically at the extra cost of the sensor and optics.

3. Examples

For many applications measuring 10 or 20 different bands including NIR will provide a much more specific information about the sample than a trichromatic (e.g. RGB) image. The relative presence of some wavelengths and relative absence of others is a very specific characteristic of many material properties, and this can be applied to many different kinds of problems e.g.

- to characterize materials
- to characterize components of composite materials
- to remove irrelevant material from the analysis
- to find defects and foreign matter

In Figure 3 we see how the use of a NIR band can make it easy to isolate a coffee spot and a textile fabric. The enables precise characterization of the spot or the textile or a combination of the two.



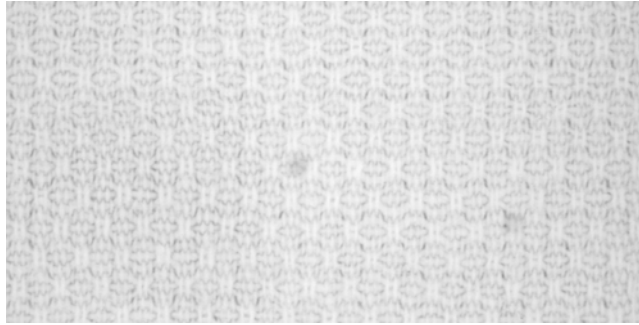


Figure 3: Textile fabric with coffee spot. Above: traditional color image. Below: same image region taken at 875 nm, where only the textile structure is visible. Multispectral images are highly suitable for separating different kinds of surface chemistry in a heterogeneous material.

In Figure 4 we see how NIR bands can be used to separate skin from hair. This could be applied in dermatological applications.

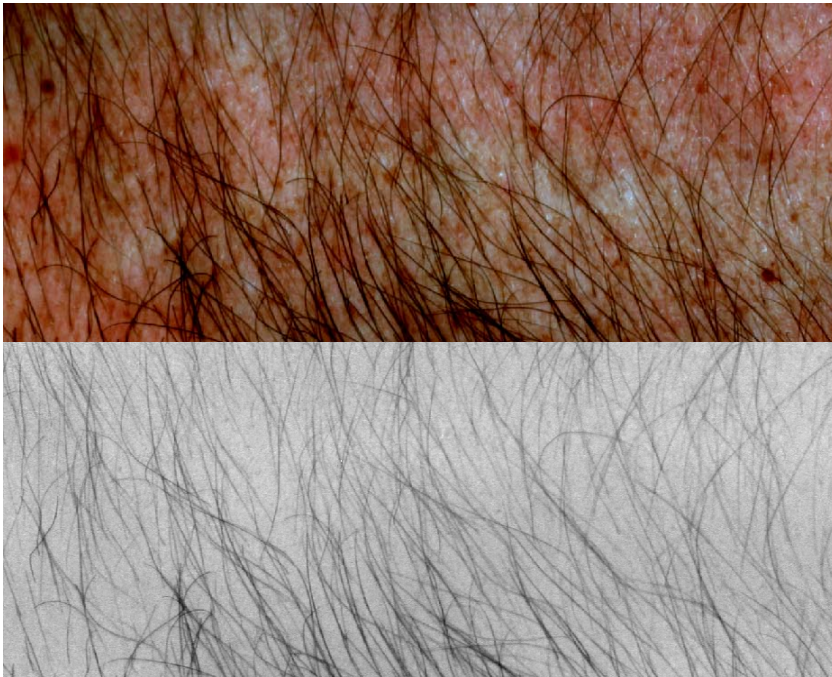


Figure 4: Skin image. Spectral analysis using NIR bands is very powerful in separating the skin from the hair thus enabling a characterization of skin pigmentation without a need to shave the skin.

In Figure 5 with see a bread image. Figure 6 and Figure 7 shows how the crust and the crumb structure can be separated spectrally.

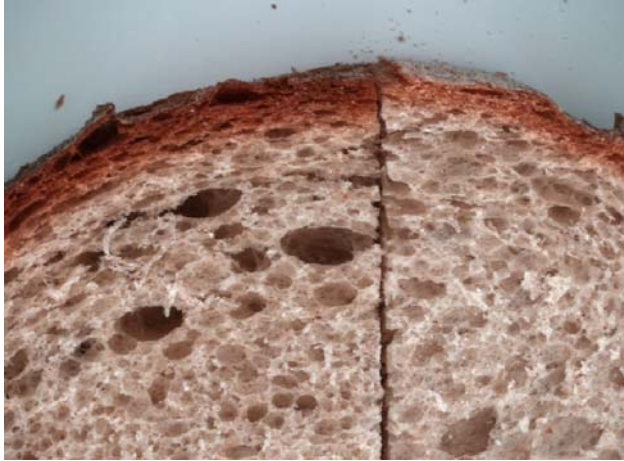


Figure 5: Traditional color image of bread.

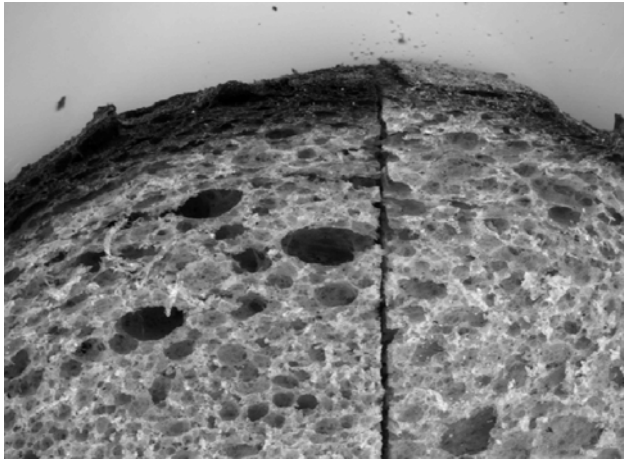


Figure 6: 472 nm (blue) band showing the crust.

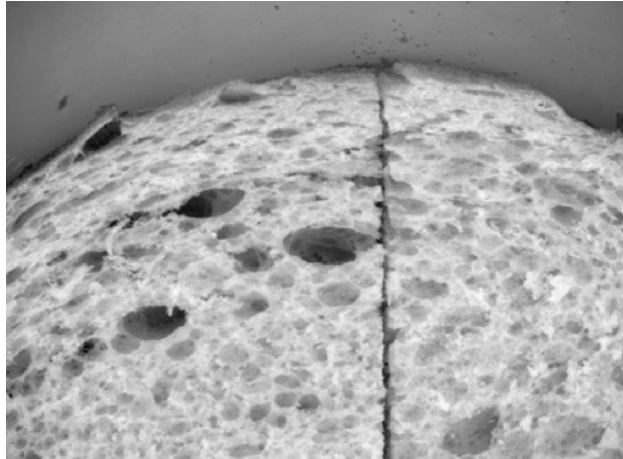


Figure 7: 940 nm (NIR) showing the crumb structure.

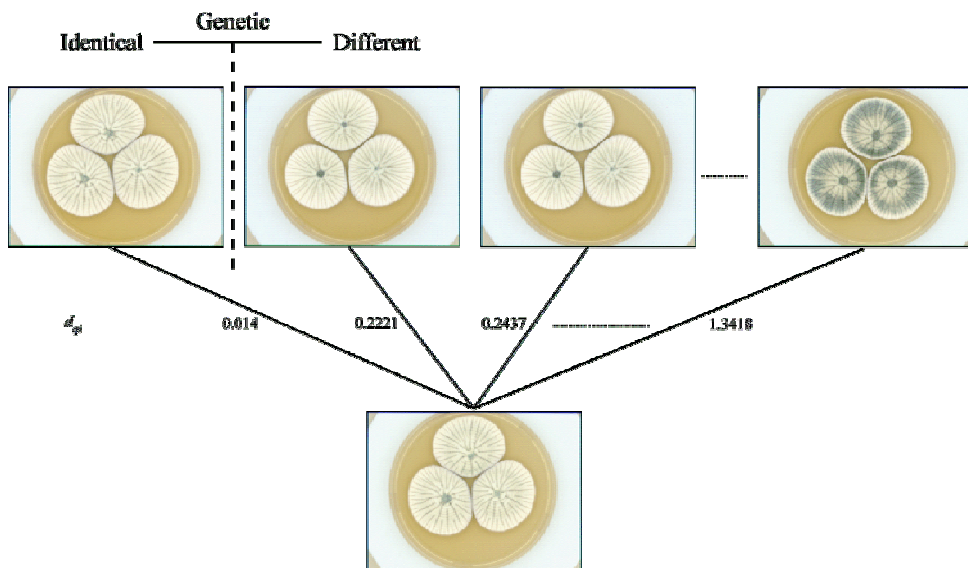


Figure 8: Example of using multispectral imaging to identify fungal species and even isolates within species. From [1].

Figure 8 shows results of a classification system for fungal species and for isolates within species. The results of this system are also very convincing.

Other applications are measurements on e.g. fur, seeds, fruit, meat, grain, paper, metal, and printed matter.

4. Conclusions

Multispectral vision will be a key technology in future measurements of non-homogeneous samples. High-performing and relatively non-expensive systems are already available providing both accurate results in a broad range of applications and the reproducibility that enables useful database generation and data mining.

References

- [1] M. E. Hansen and Jens Michael Carstensen, Density-based retrieval from high-similarity image databases, *Pattern Recognition*, 37, 2004, pp. 2155-2164.

Optical imaging of the embryonic heart for a better understanding of congenital heart defects

Talât Mesud Yelbuz

Dept. of Pediatric Cardiology and Intensive Care Medicine,
Hannover Medical School, Hannover, Germany

Cardiovascular physiology changes during embryonic development in a highly complex and carefully orchestrated manner. The developing heart undergoes simultaneous structural and functional maturation as it transforms in a dynamic process from a straight tube to a four-chambered heart (Fig. 1). Even minor negative factors or triggers could disrupt critical processes of heart development resulting in many forms of heart defects (1). In the past various imaging techniques have been employed by us and others to visualize the intricate processes of cardiovascular development in 2 or 3 dimensions in order to achieve a better understanding of the underlying mechanisms for the genesis of congenital heart defects during embryonic development (2, 3). In the first part of the talk a short overview will be given on some new imaging modalities, including a newly constructed environmental chamber with an integrated high-speed video microscope system, to image embryonic chick hearts.

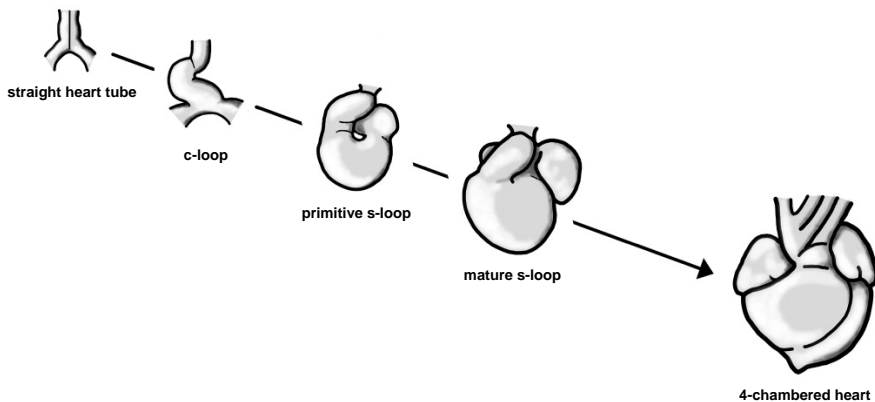


Fig. 1: Schematic drawing illustrating cardiac development in the chick embryo from the stage of the straight heart tube (Hamburger-Hamilton (HH)-stages 9+/10- (day 1 ½) up to the stage of the four-chambered heart (HH-stage 35/36(day 9)). Adapted from Männer (4).

In the second part of my talk, I'll focus on our collaborative research work with colleagues from Risø National Laboratory (Optics and Plasma

Research Dept.), Denmark, on imaging the developing heart in chick embryos by using High-Resolution Optical Coherence Tomography (OCT). OCT is an emerging non-invasive real-time 3D imaging modality to serve best for visualization of semi-transparent and highly lightscattering structures in biological materials at micron-scale level (5). We have conducted studies to visualize the embryonic chick development in 3D in very early stages by following the same embryo over time (4D). Most recently we have completed another study on *in vivo* visualization of coronary artery development by using a new mobile OCT system, developed by our colleagues from Risø National Laboratory.

Coronary artery (CA) development is one of the most critical but poorly understood processes during cardiovascular development. It is currently impossible to visualize this complex dynamic process on living human embryos. Not only that, but also in living animal embryos this intriguing process could not be unveiled yet due to methodological limitations. We have only recently acquired to the best of our knowledge the very first *in vivo* images of developing CAs in chick hearts from embryos grown in shell-less cultures at three critical stages during development (day 8 through 10; Fig. 2 and Fig. 3). We have been also able to generate *in vivo* OCT recordings by use of the functional extension of our system for Color Doppler imaging to demonstrate blood flow in CAs and vitelline vessels of the chick embryo.

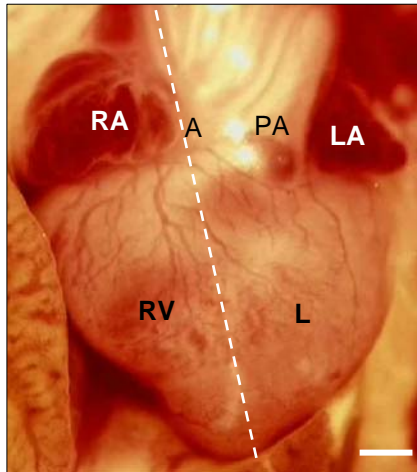


Fig. 2: Ventral view of a day 9 chick heart in original size and with higher magnification on the right. Dashed line indicates sagittal section plane for OCT scanning. Bar = 0,5 mm. Ao indicates Aorta; LA, left atrium; LV, left ventricle; PA, pulmonary artery; RA, right atrium; RV, right ventricle.

The real-time OCT system we used for the above mentioned studies is a mobile fiber-based time-domain real-time OCT system operating with a center wavelength of 1330 nm, and a typical frame rate of 8 frames/s. The axial resolution is 17 μm (in tissue), and the lateral resolution is 30 μm . The OCT system is optimized for *in vivo* chick heart visualization and enables OCT movie recording with 8 frames/s, full automatic 3D OCT scanning, and blood flow visualization, i.e., Doppler OCT imaging.

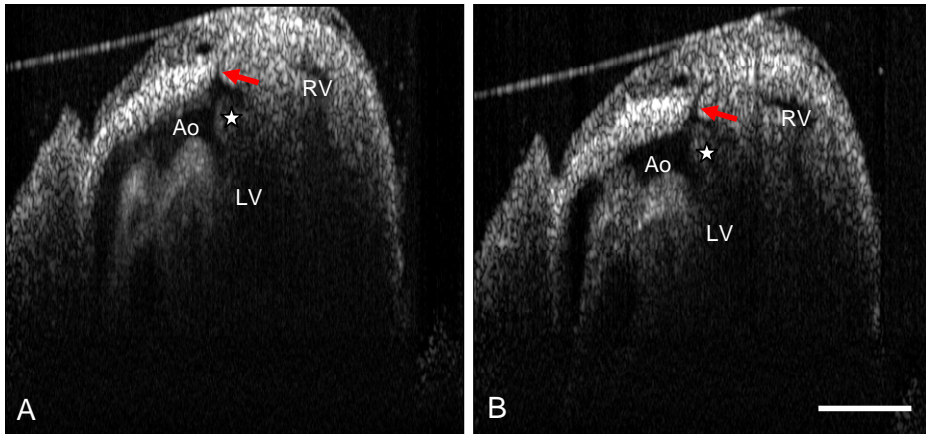


Fig. 3: Images from an *in vivo* recording of a OCT scan demonstrating the clearly established blood flow in right coronary artery (RCA) arising from the ascending aorta in a day 9 chick heart in systole (A) and diastole (B) in the sagittal plane as depicted in Figure 2 with the dashed line. Note the filling of RCA during diastole in B when the vessel becomes fully visible. Bar = 0,6 mm. Ao indicates Aorta; LV, left ventricle; RV, right ventricle; star, aortic valve cusp; arrow in red, course of RCA.

References:

- 1) Phoon CK (2001) *Curr Opin Pediatr.* 13:456-64
- 2) Yelbuz TM et al. (2002) *Circulation.* 106:e44-5
- 3) Yelbuz TM et al. (2002) *Circulation.* 108:e154-5
- 4) Männer J (2004) *Anat Rec A Discov Mol Cell Evol Biol.* 278:481-92
- 5) Yelbuz TM et al. (2002) *Circulation.* 106:2771–2774

Stereo Reconstruction of the Epicardium for Optical Fluorescence Imaging

Desmond Chung¹, Mihaela Pop¹, Maxime Sermesant², Graham A. Wright¹

¹ Department of Medical Biophysics, University of Toronto,
Sunnybrook Health Sciences Centre, Toronto, Canada

² INRIA Sophia Antipolis, France and King's College, London, UK

Email: dchung@swri.ca

Abstract Optical imaging using voltage-sensitive fluorescence dye can record cardiac electrical activity with sub-millimeter resolution that is unattainable with conventional electrode systems. The interpretations of activation recordings are often limited by the two-dimensionality of the maps obtained from the 2D optical images, and little has been done to overcome this limitation. We present a novel method to simultaneously estimate the activation patterns derived from fluorescence images and the 3D geometry of the heart by using a stereo camera configuration. Our results suggest that the stereo reconstruction is feasible in large hearts and may enable a more realistic visualization of propagation of cardiac electrical waves.

1 Introduction

Optical imaging using voltage-sensitive fluorescence dye has become a powerful research tool in studying cardiac arrhythmias [1]; however, the reconstructed maps of the action potential (AP) propagation on the epicardium are often limited to 2D projections. Moreover, the speed of propagation depends on the curvature polarization front, which cannot be correctly estimated from a 2D projection. Recently, this limitation was overcome by using 2 CCD cameras: one mapping the changes in AP and the other capturing the 3D geometry of the heart [2,3]. Simultaneously recovering the 3D epicardial geometry with the AP propagation patterns allows this information to be mapped onto theoretical 3D models of cardiac electrical activity. We present a novel method to simultaneously estimate the activation patterns derived from fluorescence images and 3D geometry of the heart by using a stereo camera configuration. The realistic 3D reconstruction could potentially allow for the validation of 3D theoretical predictions of AP propagation in a point-by-point comparison of simulation results against experimental measurements.

2 Method

We begin by describing the methodology used to record the optical fluorescence images, and then detail the steps used to reconstruct the epicardium in 3D from the stereo optical image pairs.

2.1 Optical Imaging

Optical fluorescence images of the AP propagation were obtained in swine hearts (approximately 8cm long), using a Langendorff ex-vivo perfusion preparation at 37°C. A schematic of the experimental set-up is shown in Figure 1. The hearts were paced at 60 beats per minute via a bipolar electrode placed inside the ventricle, at the apex. The fluorescence dye (0.2ml sol. di-4-ANEPPS, Biotium Inc.) was dissolved in 20ml of perfusate, and injected continuously over 10 minutes into the coronary system. The dye was excited at $531\text{nm} \pm 20\text{nm}$ through a green filter (FF01-531/40-25, Semrock Inc., Rochester, NY, USA) with two 150W halogen lamps (MHF G150LR, Moritek Corp., Japan). The lamps were controlled by shutters (labeled 'S' in the schematic below) to avoid dye photo-bleaching. The emitted signal was passed through a $>610\text{nm}$ high-pass filter and recorded with 2 high-speed CCDs (MiCAM02, BrainVison Inc., Japan).

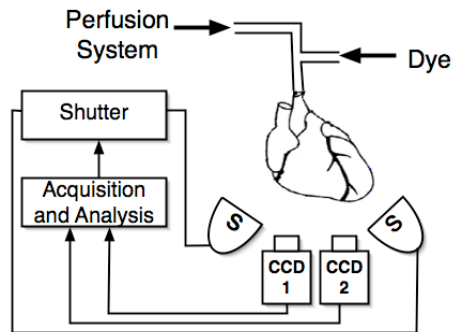


Figure 1. The experimental set-up used for stereo optical fluorescence imaging, with the halogen light sources labeled 'S'.

Fluorescence images of the epicardial surface were captured at 270 frames per second over 192×128 pixels, yielding a spatial resolution of less than 0.7mm, and a temporal resolution of 3.7ms. The action potential is given by the inverse of the relative change in fluorescence.

2.2 Stereo reconstruction

The stereo reconstruction process requires that both cameras capture overlapping areas of the epicardium, hence their parallel alignment, shown in the schematic in

Figure 1. The stereo camera pair was jointly calibrated using images of a planar calibration checkerboard in a large variety of positions [6], of which samples are shown in Figure 2. We first resolve the intrinsic and extrinsic parameters of each camera, and then for the rotation and translation between the pair [5].

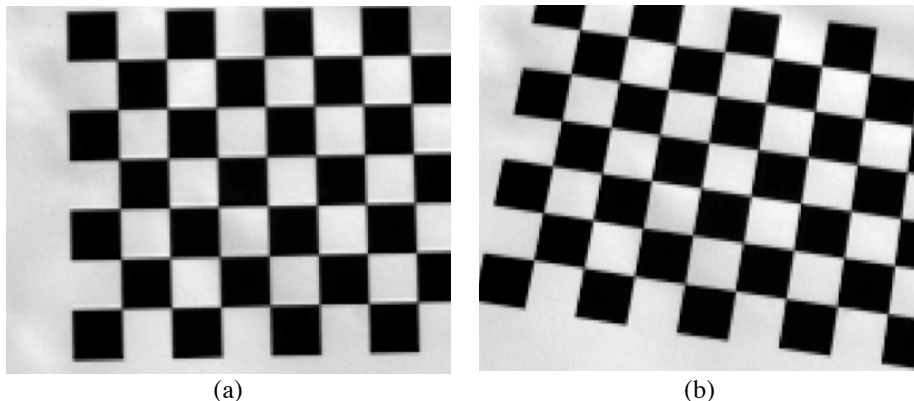


Figure 2. Sample images of the calibration grid in approximately (a) fronto-parallel and (b) tilted and rotated views.

The camera calibration parameters were used to rectify all the stereo image pairs collected during fluorescence and normal imaging, so that point correspondences from matching image pairs could be found by searching along horizontal scan lines [4]. Normalized cross-correlation was used to compare the 11 x 11 patch centered at each pixel in the left rectified image, to candidate patches in the right rectified image, centered on the same horizontal scan line. For a pixel coordinate (x,y) in the left image, and stereo disparity estimate, d , the normalized correlation, ψ , can be calculated as:

$$\psi(x,y,d) = \frac{\sum_{i=-5}^5 \sum_{j=-5}^5 (I_{left}(x+i,y+j) \cdot I_{right}(x+i+d,y+j))}{\sqrt{\left(\sum_{i=-5}^5 \sum_{j=-5}^5 I_{left}(x+i,y+j)\right) \cdot \left(\sum_{i=-5}^5 \sum_{j=-5}^5 I_{right}(x+i+d,y+j)\right)}} \quad (1)$$

The validity of disparity estimates was then verified through the use of left-right consistency checking [8]. This process compares the disparities estimated when using the left image as the reference image during the correspondence search, against the corresponding disparities estimated when using the right image as the reference image. Under ideal circumstances, the estimated disparity values should vary by a sign change. However, half-occluded points that appear in one image of the stereo pair but not the other result in different disparity estimates depending on the reference image used. We identify image points as potentially half-occluded if the left-right consistency check produces disparity estimates for corresponding pixels that fall outside a tolerance of 2 to 3 pixels.

3 Results and Discussion

The optical imaging results shown below are taken from a single camera, although the corresponding results are available from the other camera in the stereo pair. We then present the results of the stereo reconstruction, and finally combine pseudo-colored fluorescence images with the 3D epicardium surface by texture mapping.

3.1 Optical Imaging

Illustrated in Figure 3 are AP waveforms for a 4s acquisition, shown after denoising with a soft-cubic filter (BV Analyzer, BrainVision Inc., Japan), beside a 2D projection of the activation pattern at one instance in time. The average duration of the action potential measured at 90% repolarization (APD90) is approximately 350ms, a reasonable value for healthy ventricular tissue paced at 1Hz. The depolarization front (in red) propagates from the bottom left of the heart toward the upper right side. The activation times can be represented by isochrones, lines connecting pixels of equal activation time. Figure 4 shows maps of pixel activation time from two different heart specimens paced with the stimulating electrode positioned inside the heart at the apex of the right ventricle.

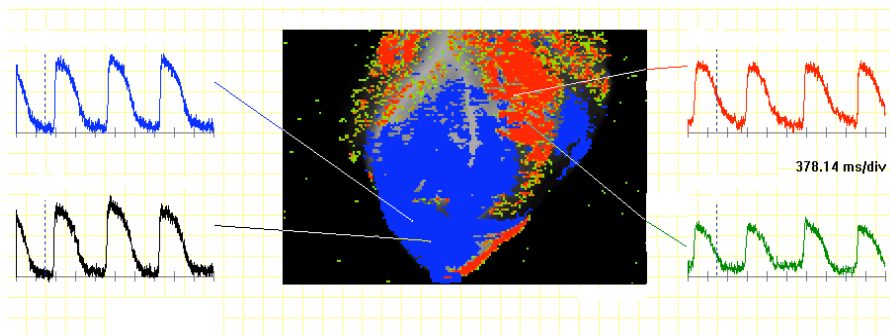


Figure 3. Action potential waveforms for four sample pixel locations of the epicardium. The red color overlay corresponds to the depolarized phase of the action potential, while the blue color corresponds to the repolarized phase.

3.2 Stereo Reconstruction

A stereo image pair under normal lighting conditions is shown in Figure 5(a) and (b). The target distances from the camera to the tissue fell in the range between 35 and 45cm, restricting the range of the disparity search to approximately 20 pixels. The disparity value that yielded the highest correlation value (which has a maximum of 1) in that range was chosen as the best disparity estimate. Disparity was used in turn to triangulate the 3D positions of each image point.

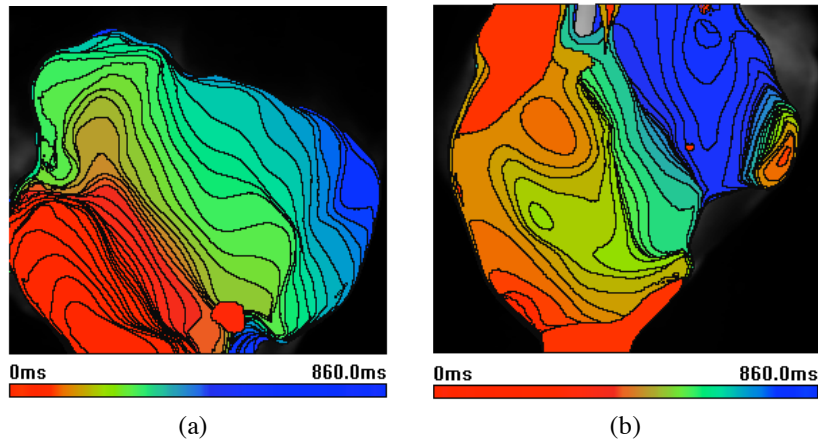


Figure 4. Activation maps from two different hearts, isochrones 20ms apart.

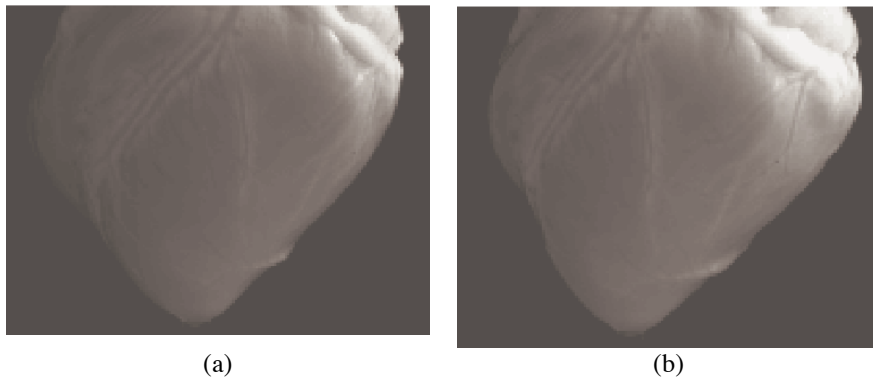


Figure 5. Examples of the (a) left and (b) right stereo image pairs taken under normal lighting.

In order to verify the validity of point correspondence estimates, a grid pattern was projected onto the heart, as shown in Figure 6, producing a set of identifiable landmarks in the left and right images of the stereo pair. The pixels on the top left and bottom right points of each grid intersection point were marked for a set of 40 intersections in the left and right images of the gridded stereo pair. The manually selected disparity estimates were then compared against those of the fully automatic cross correlation-based technique applied to the non-gridded stereo pair shown in Figure 5. The resulting comparison yielded a mean difference of 1.62 pixels over the 40 test points, with a maximum difference of 3.48 pixels.

The range of camera to target distances used in our experiments lay between 38cm and 44cm, a single pixel of disparity produced differences in depth estimates between 1.62mm and 2.11mm, with decreasing accuracy as the distance from the camera increases. Manual correspondence marking in test images of the calibration grid was

also used to measure the accuracy of 3D distance measurement between points. Measurements of lengths along the planar grid's squares of up to 44mm near the center of the field of view in a roughly fronto-parallel orientation, were all within 0.5mm of the known grid dimensions.

The final disparity map obtained from the stereo pair of ungridded images under normal lighting conditions is shown in Figure 7(a). It is important to note that disparity values cannot be accurately estimated in non-overlapping image regions, such as those areas at the left and right borders of the heart. Furthermore, it is impossible to obtain valid disparity estimates in uniform image areas, such as the black background.

Areas of possible half-occlusion are detected by the left-right consistency check, and marked regions are overlaid upon the normally lit image in Figure 7(b). Notwithstanding the tendency of left-right consistency checking to produce a significant proportion of false-positives in natural images with primarily low-frequency characteristics [8], the left-right consistency check confirms the stereo system's limited accuracy in half-occluded areas that arise due to the curvature of the heart.

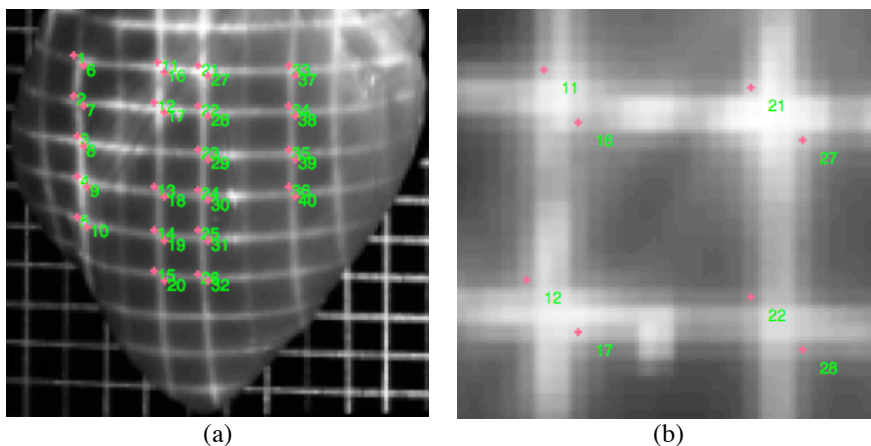


Figure 6. (a) Full scale and (b) zoomed images of the heart with a grid projected onto it. Overlaid annotations illustrate the 40 manually marked image points used to assess the validity of the cross-correlation automatic point correspondence search.

Stereo reconstruction of the 3D surface using that image pair is shown in Figure 8(a) and (b), with plain shading to illustrate the surface shape, and texture mapped to show the surface under normal lighting conditions. Figure 8(c) and (d) show the reconstructed surface texture mapped with pseudo-colored activation maps. These activation maps shows how the activation spreads diagonally when paced from the apex of the RV, from lower left part of the hearts to the upper right section.

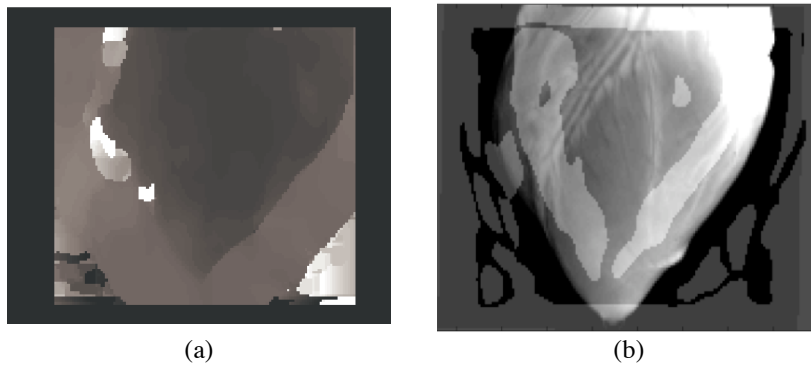


Figure 7. (a) The disparity between corresponding points in the left and right images detected by the correspondence search is inversely proportional to the depth of each image point. (b) The left to right consistency check indicates which image regions provide accurate disparity estimates (shown at normal intensity) and which regions may not (shown at higher intensity), indicating that regions of high curvature may be poorly reconstructed.

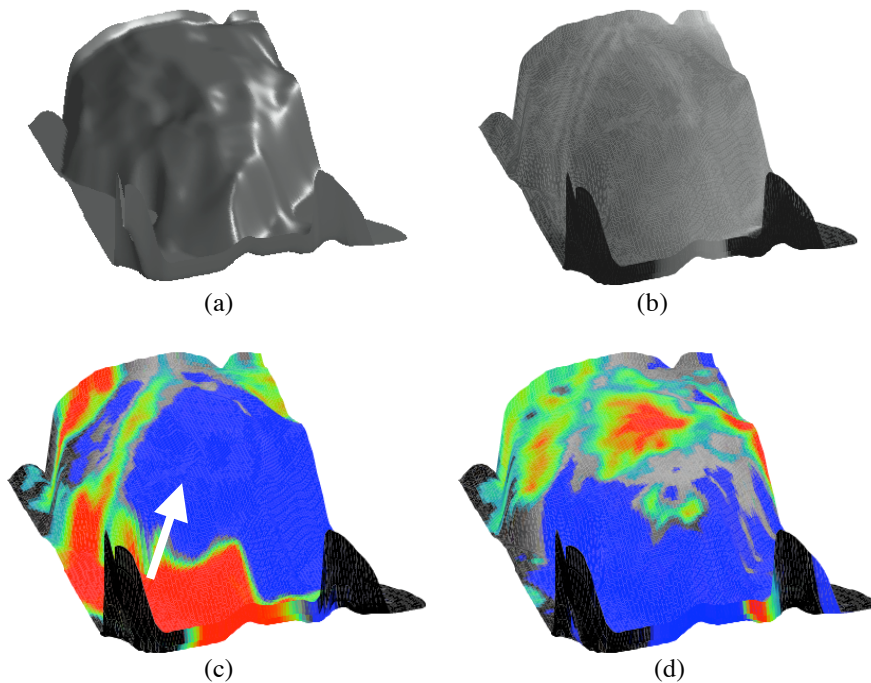


Figure 8. Renderings of the reconstructed 3D surface of the epicardium shown in Figure 5. In (a), the solid surface indicates the epicardial shape, while in (b) the surface is texture mapped with the intensities of a normally lit image. In (c) and (d) the propagation of AP is texture mapped onto the 3D surface for two instances in time. The white arrow in (c) indicates the direction of propagation.

4 Conclusion

In this work, we propose a stereo optical imaging configuration method to simultaneously recover the 3D epicardial geometry and estimate the electrical activation patterns derived from fluorescence images. Our results suggest that stereo reconstruction of the 3D epicardial surface is feasible for large hearts, comparable in size to human hearts, while avoiding the complex camera configuration required by existing work [3] for shape recovery. The technique enables the visualization and measurement of the AP propagation across the 3D geometry of the heart, providing a powerful tool for computer-aided diagnosis and for validating 3D simulations of cardiac electrical activity. Furthermore, this approach may provide more accurate measurements of electrophysiological parameters such as conduction velocity.

Future work will extend the optical imaging procedures to capture the entire epicardium by periodically rotating the heart by a small angle, then repeating reconstruction and fluorescence imaging. The stereo imaging procedure could be immediately improved by optimizing the distance between the stereo camera pair to reduce the area of half-occlusion, and by manufacturing the calibration grid with higher precision.

Acknowledgements

The authors would like to thank Dr. John Graham (Sunnybrook Health Sciences Centre, Toronto, Canada) for surgical preparation of the ex-vivo hearts, and Professor Jack Rogers (University of Alabama, Birmingham, USA) for valuable discussion regarding the optical imaging technique. This study was supported by funding from the Ontario Research and Development Challenge Fund, the Canadian Foundation for Innovation, and the Ontario Innovation Trust. Ms. Mihaela Pop is supported by a scholarship from the Heart and Stroke Foundation of Canada.

References

1. Efimov, I.R., Nikolski, V.P., Salama, G.: Optical imaging of the heart. *Circulation Research* 95(1) (2004).
2. Sung, D., Omens, J.H., McCulloch, A.D.: Model-based analysis of optically mapped epicardial activation patterns and conduction velocity. *Annals of Biomedical Engineering* 28(9) (2000).
3. Kay, M.W., Amison, P.M., Rogers, J.M.: Three-dimensional surface reconstruction and panoramic optical mapping of large hearts. *IEEE Transactions on Biomedical Engineering* 51(7) (2004).
4. Trucco, E., Verri, A.: *Introductory Techniques for 3-D Computer Vision*. Prentice-Hall (1998).
5. Bouget, J.Y.: Camera calibration toolbox for Matlab. http://www.vision.caltech.edu/bougetj/calib_doc/index.html (2005).
6. Zhang, Z., A flexible new technique for camera calibration. *IEEE Transactions on Pattern Analysis and Machine Intelligence* 22(11) (2000).
7. Heikkila, J., Silven, O.: A four-step camera calibration procedure with implicit image correction. *IEEE Conference on Computer Vision and Pattern Recognition* (1997).
8. Egnal, G., Wildes, R.P.: Detecting binocular half-occlusions: Empirical comparisons of five approaches. *IEEE Transactions on Pattern Analysis and Machine Intelligence* 24(8) (2002).

Biomedical Applications of Terahertz Technology

Vincent Wallace
TeraView Ltd
Cambridge

The terahertz portion of the electromagnetic spectrum lies between the infrared and microwave regions and until the invention of the photoconductive switch^{1,2} had been relatively unexplored. Improvements over the last two decades in the generation and detection of terahertz radiation have led to the introduction of terahertz pulsed spectroscopy (TPS)^{3,4,5} and terahertz pulsed imaging (TPI)^{6,7} with applications in pharmaceutical science^{8,9} homeland security¹⁰ and medicine^{11,12}.

We have developed a portable TPI system for use in a clinical environment. The system uses photoconduction to generate and detect terahertz radiation with frequency content from 0.1 – 4 THz. Here, we report on a study using TPI for imaging breast tumours *ex vivo*. Several breast samples were imaged and parameters from the time domain impulse functions were used to provide contrast. The size and shape of tumour regions in the terahertz images were compared with the corresponding histology section. Good correlation was found for area and shape of tumour in the THz images compared to that of histology.¹³ In addition, we have also performed spectroscopy study comparing the terahertz properties (absorption coefficient and refractive index) of excised normal breast skin and breast tumor. Both the absorption coefficient and refractive index were higher for tissue containing tumor compared to normal. These changes are consistent with higher water content and structural changes, like increased cell and protein density.¹⁴ This study demonstrates the potential of TPI to image both invasive breast carcinomas and ductal carcinoma *in situ* using THz and encourages further studies.

References

1. D.H. Auston et al. Generation and detection of millimeter waves by picosecond photoconductivity. *Appl. Phys. Lett.* 43, 631 (1983)
2. D.H. Auston, et al. Picosecond photoconducting Hertzian dipoles *App Phys Lett*; 45, 3, 211 (1984)
3. D.H. Auston and K.P. Cheung. Coherent time-domain far-infrared spectroscopy. *JOSA B.* 2, 4, 606 (1985)
4. D. Grischkowsky et al. Far-infrared time-domain spectroscopy with Terahertz beams of dielectrics and semiconductors. *JOSA B* 7, 10, 2006 (1990)
5. J.T. Kindt et al. Far-infrared dielectric properties of polar liquids probed by femtosecond terahertz pulse spectroscopy. *J. Phys. Chem*; 100, 24, 10373 (1996)
6. B.B. Hu et al. Imaging with terahertz waves. *Optics Letters*, 20, 16, 1716 (1995)
7. D.M. Mittleman et al. T-ray imaging. *IEEE J. Selected Topics Quantum Electronics* 2, 3, 679 (1996)
8. C.J. Strachan et al. Using Terahertz Pulsed Spectroscopy to Quantify Pharmaceutical Polymorphism and Crystallinity. *J Pharm Sci* 94, 4, 837 (2005)
9. A.J. Fitzgerald et al. Non-destructive Analysis of Tablet Coating Thicknesses Using Terahertz Pulsed Imaging. *J Pharm Sci*; 94, 1, 177 (2005)
10. C. Baker et al. Developments in people-screening using terahertz technology, *Proc. SPIE* 5616, 61 (2004)
11. A.J. Fitzgerald et al. An introduction to medical imaging with coherent terahertz frequency radiation. *Phys Med Bio* 47, R67 (2002)
12. V.P. Wallace et al. Terahertz pulsed imaging and spectroscopy for biomedical and pharmaceutical applications. *Faraday Discussions: Applications of Spectroscopy to Biomedical Problems* 126, 255 (2004).
13. A.J. Fitzgerald et al. TPI of human breast tumors. *Radiology* 239, 533 (2006)
14. V. P. Wallace *et al*, "Terahertz pulsed spectroscopy of human basal cell carcinoma" *Applied Spectroscopy* (in press) 2006.

The physical principles of chemical recognition in terahertz spectral imaging

Peter Uhd Jepsen¹ and Stewart J. Clark²

¹ Department of Communications, Optics & Materials, Technical University of Denmark, DK-2800 Kongens Lyngby, Denmark

jepsen@com.dtu.dk

² Department of Physics, University of Durham, Durham, United Kingdom

Abstract. Imaging in the terahertz frequency range is a promising technology for localization and identification of hidden objects as well as for applications in the medical sector. Functional terahertz imaging with the capability of detecting specific chemicals such as explosives, drugs of abuse, pharmaceutical compounds, relies on recognition of spectral features recorded at individual pixels of an image. We discuss recent progress in the understanding and the calculation of the lowest vibrational modes in hydrogen-bonded crystalline compounds. With the newest computational methods it is now for the first time possible to predict and explain the terahertz vibrational spectrum of hydrogen-bonded molecular crystals.

1 Introduction

In the recent years there has been an increased interest in the exploitation of the far-infrared, or terahertz (THz) spectral region for applications based on chemical recognition. The fact that on the one hand many packaging materials are transparent for THz radiation and on the other hand the THz spectra of many pharmaceuticals, drugs of abuse, and explosives show highly specific fingerprints show that THz spectroscopy, combined with imaging technology, hold a strong potential for identification of concealed substances by comparing the spectral signatures with entries in a database.

Yet, in part due to the lack of appropriate instrumentation the far-infrared region has for a long time remained relatively unexplored, except for a few specialized research groups working with bulky and fragile laboratory spectroscopic equipment. Therefore only few studies of the far-infrared spectra and the character of the vibrational modes that give rise to the characteristic spectral signatures in this region have been reported in the past.

Recent technological developments, most notably the invention of ultrashort-pulse lasers, have changed this situation. At present, equipment for recordings of THz spectra in the field has become commercially available. Therefore the understanding of the background of the wide range of suggested THz imaging applications becomes more and more important. There is now a tremendous activity in the field of basic and applied THz frequency research, and a sizable

fraction of this effort has been focused on the exploitation of the rich and distinct dielectric spectrum displayed by most organic molecules in the solid state in the 0.3–5 THz range. It has turned out that the vibrational modes found in this particular region of the electromagnetic spectrum are highly characteristic not only for the molecule, but also for its environment. The space group symmetry of the unit cell as well as the content of co-crystallized solvent molecules (e.g. water) has been shown to be the main factors forming the THz vibrational spectrum of the material.

The richly structured dielectric spectra often observed in poly- and single-crystal materials, including powders, are due to combinations of phonon- and intramolecular modes of the crystallites or single-crystals. On the other hand, in amorphous condensed-phase systems the existence of spectrally localized features is rare because of the strong coupling between the random environment and intramolecular modes [1]. That study showed that the long-range order of the environment of the molecules is one of the dominating factors in the shaping of the dielectric spectrum of the molecules.

In this work we present a generally applicable *ab-initio* simulation method that is capable of predicting the position and intensity, as well as identifying the normal modes of vibrational spectra in the THz region. The applicability of the method is demonstrated with results of the simulation of vibrational modes of the hydrogen-bonded molecular crystal sucrose. The experimentally determined absorption spectrum of polycrystalline sucrose has been reported earlier by Walther *et al.* [1].

2 THz time-domain spectroscopy

Standard transmission THz time-domain spectroscopy has been used for the experimental determination of the dielectric function of the crystalline systems studied here, and in a slightly modified version for simple THz imaging experiments. The technique is described for instance in [2, 1, 3].

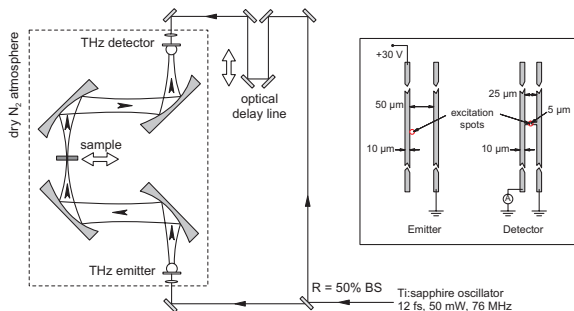


Fig. 1. Experimental setup for THz time-domain spectroscopy

This method uses femtosecond excitation- and gate pulses in two synchronized pulse trains from the same femtosecond oscillator to generate and to detect ultrashort bursts of far-infrared radiation (the THz pulses). The experimental setup is illustrated schematically in Fig. (1). Each of the excitation pulses drives an ultrafast current in a photoconductive switch. The rapid acceleration dynamics of the photogenerated charges leads to emission of a short pulse of electromagnetic radiation. This pulse is transmitted through the sample, and detected in another photoconductive switch which is gated by a second replica of the femtosecond pulse. By gradually changing the arrival time of the gate pulse with respect to the THz pulse while recording the induced photocurrent in the detector we can measure the temporal profile of the THz pulse with subpicosecond time resolution.

In the transmission experiments used for the recording of crystalline spectra in Sec. (3) the sample is placed in a closed-cycle helium cryostat equipped with 6 mm thick polymer windows, transparent to THz radiation. The spectra presented here are recorded at 10 K which make a good comparison to the zero temperature *ab initio* results.

3 Modeling of THz spectra

The reliable prediction of the precise position and strength of the peaks in the THz-frequency spectrum of crystalline compounds, as well as the assignment of these modes to specific molecular motion, has remained an unmet challenge until now for all but the simplest systems. Exceptions are systems of high symmetry and with a small number of atoms in the unit cell of the crystal. The phonon spectra of many inorganic semiconductors are well understood, silicon, germanium and gallium arsenide being well known examples. Similarly, the phonon spectra of dielectrics with simple crystal structures can be calculated, with polyethylene and diamond as classic examples.

When the number of atoms in the unit cell increases and the interaction between the atoms in the crystal becomes weaker than in covalent or ionic bonded crystals the prediction of the phonon spectrum becomes an extreme theoretical challenge. This is due to the long-range, weak interactions and the large number of ions involved in the description.

The description of solid-state, crystalline compounds must take the periodic arrangement of atoms in the crystal into account [4–6]. For a few, particularly simple crystalline systems, the periodic crystal structure can be approximated by linear strings of the molecules, and density-functional theory (DFT) applied to isolated clusters of molecules can under special circumstances successfully simulate the general appearance of THz absorption spectra [3]. However, in the general case the full crystal structure must be taken into account in order to obtain a realistic description of the lowest vibrational modes in a molecular crystal. This is the fundamental reason why calculations on isolated molecules or small units of molecules are quite successful in reproducing the mid-infrared vibrational spectra of molecules even in the condensed phase, but fail to predict

the position and intensity of low-frequency modes, typically below 5-10 THz [7, 8]. Therefore calculations on isolated molecules should be interpreted with extraordinary care when discussing vibrational modes in solid-state materials in the THz region.

Recently, Korter *et al.* performed solid-state simulations, using the software packages DMol, CHARMM, and CPMD, predicting the THz-frequency vibrational spectra of the high explosive HMX [9] and the amino acids serine and cysteine [10], taking the periodic boundary conditions of the crystal structure into account. This approach has led to reasonable overall agreement between experimental absorption spectra and simulated ones.

Our calculations are based on the plane-wave density functional method within the generalised gradient approximation as implemented in the Castep code [11, 12]. Norm-conserving pseudopotentials in the Kleinman-Bylander [13] form are used to describe the electron-ion interactions. The valence electron wavefunctions are expanded in a plane wave basis set to a kinetic energy cutoff of 1200 eV which converges total energies to better than 0.1 meV/atom. Brillouin zone integrations are performed using a k-point set that converges the energies to an equivalent accuracy. Electronic minimisations are performed using a preconditioned conjugate gradient scheme [14] and are converged to machine accuracy (approximately 10^{-13} eV/atom). Geometry optimisations are also performed using a conjugate gradients scheme; accurate geometries were found to be essential in order to obtain reliable values for the low frequencies of the molecular crystals.

It is important to note that obtaining frequencies in the THz region is a very demanding task from a computational point of view. In molecular crystals there is a wide range of bonding strengths and therefore to obtain the low frequency modes accurately, all the self-consistent and the perturbative calculations along with the geometries of the system considered must be converged to much tighter tolerances than is usual in standard plane-wave pseudopotential calculations. In general we have found that the total energy of the system (in terms of k-point sampling, total energy convergence, etc) must be converged to almost machine precision to finally obtain accurate low frequency modes.

Once accurate geometric and electronic structures are obtained, we perform density functional perturbation calculations based on the formalism of Gonze, *et al.* [4, 5] using the Castep code [11, 12, 6]. The zone centre phonon modes are calculated and also the materials' dielectric properties, bulk polarisability and Born effective charges. From this we are able to compute the spectroscopic intensities of the modes and compare directly with experiment.

We now present the results of the THz experimental frequencies and intensities and compare to the theoretical values. The experimentally recorded absorption spectrum of sucrose is shown as the full line in Fig. (2), scaled with the molar concentrations of the sample. The frequencies and intensities of the corresponding calculated modes are shown as vertical bars in the same graph. The overall intensities have been scaled by the same factor to fit within this representation, but the relative line strengths have not been adjusted.

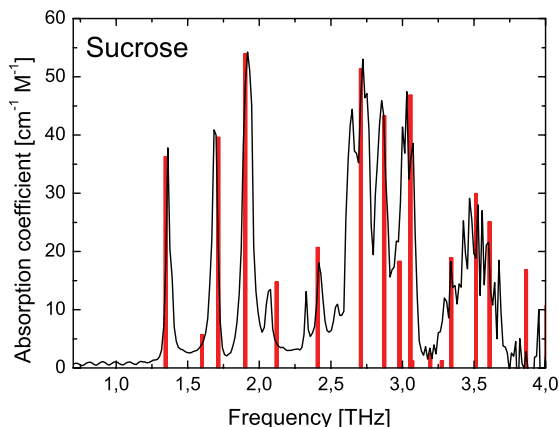


Fig. 2. Experimental (solid line) and calculated (vertical bars) vibrational spectrum of sucrose

The intensities of the measured absorption lines are reliable since it was ensured that the spectrometer was operated below its saturation [15]. Hence not only the position but also the relative strengths of the absorption lines can be compared with the simulated values. This allows a very stringent test of the simulation results.

We find a very good agreement between theory and experiment. Basically the position as well as the intensity of each observed absorption band in the frequency region below 4 THz is reproduced by the DFPT simulation. The simulation predicts only position and intensity of the normal modes of the crystal. Hence the observed line widths cannot be compared with simulations. The simulation results indicate, however, that for instance the broad absorption band between 3.2 and 3.8 THz is probably composed of several vibrational modes. There are a few modes in the experimentally determined spectrum that is not reproduced by the simulation - specifically the weak features at 2.3, 2.55, and 2.6 THz. This may indicate that these observed modes are associated with combination bands which are not accounted for in the simulation.

The close agreement between experiment and theory allows us, for the first time, to assign specific normal modes to the observed vibrational frequencies. As an example of such an assignment, Fig. (3) shows a graphical rendering of the normal mode at 1.9 THz. The direction and relative amplitude of the motion of each atom is indicated with arrows.

The dimensions of the optimized unit cell is indicated by the yellow scaffold structure, and the optimized atom placement within the unit cell is shown. To indicate the intermolecular network we show the molecules in the neighboring unit cells, indicated by transparent colors. Carbon, oxygen, and hydrogen atoms are colored green, red, and gray, respectively. The intermolecular hydrogen bonds are illustrated with blue connections, and the intramolecular covalent bonds

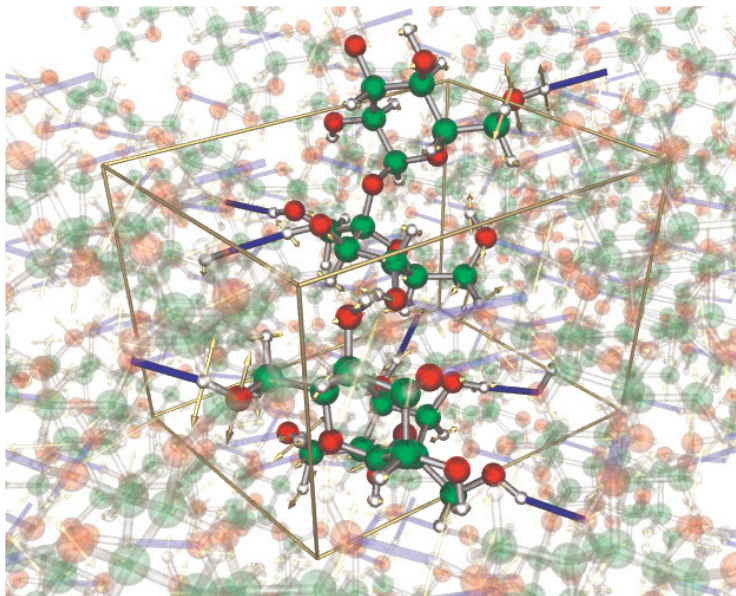


Fig. 3. Motion of the atoms in the sucrose crystal associated with the vibrational frequency of 1.9 THz. The surrounding unit cells of the crystal are indicated in half-transparent colors. Hydrogen bonds are shown in blue color while the intramolecular covalent bonds are shown in gray color.

are shown as gray connections. The figure clearly confirms that sucrose is held together by very a strong intermolecular network of hydrogen bonds.

The normal-mode motion indicated in the figure allows us to draw an important and, in our opinion, quite general conclusion about the nature of the low-frequency modes of molecular crystals. A pure intermolecular mode would lead to motion of the atoms of each molecule to have the same amplitude and identical or at least highly aligned direction. However, inspection of Fig. (3) shows that this is not the case. Both direction and amplitude of the motion of each atom in the molecules is only lightly correlated to that of the other atoms. Hence the predicted normal mode motion is neither a pure intermolecular, phonon-like motion nor a pure intramolecular vibrational mode. In contrast there is a strong and complicated coupling between the intra- and intermolecular motion, involving both hydrogen bonds and covalent bonds. This illustrates very clearly that a sharp distinction between inter- and intramolecular modes in the THz range is not possible in this case. Inspection of the other low-frequency modes of the sucrose crystal as well as simulation results on other molecular crystals indicates clearly that such a distinction is not possible in molecular crystals, even for the lowest-frequency modes.

4 Conclusions

We have demonstrated that the plane-wave DFPT method taking periodic boundary conditions into account is capable of simulating the THz vibrational spectra of different hydrogen-bonded crystals with convincing accuracy.

The detailed information available with the simulation method presented here about the solid-state THz vibrational modes of molecules will enable researchers to obtain new and important insight into the weak, delocalized forces that hold hydrogen-bonded crystals together. The interplay between weak and strong intermolecular forces can lead to unexpected behavior of vibrational modes. An example of this is the unusual blue-shift with increasing temperature of the frequency of the lowest vibrational modes in sucrose [1]. With the identification of the specific vibrational modes responsible for the blue-shifting absorption line, it should be possible in the future to perform molecular dynamics simulations taking the temperature of the crystal into account, and investigate the temperature-dependent interplay between weak and strong intermolecular forces. Similar studies could also further aid the understanding of THz anharmonicity in biologically relevant molecules, such as biotin [16].

We acknowledge partial financial support from the EU project TeraNova and from the Danish Research Agency.

References

1. Walther, M., Fischer, B. M., and Jepsen, P. Uhd: Noncovalent intermolecular forces in polycrystalline and amorphous saccharides in the far infrared. *Chem. Phys.* **288** (2003) 261-268
2. Walther, M., Plochocka, P., Fischer, B., Helm, H., and Jepsen, P. Uhd: Collective vibrational modes in biological molecules investigated by terahertz time-domain spectroscopy. *Biopolymers (Biospectroscopy)* **67** (2002) 310-313
3. Fischer, B., Hoffmann, M., Helm, H., Modjesch, G., and Jepsen, P. Uhd: Chemical Recognition in terahertz time-domain spectroscopy and imaging. *Semicond. Sci. Technol.* **20** (2005) S246-S253
4. Gonze, X.: First-principles responses of solids to atomic displacements and homogeneous electric fields: Implementation of a conjugate-gradient algorithm. *Phys. Rev. B* **55** (1996) 10337-10354
5. Gonze, X., and Lee, C.: Dynamical matrices, Born effective charges, dielectric permittivity tensors, and interatomic force constants from density-functional perturbation theory. *Phys. Rev. B* **55** (1996) 10355-10368
6. Refson, K., Tulip, P. R. and Clark, S. J.: Variational density-functional perturbation theory for dielectrics and lattice dynamics. *Phys. Rev. B* **73** (2006) 155114
7. Takahashi, M., Ishikawa, Y., Nishizawa, J., and Ito, H.: Low-frequency vibrational modes of riboflavin and related compounds. *Chem. Phys. Lett.* **401** (2004) 475-482
8. Chen, Y., Liu, H., Deng, Y., Schauki, D., Fitch, M. J., Oslander, R., Dodson, C., Spicer, J. B., Shur, M., and Zhang, X.-C.: THz spectroscopic investigation of 2,4-dinitrotoluene. *Chem. Phys. Lett.* **400** (2004) 357-361
9. Allis, D. G., Prokhorova, D. A., and Korter, T. M.: Solid-state modeling of the terahertz spectrum of the high explosive HMX. *J. Phys. Chem. A* **110** (2006) 1951-1959

10. Korter, T. M., Balu, R., Campbell, M. B., Beard, M. C., Gregurick, S. K., and Heilweil, E. J.: Terahertz spectroscopy of solid serine and cysteine. *Chem. Phys. Lett.* **418** (2006) 65-70
11. Segall, M. D., Lindan, P. J. D., Probert, M. J., Pickard, C. J., Hasnip, P. J., Clark, S. J., and Payne, M. C.: First-principles simulation: ideas, illustrations and the CASTEP code. *J. Phys.: Condens. Matt.* **14** (2002) 2717-2744
12. Clark, S. J., Segall, M. D., Pickard, C. J., Hasnip, P. J., Probert, M. J., Refson K., and Payne, M. C.: First principles methods using CASTEP. *Zeitschrift Für Kristallographie* **220** (2005) 567-570
13. Kleinman, L. and Bylander D. M.: Efficacious Form for Model Pseudopotentials. *Phys. Rev. Lett.* **48** (1982) 1425-1428
14. Payne, M. C., Teter, M. P., Allan, D. C., Arias, T. A. and Joannopoulos, J. D.: Iterative minimization techniques for ab initio total-energy calculations: molecular dynamics and conjugate gradients. *Rev. Mod. Phys.* **64** (1992) 1045-1097
15. Fischer, B. M. and Jepsen, P. Uhd: Dynamic range in terahertz time-domain transmission and reflection spectroscopy. *Opt. Lett.* **30** (2005) 29-31
16. Korter, T. M. and Plusquellic, D. F.: Continuous-wave terahertz spectroscopy of biotin: vibrational anharmonicity in the far-infrared. *Chem. Phys. Lett.* **385** (2004) 45-51

A bidimensional signal processing approach to vesicle trafficking analysis in 3D+T fluorescence videomicroscopy.

Ikhlef Bechar^{1,2} and Alain Trubuil¹

¹ Unité de Mathématiques et Informatique Appliquées (MIA), INRA Jouy-en-Josas, France, ikhlef.bechar@jouy.inra.fr

² Laboratoire de Mathématiques Appliquées de Paris 5 (MAP5), Université René Descartes, Paris, France. *

Abstract. We describe a novel automatic approach for vesicle trafficking analysis in 3D+T videomicroscopy. The method exploits spatio-temporal coherence of object's fluorescence to make robust detections of moving objects in the spatio-temporal domain. Indeed, the method first proceeds by identifying trafficking zones in the 3D volume and next analyzing at them the vesicle trafficking. The latter is viewed as significant change in the fluorescence of a site in the image. The problem is embedded in a model selection framework and is solved using dynamic programming. We applied the proposed approach to analyze the vesicle dynamics related to the trafficking of the RAB6A protein between the Golgi apparatus and ER cell compartments.

1 Introduction

With the advent of new live-cell imaging modalities (wide-field videomicroscopy, confocal videomicroscopy, FRAP, FLIM, etc. . .) made possible by the development in marker technology (GFP) and fluorescence microscopes, it has become possible to collect *in vivo* vast amounts of spatio-temporal data. Hence, there is an increasing need for providing automatic tools for the analysis of such data. So far, many techniques inspired from classical video processing have been applied more or less successfully to videomicroscopic data processing: optical flow (Miura *et al.*, 2005), individual tracking of vesicles (Danuser *et al.* 2005, 2006); kymograms (Sibarita *et al.* , 2006); IMM filter tracking (Olivo Marin *et al.*, 2004)) (see [8][9] for more details). However, due to the low SNR of videomicroscopic data (Kervrann *et al.*, 2005), the density of objects in the scene, the complexity of their dynamics (collapses, deforming shapes, appearance, disappearance), the dynamic nature of the background (Kervrann *et al.*, 2006), etc. . . , other techniques taking into account all these aspects are expected. In this paper, we present a new approach that is capable of making spatio-temporal detection of

* This work was supported by the French Ministry of Research - Project IMBIO-MODYNCELL5D.<http://www.irisa.fr/vista//ftp/ckervran/ACI-IMPBIO/MODYNCELL5D.html>

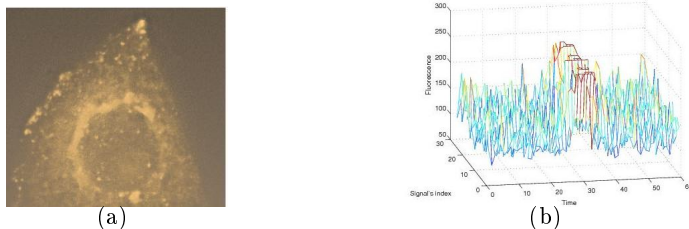


Fig. 1. (a) A volume rendering of a 3D videomicroscopic image ; (b) A packet of neighbouring signals. The figure shows a significant simultaneous change in the fluorescence of some of the 27 voxels between instants 30 and 40 due to object passage (Colour is used for visualization only).

moving objects in 3D+T videomicroscopy. These spatio-temporal detections can then be used to make certain estimations of the objects dynamics in the scene such as the number, the volume, the average fluorescence of moving objects, their movement speed and passage frequency with respect to different image regions. Our approach proceeds by first detecting activity regions of the sequence. Next, we use an original bidimensional signal processing technique to analyze the fluorescence of the voxels of each detected activity region. Finally, trafficking is detected as significant simultaneous change in the fluorescence of some or whole voxels of a given activity region. We used the developed approach to summarize and analyze the vesicle dynamics related to the trafficking of the RAB6A protein between the Golgi apparatus and ER cell compartments.

2 Method description

2.1 The basic idea of the method

The basic idea of our approach to make trafficking analysis in 3D+T videomicroscopic sequences is that a highly contrasted object, when crossing a given voxel of the 3D image, makes its fluorescence intensity passing from a low to a higher value (*cf.* Fig1.b) during a certain interval of time. To achieve robustness, instead of individual signals³, packets of neighboring signals are considered. So, trafficking at a given voxel of the image is detected as significant *simultaneous* change in the fluorescence of a group of neighboring voxels. In the sequel, the whole methodology is described and some results on sequences of the RAB6A related cell membrane trafficking are shown.

2.2 A Model selection framework to simultaneous change detection in an ordered packet of 1D signals

Consider a group of M unidimensional signals $y_i, i = 1, \dots, M$. We suppose that each signal $y_i, i = 1, \dots, M$ can be decomposed as the sum of a deterministic

³ We mean by a signal the temporal profile of the fluorescence of a given image voxel.

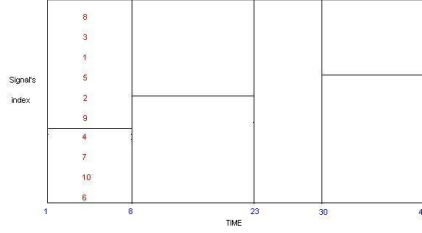


Fig. 2. An example of a spatio-temporal part ($N=40$, $M=10$). For instance, the first time part is $[1, 8]$ and consists of two spatio-temporal parts. The first spatio-temporal part is composed of the six signal indexes $\{8, 3, 1, 5, 2, 9\}$, and the second is composed of the 4 signal indexes $\{4, 7, 10, 6\}$

part S (expectation value) and a random part ϵ modeled as white Gaussian noise with standard deviation σ :

$$y_i(t) = S_i(t) + \epsilon_i(t), \quad i = 1, \dots, M, \quad t = 1, \dots, N \quad (1)$$

The question we will try to answer through this section is how one can estimate S only from data when S is piecewise constant in the spatio-temporal domain.

Designing models and building estimators for S : In the light of the ideas we presented in section 2, an *ideal* model for S captures all simultaneous jumps in the intensity of any sub-group of the M signals $y_i, i = 1, \dots, M$ and estimates exactly the corresponding intensity levels. Then a model for S spans the space \mathcal{M} of the piecewise constant functions defined in the spatio-temporal domain. So, consider a partition of the interval of time $[1, N]$ which we denote by \mathcal{T} . To each time interval $\tau \in \mathcal{T}$, we associate a partition of signal indexes \mathcal{I}_τ (cf. Fig2). Then a model for S is given by:

$$S_i(t) = \sum_{k=1}^{|\mathcal{T}|} \sum_{j=1}^{|\mathcal{I}_k|} U_{k,j} \mathbb{I}_{\mathcal{I}_{k,j}}(i) \mathbb{I}_{\mathcal{T}_k}(t) \quad (2)$$

where $U_{k,j}$ is constant in the spatio-temporal part $\mathcal{I}_{k,j}$, and $\mathbb{I}_{\mathcal{I}_{k,j}}(\cdot)$ stands for the indicator function. We assume that $|\mathcal{I}_k| \leq p$. Though our approach can work for an arbitrary p , herein, we consider only the case where $p = 2$ (a voxel either belongs to an object or to the background).

Now, let's construct estimators of S from data. For this, suppose we are given a spatio-temporal partition $m = \{\mathcal{I}_{k,j}, 1 \leq k \leq |\mathcal{T}|, 1 \leq j \leq |\mathcal{I}_k|\}$, and we want to build an estimator \hat{S}_m for S accordingly. If one chooses the \mathcal{L}^2 distance as a metric for assessing the quality of \hat{S}_m , then we have:

$$\hat{S}_m = \sum_{k=1}^{|\mathcal{T}|} \sum_{j=1}^{|\mathcal{I}_k|} \bar{S}_{k,j} \mathbb{I}_{\mathcal{I}_{k,j}}(i) \mathbb{I}_{\mathcal{T}_k}(t), \quad \text{where} \quad \bar{S}_{k,j} = \frac{1}{|\mathcal{I}_{k,j}|} \sum_{t \in \mathcal{T}_k} \sum_{i \in \mathcal{I}_{k,j}} y_i(t)$$

The dimension of an estimator \hat{S}_m is defined as the number of the spatio-temporal parts of the corresponding spatio-temporal partition $m : D_m = |m|$.

A penalized criteria for the estimation of S - Theoretical background:

Let \mathcal{M} be a family of models to which we associate a family $\mathcal{S} = \{\hat{S}_m, m \in \mathcal{M}\}$ of estimators of S . We seek for the estimator $\hat{S}_m \in \mathcal{S}$ which minimizes the quadratic risk $\mathbb{E}\|S - \hat{S}_m\|^2$. As $\mathbb{E}\|S - \hat{S}_m\|^2$ cannot be minimized directly from data [1][7], a sharp upper bound of this risk is minimized using data. A known approach in model selection literature is the penalized least squares criteria where one minimizes a criteria of the form:

$$\text{crit}(\hat{S}_m) = \gamma(\hat{S}_m) + \text{pen}(m) \quad (3)$$

where $\gamma(\cdot)$ stands for the \mathcal{L}^2 distance to the data y , and $\text{pen}(\cdot)$ stands for a penalty on the model complexity. Herein, we use the key result of Birgé & Massart [1] to give the form of $\text{pen}(m)$ and a risk bound of the penalized estimator of S which we denote by \tilde{S} .

Proposition 1 *There exist two positive constants $K > 1$ and $\theta > 0$ such that if the penalty is defined for all model $m \in \mathcal{M}$ by:*

$$\text{pen}(m) = K D_m \sigma^2 \left(1 + \sqrt{\theta + \frac{2 \log(\text{card}_{\mathcal{M}}(D_m))}{D_m}} \right)^2 \quad (4)$$

then the penalized estimator \tilde{S} satisfies:

$$\mathbb{E}\|S - \tilde{S}\|^2 \leq C(K) \inf_{m \in \mathcal{M}} \left\{ \|S - \bar{S}_m\|^2 + \text{pen}(m) \right\} + C'(K, \theta) \sigma^2 \quad (5)$$

where $\text{card}_{\mathcal{M}}(D)$ represents the number of the models $m \in \mathcal{M}$ having the dimension D , and \bar{S}_m is the projection of S on m ■

Proof. Recall the theorem of Birgé & Massart [1]:

Theorem 1 (Birgé and Massart) *Let's consider the Gaussian framework (1) and let define a family of non-negative weights $\{L_{m \in \mathcal{M}}\}$ satisfying:*

$$\Sigma = \sum_{m \in \mathcal{M} | D_m > 0} e^{-L_m D_m} < \infty. \quad (6)$$

Let's now consider a penalty function $\text{pen}(\cdot)$ satisfying:

$$\text{pen}(m) \geq K \sigma^2 D_m (1 + \sqrt{2L_m})^2 \quad (7)$$

for all $m \in \mathcal{M}$ and some $K > 1$, then the penalized estimator \tilde{S} exists almost surely and is unique. Moreover, it satisfies the following inequation:

$$\mathbb{E}\|S - \tilde{S}\|^2 \leq C(K) \inf_{m \in \mathcal{M}} \left\{ \|S - \bar{S}_m\|^2 + \text{pen}(m) \right\} + C'(K) \Sigma \sigma^2 \quad (8)$$

■

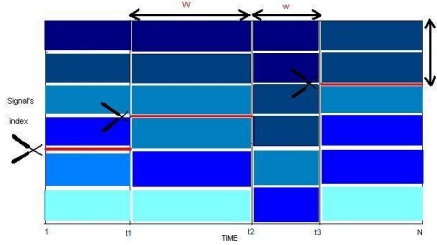


Fig. 3. An example of a spatio-temporal part belonging to \mathcal{M}^* . As shown by the figure, given a time partition of the time interval $[1, N]$, the average signal magnitudes with respect to each time part of the spatio-temporal partition are ordered in a descending order (from dark to light blue in the figure) and a spatio-temporal partition is obtained by dividing the signal indexes in each time part to one or to sets while respecting the so created spatial order in each time part.

Using this theorem, it amounts to find the (optimal) weights $\{L_{m \in \mathcal{M}}\}$:

$$\Sigma = \sum_{m \in \mathcal{M}} e^{-L_m D_M} = \sum_{D=D_{min}}^{D_{max}} e^{-L_D D} \text{card}_{\mathcal{M}}(D) = \sum_{D=D_{min}}^{D_{max}} e^{-D(L_D - \frac{\log \text{card}_{\mathcal{M}}(D)}{D})}$$

Put: $L_m = L_{D_m} = \theta + \frac{\log \text{card}_{\mathcal{M}}(D_m)}{D_m}$, for some $\theta > 0$, then we get:

$$\Sigma = \Sigma(\theta) = \sum_{D=D_{min}}^{D_{max}} e^{-D\theta} = \frac{e^{-D_{min}\theta} - e^{-(D_{max}+1)\theta}}{1 - e^{-\theta}}$$

We replace $\{L_{m \in \mathcal{M}}\}$ in (7) and $\Sigma(\theta)$ in (8), to establish the proof of the proposition 1 ■

Computing $\tilde{\mathcal{S}}$: Minimizing (3) on \mathcal{S} is quite an NP-hard problem. So, instead of minimizing (3) on \mathcal{S} , our idea is to minimize it only on a subset of \mathcal{S} that we think contains good candidate estimators of S .

We construct such candidate estimators as follows: First, we consider a time partition \mathcal{T} . For each time interval τ of \mathcal{T} , we compute the average intensity value for each signal of the packet of signals, and we order these mean values in a descending order. Indeed, it is natural to put together the signal segments with higher mean intensity values (very likely to correspond to the object) and together those with lower mean intensity values (corresponding to the background). Thus, the decision in each time interval τ on \mathcal{T} of the signal index where to cut the signals mean values into one or two sets yields a spatio-temporal partition (cf. Fig.3). The set of all such spatio-temporal partitions is denoted by \mathcal{M}^* and the associated set of estimators is denoted by \mathcal{S}^* .

Though there is still exponential number of candidate estimators of S (because $|\mathcal{M}^*|$ is exponential on M and N), the algorithm we present herein uses dynamic programming to compute $\text{card}_{\mathcal{M}^*}(D)$ and finds the best estimator of S (\mathcal{S}^*) for a given dimension $D, D_{\min} \leq D \leq D_{\max}$ in polynomial time. We denote it by \hat{S}_D . \hat{S}_D minimizes the sum of square differences to data among all the estimators of the class \mathcal{S}^* having the dimension D . Denote by: $\gamma(P)$ the cost (\mathcal{L}^2 distance to data) of a time-space part $P = \tau \times I$ after the ordering operation of the mean intensity values with respect to the time interval τ as we explained it earlier in this subsection, w and W are respectively the minimal and the maximal temporal lengths of a time-space part, h is the minimal spatial length (minimal number of signal indexes) of a time-space part⁴. We define $\hat{\Delta}_{t,D}$ and $C_{t,D}$ respectively as the cost of the minimal estimator and the cardinal of the set of the estimators of class \mathcal{S}^* of the part of data $\{y_i(s), i = 1 \dots, M, s = t, \dots, N\}$ having the dimension D . Then, we seek to compute $\hat{\Delta}_{1,D}$ (ie. the cost of \hat{S}_D) and $C_{1,D}$ (ie. $\text{card}_{\mathcal{M}^*}(D)$), for $D = D_{\min}, \dots, D_{\max}$. The following general recursive formulas allow their calculation, and because of lack of space, the dear reader must handle the initialization step (border terms).

$$\hat{\Delta}_{t,D} = \min_{\substack{\min(N-w, t+W-1) \geq u \geq t+w, \\ h \leq i \leq M-1}} \left\{ \gamma_{t,u,1,i} + \gamma_{t,u,i+1,M} + \hat{\Delta}_{u+1,D-2}, \gamma_{t,u,1,M} + \hat{\Delta}_{u+1,D-1} \right\},$$

$$N - W + 1 \leq t \leq N - w + 1, D_{\min} \leq D \leq D_{\max}$$

$$C_{t,D} = \sum_{\min(N-w+1, t+W-1) \geq u \geq t+w} C_{u,D-1} + (M - h) \times C_{u,D-2},$$

$$N - W + 1 \leq t \leq N - w + 1, D_{\min} \leq D \leq D_{\max}$$

Once one has computed \hat{S}_D and $\text{card}_{\mathcal{M}^*}(D)$ for $D = D_{\min}, \dots, D_{\max}$, (3) is minimized with respect to D to find \hat{S} .

Method calibration: K and θ are trade-off parameters in (5). We adjusted K to 2 and θ to 2 by simulation. For σ which is assumed to be known so far, we propose a fast and simple method for its estimation. As we assumed that the variance of the 2D signal y is the same as the variance of each of its constituting 1D signals $y_i, i = 1, \dots, M$, then, let's first estimate the variance σ_i^2 of y_i . Define $z_i(t) = y_i(t+1) - y_i(t), t = 1, \dots, N-1$. Let's now consider $z_i^*(t) = z_i(2t-1), t = 1, \dots, \lfloor \frac{N+1}{2} \rfloor$ and $z_i^{**}(t) = z_i(2t), t = 1, \dots, \lfloor \frac{N}{2} \rfloor$. If there was no significant fluorescence change in the signal y_i , than both $z_i^*(t), t = 1, \dots, \lfloor \frac{N+1}{2} \rfloor$, and $z_i^{**}(t), t = 1, \dots, \lfloor \frac{N}{2} \rfloor$ would be *i.i.d* Gaussians with variance $2\sigma_i^2$. In presence of significant fluorescence change due to vesicle trafficking, both $z_i^*(t), t = 1, \dots, \lfloor \frac{N+1}{2} \rfloor$ and $z_i^{**}(t), t = 1, \dots, \lfloor \frac{N}{2} \rfloor$ may be viewed as *i.i.d* Gaussians with variance $2\sigma_i^2$ but contain outliers. Thus, a robust estimator of $2\sigma_i^2$ is needed. A good robust estimator of the standard deviation s of Gaus-

⁴ w, W and h are by default respectively equal to 1, N , and 1, but may also be set accordingly to trade off robust detections and fast calculations.

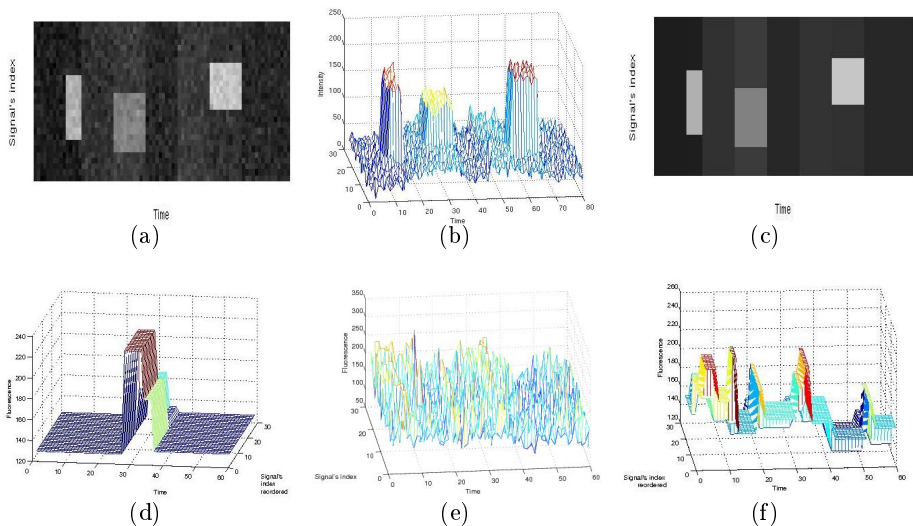


Fig. 4. (a) Image representation of a simulated 2D piecewise constant Gaussian signal ($\sigma = 10$); (b) Topographical representation of the 2D signal in (a); (c) Image representation of the restored 2D signal ($w = 1, W = 15, h = 6$); (d) A 3D representation of the observed trafficking (penalized estimator (up to a spatial reordering)) for the signal packet of Fig1.b ($w = 1, W = 60, h = 6$). The algorithm found that $\tilde{S} = \hat{S}_6$; (e) A packet of the 27 signals of a site X with heavy background; (f) The corresponding penalized estimator (up to a spatial reordering) ($w = 1, W = 10, h = 6$).

sian process $\epsilon_t, t = 1, \dots, K$ is: $\hat{s} = 1.48 \times \text{Median}\{|\epsilon_t|, t = 1, \dots, K\}$. So, two estimators of $\sqrt{2}\sigma_i$ is: $\hat{s}_1 = 1.48 \times \text{Median}\{|z_i^*(t)|, t = 1, \dots, [\frac{N+1}{2}]\}$ and $\hat{s}_2 = 1.48 \times \text{Median}\{|z_i^{**}(t)|, t = 1, \dots, [\frac{N}{2}]\}$. It follows that an estimator of σ_i is: $\hat{\sigma}_i = \frac{\hat{s}_1 + \hat{s}_2}{2\sqrt{2}}$, and finally an estimator of σ can be: $\hat{\sigma} = \text{Median}\{\hat{\sigma}_i, i = 1, \dots, M\}$.

3 Experimental results

To assess the performance of our bidimensional signal technique, we first experimented it on simulated 2D signals for realistic SNRs. Unless the 2D signal is severely damaged by noise, the method successfully restores it (*cf.* Fig4.a-c). Second, we sampled manually many image sites where we can see object trafficking, and we applied the method on the corresponding signal packets. The obtained results have been very encouraging (*cf.* Fig4.d-f).

We used the developed approach to analyse videomicroscopic sequences of the RAB6A related vesicle trafficking. These sequences of size $395 \times 345 \times 10$ voxels³ \times 120 seconds were acquired using the wide-field modality and are coded in short (intensity values range from a few tens to a few thousands).

3.1 Detection of activity regions

First, we divided the 3D volume into blocks (sites) of size $3 \times 3 \times 3$ and we treat at once $N = 60$ instants. For each voxel of a site, we consider the corresponding signal y_x . To decide whether or not there is vesicle trafficking at some site X , we use *a contrario* hypothesis testing (Desolneux et al., 2000). For each voxel x of X , we consider the null hypothesis $H_0(x)$: "No trafficking occurs at voxel x " and the alternative hypothesis $H_1(x)$ "There is trafficking at voxel x ". Noise is assumed to be Gaussian, so let's consider the statistic $T_x = \frac{\sum_{t=1}^N (y_x(t) - \bar{y}_x)^2}{\sigma_x^2}$,

where $\bar{y}_x = \frac{1}{N} \sum_{t=1}^N y_x(t)$ and σ_x^2 is the signal variance. Notice that the statistic T_x increases as there is significant changes in the fluorescence profile y_x of the voxel x . Under $H_0(x)$, T follows a χ^2 distribution with degree of freedom $N - 1$. So, we fix a p -value α (eg. $\alpha = 5\%$), and we determine the quantile A_x such that $\mathbf{P}(T_x \geq A_x/H_0(x)) = \alpha$. Finally, we decide to select the site X if $T_x \geq A_x$ for at least six voxels x of X . For instance, for the sequence shown in Fig1.a, around 15.900 of image sites (cf. Fig5.a) were detected ($\alpha = 5\%$).

Remark. In presence of highly spiky noise (which is generally the case for raw videomicroscopic sequences), to avoid false alarms in the test output, we recommend either to use a fix σ characteristic of trafficking sites, for all the signals in the sequence, or estimate σ_x as explained at the end of section 2 but filter the sequence (using eg. the median filter) to eliminate the spikes before performing the test on each signal y_x of the sequence.

3.2 Spatio-temporal vesicle localization & trafficking analysis

The described approach is applied on the so detected sites. Following our modeling, detecting vesicle trafficking at a site amounts to take the higher mean value in each time interval of the found optimal spatio-temporal partition (this induces a 1D function we denote by F)(cf. Fig5.b) and detecting significant changes in the intensity of F . So, background can be viewed as the valleys while object passages can be viewed as the significant hills in the profile of F . The detection of the hills and the valleys in F can be performed with the 1D watershed transform. To handle small background changes (due to eg. dynamic background, photobleaching, etc. . .), some post-processing aiming at discarding insignificant hills in F detected with the 1D watershed transform F is necessary (cf. Fig5.c).

Once this preliminary analysis is performed, moving spots are detected at each time instant as spatial connected components (cf. Fig6). The strength of such a detection is that, contrarily to wavelet based detection and to Gaussian kernel fitting which simply fail in case of anisotropic and collapsing spots, this method is able to detect moving spots whatever their shape. Furthermore, the temporal windows (temporal lengths of the significant hills in F) are used to track locally (with respect to a given image region) the moving spots, and statistics regarding their dynamics can be computed accordingly (eg. cf. Fig.7).

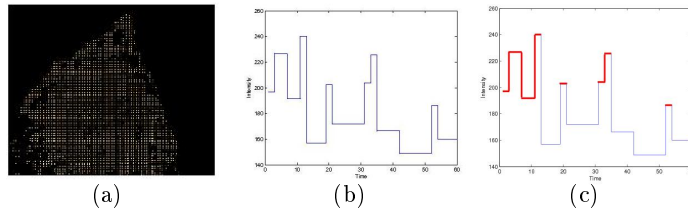


Fig. 5. (a) A 2D slice of the 3D binary image of the detected trafficking sites (in white) ($\alpha = 5\%$) ; (b) Constructing the 1D function F for the example of Fig4.f ; (c) Detection by the watershed transform of F of vesicle trafficking at the site X . As shown in the figure, four vesicle passages are detected (colored in red).

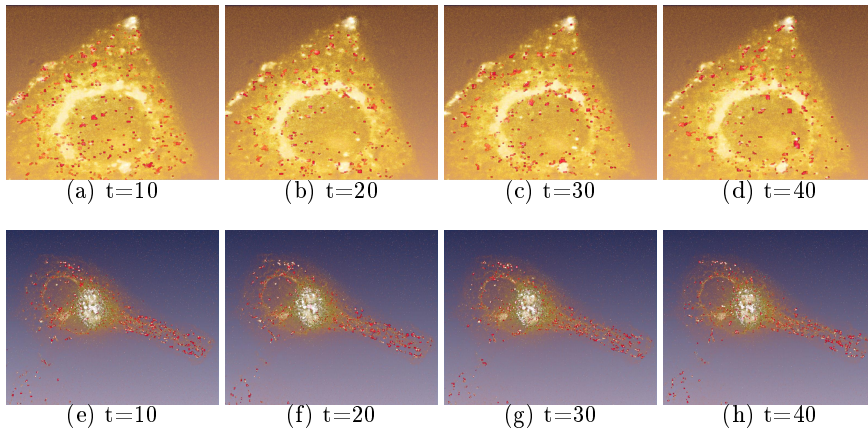


Fig. 6. Spatio-temporal detection of moving spots (colored in red) corresponding to the trafficking of the GFP-tagged RAB6A protein between Golgi apparatus and ER cell compartments (a) In a 3D+T raw videomicroscopic sequence ; (b) In a 3D+T deconvoluted videomicroscopic sequence.

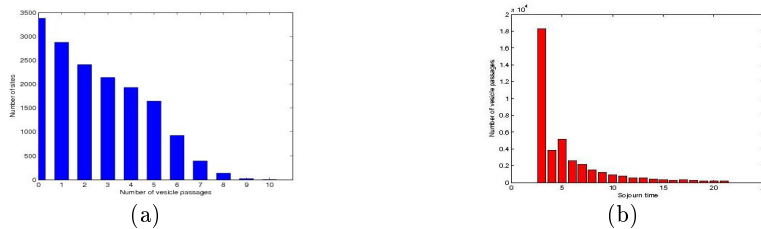


Fig. 7. (a) The histogram of trafficking intensity ; (b) The histogram of sojourn times of vesicles (carrying the GFP-tagged RAB6A protein) in the detected activity sites.

4 Conclusion & perspectives

We presented an automatic approach for spatio-temporal analysis of vesicle trafficking in 4D videomicroscopy. It constitutes an interesting framework for summarizing the huge spatio-temporal data and performing statistical analysis of dynamics in 4D videomicroscopy without the need to track individually the objects in the scene. We used the developed approach to analyze the RAB6A protein related vesicle trafficking. Now, we are constructing high level representations of vesicle dynamics based on the described bidimensional signal processing technique and on graph theory. This aims at developing a GUI (Graphical User Interface) that allows the user to navigate intelligently in the spatio-temporal content of the sequence, focus on special sites, select special dynamics, visualize particular events, add missing information by simple clicks in the image, etc ...

5 ACKNOWLEDGMENTS

The authors are grateful to V. Racine, J. Salamero, and J.B. Sibarita of the team *Compartments and cell dynamics - UMR 144 CNRS/Curie Institute of Paris*, for providing us with the 4D raw and deconvoluted videomicroscopic sequences we used in this work.

References

1. Birgé, L. and Massart, P. Gaussian Model Selection. *J. European Math. Soc.*3, pp.203-268, 2001.
2. Boulanger, J. ; Kervrann, C. and Bouthemy, P. An adaptive statistical method for 4D fluorescence image sequences denoising with spatio-temporal discontinuities preserving. *Proc. Int. Conf. Image Processing (ICIP'05)*, Genova, Italy, 2005.
3. Boulanger, J. ; Kervrann, C. ; Bouthemy, P. Estimation of dynamic background for fluorescence video-microscopy. *In Proc. Int. Conf. Image Processing (ICIP'06)*, Atlanta, USA, 2006.
4. Desolneux, A. ; Moisan, L. and Morel, J.M. Meaningful Alignments, *International Journal of Computer Vision*, Vol.40(1), pp.7-23, 2000.
5. Genovesio, A.; Belhassine, Z.; Olivo-Marin, J-C. Adaptive Gating in Gaussian bayesian Multi-Target Tracking. *Int. Conf. Image Processing (ICIP'04)*, Vol.1, pp.147-150, Singapore, 2004.
6. Ji L., and Danuser G. Tracking quasi-stationary flow of weak fluorescent signals by adaptive multi-frame correlation. *J. Microscopy*. 220, pp. 150-167, 2005.
7. Lebarbier, E. Detecting multiple change-points in the mean of Gaussian process by model selection. *Signal Processing* 85, pp.717-736, 2005.
8. E. Meijering, I. Smal, G. Danuser. Tracking in Molecular Bioimaging. *IEEE Signal Processing Magazine*, vol. 23, no. 3, pp. 46-53, 2006.
9. Miura, K. Tracking Movement in Cell Biology. *Advances in Biochemical Engineering/Biotechnology*, vol.95, p267 Springer Verlag, 2005.
10. Sibarita, J.B. ; Racine, V. and Salamero, J. Quantification of membrane trafficking on a 3D cytoskeleton network in living cells, *In Proc. Int. Symp. on Biomedical Imaging (ISBI'06)*, Arlington, USA, 2006.

Characterization of Pre- and Postoperative Macular Holes from Retinal OCT Images

Jakob Thomadsen¹, Thomas Martini Jørgensen², Ulrik Christensen³, Kristian Krøyer³, Bjarne Kjær Ersbøll¹, and Rasmus Larsen¹

¹ Informatics and Mathematical Modelling, Technical University of Denmark, Denmark,

² Optics and Plasma Research Department, Risø National Laboratory, Denmark,

³ Department of Ophthalmology, Herlev Hospital, Denmark

Abstract. A set of interactive tools have been developed to assist in the extraction of macular hole descriptors in retinal optical coherence tomography images. Due to differences in the shape of the pre- and postoperative retinal surface, two different methods are applied. The localization of transitional borders is based on regularized shortest-path extraction except for the retinal surface in preoperative images, where a parametric snake is applied, since the retinal surface is not single-valued as a function of the retinal position. The tools make extraction of relevant descriptors less time consuming and more accurate.

1 Introduction

For a number of eye diseases, the pathological changes are localized in the retina. This is the case for diabetic retinopathy and glaucoma, but also for less known diseases such as macular hole, where a rupture happens in the central part of the retina. Since this is where our sharpest vision is localized, a macular hole leads to a significant loss of central vision on the affected eye.

Only few full-thickness macular holes close spontaneously. Surgery is currently the only way to treat a macular hole that does not close spontaneously. It was discovered in 1999 as reported in [1] that peeling of the internal limiting membrane (ILM) on the retina has been found to be a way to stimulate the wound healing. This is an extremely difficult procedure, but the challenge for the surgeons can be greatly reduced if the membrane is stained with the dye indocyanine green (ICG). There are concerns that ICG may be toxic to the retina, but on the other hand if the ILM is not peeled, there is a higher risk of the hole not closing [2].

Optical coherence tomography (OCT) is an often used method to visualize the retina. OCT is an imaging technique developed in the early nineties that can produce high-resolution cross sectional images of the internal microstructure of living tissue [3]. OCT has conceptually many similarities with ultrasonic imaging, the major difference being the use of coherent light instead of ultrasound.

Currently a research project at a collaborating hospital is performing a randomized clinical trial comparing different surgical techniques for the treatment

of macular holes. Half of the patients will have performed ICG-assisted ILM peeling, and the other half will not. An important method used in evaluating the results is OCT. To quantitatively be able to evaluate the changes occurring in the retina, it is relevant to look at several measurable descriptors in the OCT images. A set of relevant descriptors have been decided in collaboration with the relevant personnel from the department of ophthalmology at the collaborating hospital. To assist in the data processing, two interactive tools have been developed that extract these descriptors.

The primary goal of the research project is to evaluate the surgical results achieved with ICG assisted ILM peeling, vs. no peeling. During the trial, insight about the pathogenesis of macular hole may also be gained. This could for instance be about which macular holes spontaneously regress and which do not. Then surgery could be performed earlier for the holes not expected to regress.

The retinal layers that will be referred to below are indicated on an OCT image of a normal case in figure 1. An example of a macular hole can be seen in figure 3.

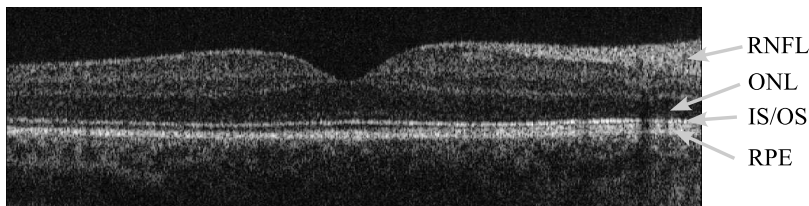


Fig. 1. Relevant retinal layers shown on an OCT image. Starting from the inner part of the eye, they are: retinal nerve fiber layer (RNFL), outer nuclear layer (ONL), inner and outer segment of the photoreceptors (IS/OS) and the retinal pigment epithelium (RPE).

2 Method

Two types of images will be available, one being preoperative images with a macular hole, and the other being postoperative images, which for the main part will be similar in shape to a normal retina. Different descriptors are to be determined for the two cases, so two different methods have been developed.

2.1 Pre-Operative Images

In order to determine the relevant descriptors in the preoperative case, the inner (closest to the eye) and outer transition of the neuroretina needs to be located. The neuroretina refers to the retina excluding the retinal pigment epithelium

(RPE). Thus the inner transition is between the vitreous body and the retinal nerve fiber layer (RNFL), and the outer is where the inner and outer segments of the photoreceptors (IS/OS) and the RPE connects. Since it can be very difficult to locate the precise transition between the RPE and IS/OS, an often used approximation is to use the transition between the outer nuclear layer (ONL) and the IS/OS. In the following a reference to the neuroretinal thickness will refer to this approximate thickness.

The outer transition can be found as a shortest-path running from the left to the right in the negated vertical gradient image. This has been implemented with regularized shortest-path extraction as described in [4]. The method is an extension of dynamic programming that constrains the second order derivative of the path, but still maintains optimality. The cost of the path that is minimized consists of two parts, the first being the intensity of the pixels the path crosses and the second being the second order derivative of the path,

$$\sum_{c=1}^M I(i_c, c) + \lambda \sum_{c=2}^{M-1} (i_{c-1} - 2i_c + i_{c+1})^2. \quad (1)$$

I is the image and i_c is the corresponding row of the path location in column c . A regularization constant λ is introduced that controls the rigidity of the path. It has been set to 10% of the maximum pixel value. In this way the cost is approximately independent of scaling of the image intensities.

This procedure fails for some cases, where the tracked path jumps down and locates the inner part of the RPE instead of the IS/OS. An extra energy term could be added that penalized lower lying pixels, but this could also shift the location of the shortest path upwards in the cases where the top has been correctly found. Therefore another approach is taken. First the center of the RPE is located with regularized shortest-path extraction. The inner part of the IS/OS is expected to lie between 40 and 60 μm above the central line, and the inner part of the RPE is expected to lie below 40 μm . If there is a significant peak in the gradient image, lying in the interval 40-60 μm above the central line, it and its vertical vicinity is rewarded, thus attracting the shortest-path.

An example where this corrects an otherwise erroneous path can be seen in figure 2. The white path, indicating the altered path, has been pulled upwards from the black path, to correctly find the outer neuroretinal transition on the right side, without otherwise affecting the path. If for some reason this method or any of the other methods based on shortest-path extraction fails, the user can reward a point on the image and thereby attract the shortest-path towards the point.

In contrast to the above situation with no macular hole, the inner border in the case of a macular hole will not be single-valued as a function of the retinal position. In such a case we cannot apply our shortest-path algorithm. Instead we apply a parametric snake algorithm. For further information on, and how to implement a snake see [5].

Since the surface of the retina is not a closed curve, the snake is adapted, such that it always starts at one side of the image and ends at the other side. By

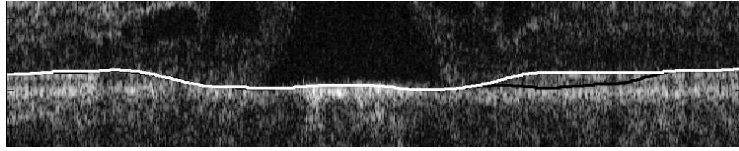


Fig. 2. The shortest path found in the negated gradient image is marked with black. To correctly find the top of the IS/OS, indicated by a white line, a high gradient lying in the interval $40\text{-}60\mu\text{m}$ above the center of the RPE has been rewarded.

letting a balloon force be directed perpendicular to the snake in the downwards direction, the snake will have greater chance of extending to corners of the macular hole. This only gives good results if the snake is initialized at or above the border it should fall to rest on.

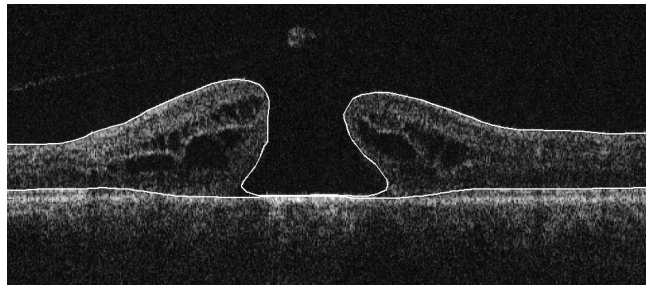


Fig. 3. The locations of the inner and outer transitions of the neuroretina are shown.

In figure 3 the located borders of a neuroretina are shown. The inner transition is located on the basis of 10 points provided by the user.

From the location of the inner and outer borders of the neuroretina the relevant hole descriptors can be extracted. The descriptors are the height of the hole, minimum and maximum width of the hole, an estimate of the area and volume of the hole and an estimate of the neuroretinal area.

2.2 Post-Operative Images

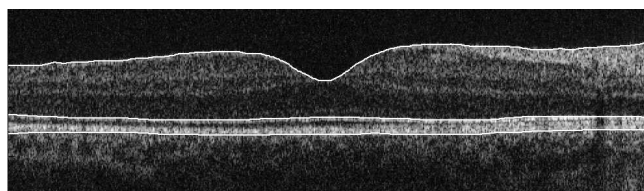
A postoperative OCT image is shown in figure 4(b), and compared to a normal subject, shown in figure 4(a). There are several things to look for when assessing how well the retina has rejuvenated. The apparent difference at the top right position showing a thick RNFL (indicating it is close to the optical nerve head and the nasal direction) for the normal subject is simply caused by this OCT scan being recorded at an angle close to horizontal.

Three factors that may indicate a loss of visual acuity in the fovea will be mentioned in the following. It can be seen that the hyperreflective layer in the fovea has decreased in thickness. It consists not only of the RPE as previously mentioned, but also of the IS/OS. In the postoperative image this layer has completely disappeared in the foveal area. This indicates that the photoreceptors may have been decomposed in the detachment period.

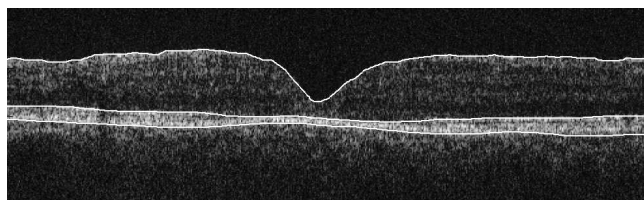
The "foveal dip" is significantly deeper in the postoperative image. Since the significant layer present in the fovea lying above the IS/OS is the ONL, consisting of the cell bodies of the photoreceptors, it indicates that the photoreceptors have shrunk or completely disappeared. These two features have been investigated before in [6], where there were indications of the IS/OS thickness correlated with visual acuity but not the foveal thickness.

The last factor that indicates a significant loss of visual acuity in the postoperative image is the increased intensity of the ONL in the fovea. It can be seen that the layer in the fovea lying above the RPE has an increased intensity when compared to the non-foveal area in the same image, or the foveal area in the normal eye. This could indicate that instead of being rejuvenated photoreceptors it may be scar tissue.

These three factors, are to be determined quantitatively and automatically. To achieve this, the same two transitions as were located in the preoperative case need to be located, along with the location of the outer boundary of the RPE. All these transitions can be located with regularized shortest-path extraction. To increase the robustness, the center of the RPE is located before the inner and outer transitions, such that the search space can be constrained. The three transitions located are shown for two different cases in figure 4.



(a) Normal eye



(b) Postoperative macular hole

Fig. 4. The inner and outer transitions of the neuroretina are outlined, along with the outer transition of the RPE.

From these three transitions, the thickness of the neuroretina and the thickness of the layer consisting of the IS/OS and RPE can be found, and the ONL can be sampled at different locations.

3 Results

The methods have been tested on a preliminary set consisting of six preoperative and six postoperative images, to indicate whether or not the methods cover the variation present. The localized transitions achievable in both the pre- and postoperative cases are satisfactory. A set of screen captures of the tools are shown in figure 5.

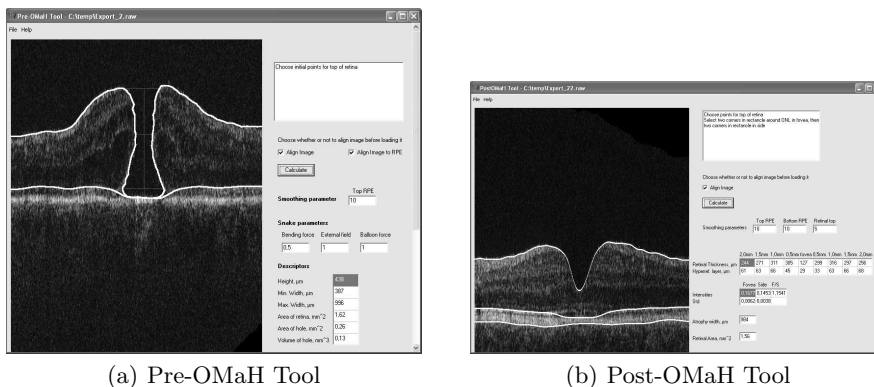


Fig. 5. Screen captures of the two tools developed.

The preliminary test case shown in figure 4(b) has been compared to a normal case. The neuroretinal thickness, the RPE+IS/OS thickness and ONL intensities are shown in figure 6. They have all been plotted as a function of the position. The graphs show significant differences between the postoperative macular hole and normal case. Figure 6(a) gives the impression that the postoperative case has a depleted retina, particularly around the fovea. In figure 6(b) the RPE+IS/OS thickness is significantly thinner in the macular area of the postoperative case, indicating an atrophy and thus a loss of photoreceptors. Finally figure 6(c) shows a gaussian filtered version of the intensity of the ONL. The macular area of the postoperative case has a significantly higher intensity than the ONL lying outside the macula, and also higher than in the normal case. This indicates the tissue may be other types of tissue, such as scar tissue instead of cell bodies of the photoreceptors. These indications corresponds well with the fact that this individual has a worse postoperative visual acuity than other test cases that are visually more similar to the normal case.

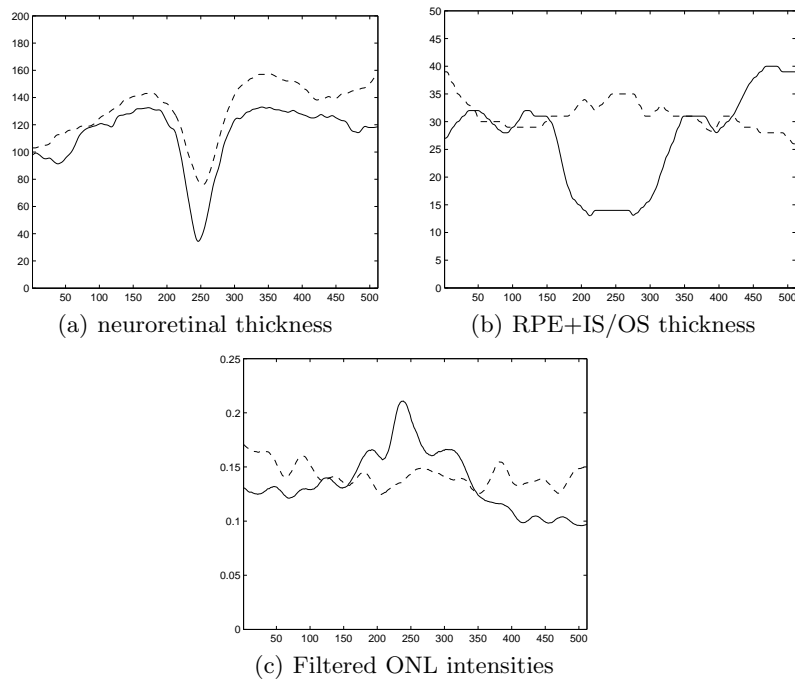


Fig. 6. Comparison between a normal case and a postoperative macular hole. (a) gives the impression that the postoperative case has a depleted retina. In (b) the atrophic area can be seen in the central part of the graph. (c) shows that the ONL in the macular area has a higher intensity than the ONL lying outside the macula, and also higher than in the normal case.

4 Conclusion

A set of interactive tools have been developed to assist in the extraction of descriptors in OCT images of pre- and postoperative macular holes. The tools make extraction of relevant descriptors less time consuming and more accurate. To localize the descriptors, a set of transitional layers need to be located. This is achieved by the use of regularized shortest-path extraction and a parametric snake in the case of the inner retinal border, since the inner retinal border is not single-valued as a function of the retinal location. There are initial indications that the outcome of the surgery can be assessed from the descriptors extracted from postoperative OCT images.

References

1. Madreperla, S., McCuen, B.I.: Internal limiting membrane removal in surgery for full-thickness macular holes. In: *Macular Hole. Pathogenesis, Diagnosis and Treatment*. Boston: Butterworth Heinemann (1999) 125–146
2. Brooks, H.L.: Macular hole surgery with and without internal limiting membrane peeling. *Ophthalmology* **107**(10) (2000) 1939–1948
3. Huang, D., Swanson, E.A., Lin, C.P., Schuman, J.S., Stinson, W.G., Chang, W., Hee, M.R., Flotte, T., Gregory, K., Puliato, C.A., Fujimoto, J.G.: Optical coherence tomography. *Science* **254**(5035) (1991) 1178–1181
4. Buckley, M., Yang, J.: Regularised shortest-path extraction. *Pattern Recognition Letters* **18**(7) (1997) 621–629
5. Kass, M., Witkin, A., Terzopoulos, D.: Snakes: active contour models. *International Journal of Computer Vision* **1**(4) (1987) 321–31
6. Villate, N., Lee, J., Venkatraman, A., Smiddy, W.: Photoreceptor layer features in eyes with closed macular holes: Optical coherence tomography findings and correlation with visual outcomes. *American Journal of Ophthalmology* **139**(2) (2005) 280–289

Texture and wavelet based lesion classification using color images

Artur Chodorowski¹, Chitta R. Choudhury², and Tomas Gustavsson¹

¹ Signals and Systems, Chalmers University of Technology, Sweden,
artur@s2.chalmers.se, gustavsson@s2.chalmers.se

² Oral Biology, AB Shetty Memorial Institute of Dental Sciences, Deralakatte, Mangalore, India and International Centre For Tropical Oral Health, England, cr_choudhury@yahoo.co.uk

Abstract. We analyzed the true color images of human oral cavity with respect to potentially precancerous oral lesions. The aspect of the analysis was texture of the lesions. The images of the lesions were decomposed using 2D wavelet transform and the resulting wavelets coefficients were taken as parameters to extract textural features. The analysis was performed on hue, saturation and intensity color bands. 48 color images with known diagnoses were analyzed and used to build a supervised classification system. The overall classification accuracy was 81% (39 out of 48) using Support Vector Machine classifier.

1 Introduction

The oral mucosa is the site of a variety of disorders and more than two hundred diseases have been diagnosed. Some of the lesions have a potential to develop into cancer, which means that we need to monitor these lesions. The visual examination of patient's oral cavity is in fact the first step in the diagnostic process and has a great impact on further diagnostic evaluation and possible treatment of the patient. Many biophotonic methods, such as multispectral and spectroscopic analysis, optical coherence tomography and TeraHz imaging, have been proposed to investigate oral lesions tissues [1][2][3]. However, the common method of preliminary investigation is still the true color imaging using digital color cameras. This is due to its simplicity and the low cost, which is important for spreading the technique to the developing countries. In fact, one of the countries suffering most from the oral cancer is India and their neighbouring countries [4].

In this work we analyze the color images of oral mucosal lesions, with respect to the texture of the lesions and the clinical diagnosis. The texture parameters are in turn taken to build a supervised classification system, to discriminate between potentially cancerous and harmless lesions. Such a system could be used as diagnostic support system for oral lesion investigations.

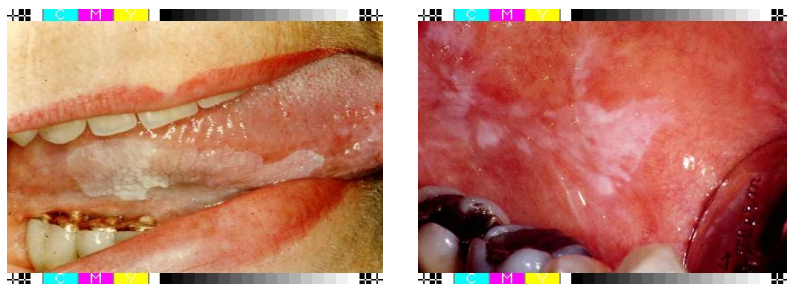


Fig. 1. (left) Leukoplakia - potentially pre-cancerous lesion, many leukoplakias show a patch-like structures, (right) Lichenoid reaction - usually harmless lesion, with smooth structures.

2 Material and methods

The material for this study was derived from patients treated at the Central Hospital, Karlstad, Sweden. The intraoral macrophotographs (1:1) were taken of the lesions before biopsy and all diagnoses were histologically verified. The images were represented by 768x512 pixels, 24 bits per pixel, 8 bits per color channel (red, green, blue). In total, we analyzed 48 images, 24 case of oral leukoplakia and 24 cases of oral lichenoid reactions. The images in Figure 1 show examples of potentially precancerous lesion (leukoplakia) and usually harmless lesions (lichenoid reactions). In contrast to lichenoid reactions, many of leukoplakias exhibit a patch-like structures.

The RGB values were transformed to HSI (Hue-Saturation-Intensity) color system using the following equations: $Hue = atan2(Y, X)$, where $X = (2R - G - B)$, $Y = \sqrt{3}(G - B)$, $Saturation = 1 - \min(R, G, B)/(R + G + B)$, $Intensity = (R + G + B)/3$, as they better correspond to the human perception of colors [5].

The feature extraction process is as follows (see Figure 2) :

- a) the user manually selects a representative part of the lesion and extracts a quadratic 32x32 pixels area
- b) the extracted image is converted to a log-polar representation, to obtain rotation and nearly scale invariance of wavelet coefficients [6]
- c) the image is converted to hue, saturation and intensity bands [5]
- d) the resulting images are decomposed by 3-level 2D wavelet transform into approximation and detail wavelet coefficients, using 2D Haar mother wavelet and row shift invariant transform [6]
- d) from wavelet decomposition, two rotation invariant features are extracted: variance $Var(C_k)$ and energy $E(C_k)$, where C_k is a subimage k . Here subimage C_k consisted of both original coefficients and coefficients calculated for one row shifted log-polar image.

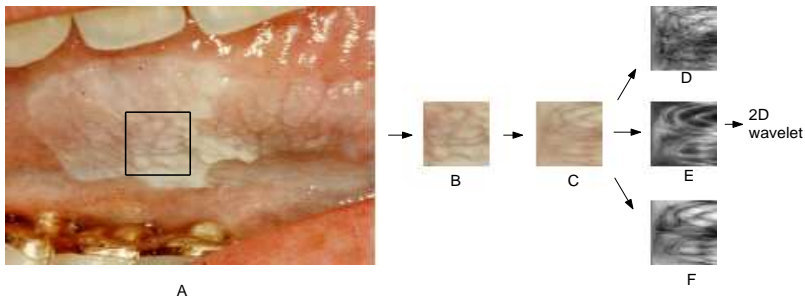


Fig. 2. Decomposition of rotation and scale invariant wavelet coefficients from a color image: (A) original image with region of interest ROI marked (B) extracted ROI (C) ROI converted to log-polar representation (D) hue log-polar band (E) saturation log-polar band and (F) intensity log-polar band. Here hue, saturation and intensity values are stretched for visualization purpose.

The 3-level wavelet decomposition produces in total 10 subimages, thus the feature vector F consisted of 10 energy and 10 variance values, for every color band:

$$F_i = \{Var(C_1) Var(C_2) \dots Var(C_{10}) E(C_1) E(C_2) \dots E(C_{10})\}$$

where $i \in \{Hue, Saturation, Intensity\}$. Here indices 1..4 indicate the last decomposition level, 5..7 to the next higher level and 8..10 the second higher level.

The feature selection was done by forward selection based on Wilks' lambda as discriminatory measure. This was done individually for every color band and then the most discriminatory features were used for classifier design. The classification was performed using Support Vector Machines (SVMs) [7], and the following decision function:

$$f(\mathbf{x}) = sgn\left(\sum_{i=1}^l \alpha_i y_i K(\mathbf{x}_i, \mathbf{x}) + b\right) \quad (1)$$

where (\mathbf{x}_i, y_i) are training examples, \mathbf{x} is a sample to be classified, l is number of training examples, K is a kernel function, b is bias, α_i are the solutions to the associated quadratic programming problem, $\alpha_i \leq C$, and C is a penalty parameter chosen by the user.

3 Results

3.1 Classification results

In this section, we present a number of classification experiments in which SVMs are used to the two-class oral lesion problem. The aim was to find a penalty parameter C and the kernel K with the best generalization ability. The classifier performance was evaluated using leave-one-out cross-validation. During the classifier training the leukoplakia cases were labeled as $\{+1\}$ and the lichenoid reactions were labeled as $\{-1\}$.

Table 1 shows total leave-one-out classification errors using two the best wavelet features and polynomial and radial basis functions (RBF) kernels. Table 2 presents corresponding results using an additional parameter in the feature vector. We observe that that the best results are for linear-SVMs. The total error using three features is slightly lower than for two features (15% vs. 19%), but due to the low number of available training data this difference is not statistically significant.

Table 1. Leave-one-out crossvalidation error rates (%) for linear, polynomial and rbf-SVMs, using the two most discriminatory features: intensity variance $Var(C_4)$ and saturation variance $Var(C_4)$, $\dim(X)=2$.

Kernel type	$C = 0.1$	$C = 1$	$C = 10$	$C = 10^2$	$C = \infty$
linear	19	22	25	25	25
poly d=2	29	31	29	29	29
RBF $\sigma = 0.25$	31	31	31	45	45
RBF $\sigma = 0.5$	31	33	45	47	47
RBF $\sigma = 1$	29	29	29	43	43

Table 2. Leave-one-out crossvalidation error rates (%) for linear, polynomial and rbf-SVMs, using the three features: intensity variance $Var(C_4)$, saturation variance $Var(C_4)$ and intensity energy $E(C_5)$, $\dim(X)=3$.

Kernel type	$C = 0.1$	$C = 1$	$C = 10$	$C = 10^2$	$C = \infty$
linear	23	18	15	15	18
poly d=2	25	27	21	21	23
poly d=2	25	27	21	21	23
RBF $\sigma = 1$	31	22	31	31	37
RBF $\sigma = 0.5$	29	29	33	33	39

3.2 Receiver Operating Characteristics

Figure 3 shows the ROC curves for the leukoplakia vs. lichenoid reactions problem for the two classifiers. The ROC curve have been generated by varying the classifiers' bias term. Both classifiers show a similar performance and have difficulty to obtain high sensitivity and high specificity simultaneously. In particular, for nearly 100% specificity, the sensitivity drops down to 30%.

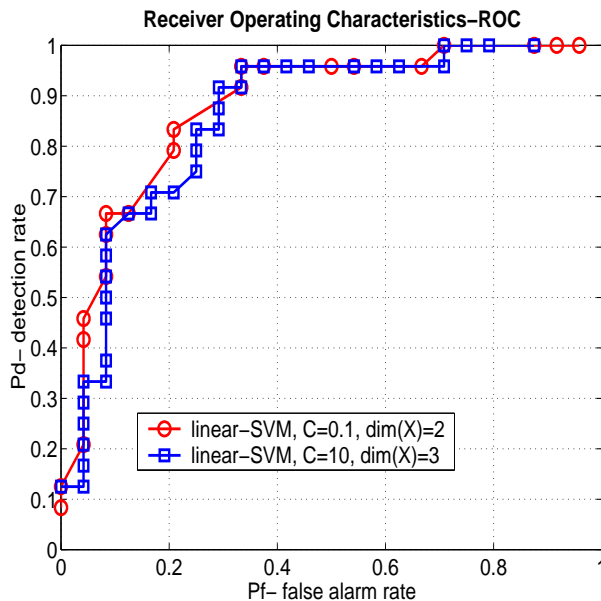


Fig. 3. ROC curve for linear SVM ($C=0.1$, $\dim(X)=2$) and linear SVM ($C=10$, $\dim(X)=3$), Pd is detection rate (sensitivity) for leukoplakia, Pf is false alarm rate (1-specificity) for lichenoid reactions. Leave-one-out crossvalidation rates.

4 Conclusion

The presented method has too low accuracy to be used at clinical practice. The most interesting points of the ROC curves are where both sensitivity and specificity are high, and are difficult to approach using the presented method. Tumor detection schemes using textural information have been proposed for various tissues [8] [9]. The wavelet features are usually selected after some unsupervised dimension reduction method based on energy or entropy measures. Our method differs from others, that the choice of the suitable combination of wavelet features is done during the classifier feature selection.

Potential improvements may be done by combining true color imaging with other recording modalities such as multispectral imaging and optical coherence tomography and including other non-textural features. The extension to multispectral data will put even more attention on feature selection and data reduction to avoid overfitting. Currently, we collect data from AB Shetty Memorial Institute of Dental Sciences, India, to investigate the classification method on Indian cases and compare them with the results obtained on the Nordic population. These images are being recorded with higher resolution, which will make it possible to closer investigate lesions' texture.

References

1. Dhingra, J.K., Perrault Jr., D.F., McMillan, K., Rebeiz, E.E., Shapshay, S.M., Manoharan, R., Itzkan, I., Feld, M.S., Kabani, S.: Spectroscopic analysis of pre-cancerous and cancerous lesions of the oral cavity. *Lasers and Electro-Optics Soc Ann Meeting, IEEE* **1**(18-19) (1996) 332–333
2. Jen Hsu, I., , Lu, C.W., Lin, S.M., Yang, C.C., Chiang, C.P., Lin, C.W., Kiang, Y.W.: Imaging of the oral cancer tissues with optical coherence tomography using self-phase modulation in fiber for broadband source generation. *Lasers and Electro-Optics, The 4th Pacific Rim Conference on* **1**(I-346–I-347) (2001)
3. Motamedi, M., Johnigan, R., Bell, B., Pasricha, J., Calhoun, K.: Fluorescence guided optical coherence tomography for early detection of epithelial neoplasia. *LEOS 2000 13th Annual Meeting. IEEE* **1** (2000) 151
4. Gupta, P.C., Nandakumar, A.: Oral cancer scene in India. *Oral Diseases* (1) (1999) 1–2
5. Ledley, R.S., Buas, M., Golab, T.: Fundamentals of true color processing. In: 10th International Conference on Pattern Recognition, Atlantic City. Volume 1. (1990) 791–795
6. Pun, C.M., Lee, M.C.: Log-polar wavelet energy signatures for rotation and scale invariant texture classification. *IEEE Trans on Pattern Analysis and Machine Intelligence* **25**(5) (2003) 590–603
7. Cortes, C., Vapnik, V.N.: Support vector networks. *Machine Learning* **20** (1995) 273–297
8. Karkanis, S.A., Iakovidis, D.K., Maroulis, D.E., Karras, D.A., Tzivras, M.: Computer-aided tumor detection in endoscopic video using color wavelet features. *IEEE Trans on Technology in Biomedicine* **7**(3) (2003) 141–152
9. Ji, Q., Engel, J., Craine, E.: Texture analysis for classification of cervix lesions. *IEEE Trans. Med. Imag.* (2000) 1144–1149

Preliminary Clinical Results for the *In Vivo* Detection of Breast Cancer Using Interstitial Diffuse Optical Spectroscopy

Anthony Kim¹, Usha Kasthuri³, Brian C. Wilson²,
Alexander White¹, Anne L. Martel¹

¹ Sunnybrook Research Institute, Dept of Medical Biophysics, Toronto, Ontario, Canada

² Ontario Cancer Institute, Dept of Medical Biophysics, Toronto, Ontario, Canada

³ BioTelligent, Livermore, CA, U.S.A.

{anthony.kim@swri.ca}

Abstract. Timely and accurate diagnosis of breast cancer is vital to the prognosis for women with malignant tumors. Diffuse optical spectroscopy (DOS) has shown promise in *ex vivo* studies in distinguishing normal, benign and malignant breast tissue. In this work, we present preliminary results to diagnose breast cancer using DOS *in vivo*. A minimally-invasive fiber optic needle probe delivers light and collects optical spectra from the sampled tissue. Data sets from within healthy tissue and tumors have been collected for 19 patients with suspect lesions, with 10 patients exhibiting benign lesions and 9 patients with malignancies. Cytology and histology were used as the gold standard against the optical data. Principal components analysis on the clinical data is presented, demonstrating a clear shift in the spectra as the needle probe progresses from healthy to abnormal tissue.

Keywords: diffuse reflectance; diffuse optical spectroscopy; breast cancer; optical biopsy; elastic scattering spectroscopy

1 Introduction

Several types of optical spectroscopy have yielded promising results in the diagnosis of disease, with the focus on distinguishing cancerous or dysplastic areas from healthy tissue. Diffuse optical spectroscopy (DOS), a modality that measures multiply-scattered spectra from tissue, is particularly sensitive to the changes in biochemistry and structure of sub-cellular components with the onset of disease [2-8].

In screening for breast cancer, lesions are typically detected through mammography and palpation. Several researchers have explored the possibility of using various spectroscopic methods for diagnosing breast cancer once it is suspected [1-6]. There are several reasons that optical methods are potentially more desirable than excision or biopsy for breast cancer diagnosis. The real-time acquisition of optical spectra gives DOS the advantage of an immediate diagnosis, easing the psychological toll of delayed diagnosis. Fiber optics can be engineered into needles as small as those used in fine needle aspiration (FNA), allowing for a minimally invasive procedure. Unlike FNA, an 'optical biopsy' can interrogate larger volumes of tissue at

varying depths and locations in the suspect lesion, as opposed to a single tissue extraction point. Also, the optical biopsy procedure is less disfiguring than either a lumpectomy or core biopsy, since no tissue is being removed.

We present a diffuse optical spectroscopy device that delivers broadband white light into a suspect area of breast tissue through an optical biopsy needle and measures spectra diffusely reflected by the tissue (diffuse reflectance spectroscopy). A preliminary study using principal components analysis (PCA) on the separability of the spectra of normal/benign tissue and normal/malignant tissue within each patient shows promise that this method is sensitive to changes in tissue brought upon by the onset of breast cancer.

2 Background

Diffuse reflectance spectra in tissue are typically measured in the ultraviolet to near infrared range. A system consists of a source fiber that delivers light into the tissue and one or more collection fibers located at a distance from the source fiber. A spectrometer measures the incoming spectrum. The photons undergo scattering and absorption as they interact with the tissue, yielding valuable information on biochemical composition and scatterer content in the collected spectra.

This information can in turn be used to differentiate between normal and abnormal tissue states. Biological markers such as oxy-hemoglobin (HbO_2), deoxy-hemoglobin (Hb), and beta carotene (βC) are highly absorptive in the visible spectrum. Hemoglobin content and oxygenation is often associated with the growth of tumors, since their rapid proliferation requires enhanced angiogenesis. Scatterers such as organelles, nuclei, and macromolecules also significantly affect the reflectance spectra. One of the histological hallmarks of malignant tumors is the increase in nuclear size and irregularity, so the optical scattering power may be of diagnostic interest [4, 9].

Two approaches are generally used in extracting information from diffuse reflectance spectra for the diagnosis of disease, which can be termed the 'analytical approach' and the 'diagnostic approach' [9]. The analytical approach seeks to deconstruct the reflectance spectra into biologically and physically meaningful factors. These factors can then be used as bio-markers for the normal and diseased tissue states in order to form a basis for a diagnosis.

van Veen *et al* [3] uses this analytical approach to model the reflectance spectra with a modified diffusion theory equation for a diffuse reflectance optical biopsy needle. The percent oxygen saturation, beta carotene concentration, and total hemoglobin concentration were fitted to a model of the reflectance spectra for analyzing breast malignancies with an optical biopsy needle probe. Lorentz-Mie scattering was assumed in modeling the scatter power of the tissue, resulting in a simple mono-exponential form. From the 12 patient data set, normal tissue and malignant tumors were compared (all malignancies were either lobular or ductal carcinomas). There was a statistically significant difference in blood oxygenation, defined as $\text{StO}_2 = 100\% \times (\text{Hb} + \text{HbO}_2) / \text{Hb}_{\text{total}}$, with normal breast tissue having $\text{StO}_2 = 93 \pm 7\%$ and malignant tissue $65 \pm 28\%$. Beta carotene levels and scattering power, however, were not strong indicators.

The diagnostic approach does not try to explain the spectral characteristics in the reflectance data. Rather than attempt to find the source of biophysical causes behind the spectra exhibited by certain tissues, a diagnosis is based upon statistical metrics that separate the normal and disease tissue states. Nevertheless, this approach has merit, as solving the analytical approach may be difficult due to the complexity of the probe and the heterogeneity of the tissue.

Palmer *et al* [5] examined diffuse reflectance data from excised breast tissue using the diagnostic approach. They used a cylindrical surface probe, with a ring of collection fibers surrounding the source fiber. Of the 56 samples from 32 patients, most consisted of a normal-tumor pair from each patient. Tissue samples were broadly categorized as benign, malignant, and normal. Principal components analysis (PCA) was then applied as a data reduction technique, and the scores were used as metrics to train a classifier called a support vector machine (SVM) to separate the data into malignant and non-malignant tissues. This resulted in an optimized classifier that could diagnose malignancies with a sensitivity and specificity of 70% and 92%, respectively.

For the present work, we analyzed the diffuse reflectance data using the diagnostic approach, performing PCA to observe how well the optical data can separate normal tissue and tumors within a single patient. Rationale for taking a more analytical approach will be discussed at the end.

3 Methods

The clinical instrumentation used in this study is the BioTelligent Optical Diagnostic System(ODS)TM. Fig 1 shows a schematic of the fiber optic needle probe. A broadband white light source illuminates the tissue through fiber optics. Collection fibers, located on the needle tip, deliver the reflected light to a spectrometer and data acquisition system. The reflectance spectra are collected at 100Hz as the surgeon progresses the needle through the breast tissue. The measurements are in the visible light range between 400nm and 700nm.

A total of 19 patients, 10 with benign lesions and 9 with malignancies, underwent the ODS optical biopsy during the same visit as a FNA procedure. Lesions for this study were typically large, between 1-3cm in diameter, so the surgeon was able to record the time when the optical probe tip contacted the lesion. If FNA cytology came back suspect, the lesion was excised and histologically confirmed.

4 Results and Discussion

The data reported here were taken from a small set of 19 patients in an ongoing study. The goal is to eventually achieve sensitivity and specificity rates of over 90%. In the present work, the objective is to explore the viability of this goal by testing 1) if the normal and abnormal regions of the breast within each patient are indeed spectrally different and 2) for any obvious patterns between malignant tumors, benign lesions, and normal tissue across the inter-patient data set.

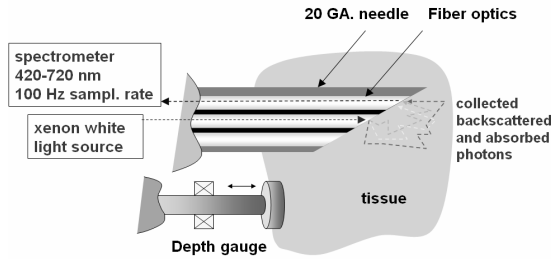


Fig 1. Schematic of the diffuse reflectance optical biopsy probe

4.1 Analysis of Individual Patient Data Sets

The optical spectra of an infiltrating ductal carcinoma and a benign fibroadenoma are shown in Fig. 2a, from two patients. The spectra are averaged over 1cm within the abnormal tissue (tumor or fibroadenoma). The spectra are representative of some but not all the data.

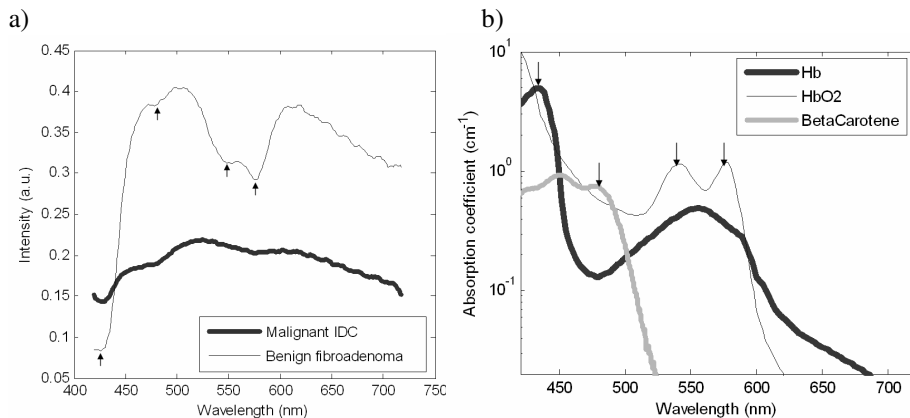


Fig. 2: a) Reflectance spectra for a malignant infiltrating ductal carcinoma and a benign fibroadenoma. The characteristic absorbance spectral peaks of beta-carotene, deoxy- and oxy-hemoglobin are shown by the small arrows on the benign spectrum and the corresponding absorbance graphs shown in b). Since increased absorbance means decreased reflectance and vice-versa, peaks and valleys in the absorbance curves correspond to valleys and peaks in the reflectance curves.

For comparison, the absorbance graphs of oxy-hemoglobin, deoxy-hemoglobin, and beta carotene are shown in Fig. 2b¹. The breast tissue reflectance spectra resemble a Mie-like negative slope pattern overlaid by the spectral peaks and valleys of the various absorbers. The benign lesion displays a strong 'double-hump' oxy-hemoglobin signature at 541 and 576nm. The beta carotene valley at 477nm is evident

¹ Molar concentrations for Hb, HbO₂, and β C of 3.90 μ M, 9.3 μ M, and 29.0 μ M were used to calculate the absorbance graph scaling. Hemoglobin concentrations were measured by Shah *et al* [8]; beta carotene concentrations were measured by van Veen *et al* [3].

as well. The spectrum for this benign fibroadenoma closely resembles the diffuse reflectance spectrum for normal glandular tissue published by van Veen *et al* [3].

The malignant tumor has a significantly lower amplitude, albeit with smaller hemoglobin indicators, implying a reduced amount of scattering. In the analytical methodology of Tromberg *et al* [7], the relative scattering coefficient (relative to normal healthy tissue) for invasive cancers was found to be significantly lower than that of fibroadenomas; the result in Fig. 2a is consistent with this observation.

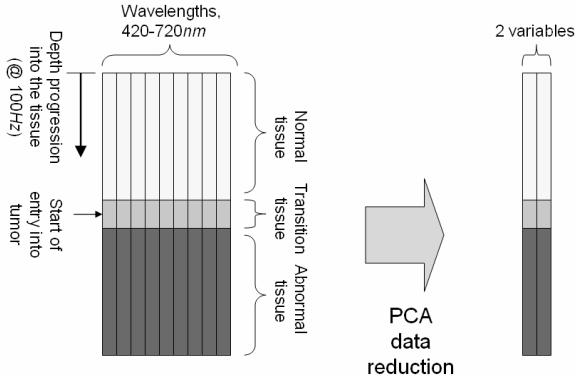


Fig. 3: Schematic of the reflectance data compressed by PCA to two variables

In order to characterize how the data shows the transitions from normal to abnormal tissue, principal components analysis for individual patients was employed to reduce the data to a small number of orthogonal variables. Let the data be contained in matrix \mathbf{D} ($n \times p$), with n data points corresponding to time indices taken at 100Hz, and p wavelength channels. Taking the covariance of \mathbf{D} to produce \mathbf{A} ($p \times p$), we solve for the eigenvalue problem:

$$\mathbf{A}\Phi = \Phi\Lambda, \quad \Phi^T\Phi = \mathbf{I} \quad (1)$$

$$\Lambda = \text{diag}(\delta_1, \delta_2, \dots, \delta_p), \quad \delta_1 \geq \delta_2 \geq \dots \geq \delta_p$$

where Φ ($p \times p$) has as its columns p orthonormal eigenvectors $\phi_1, \phi_2, \dots, \phi_p$ (which happens to be equivalent to the principal components), and Λ is the eigenvalue matrix.

PCA characterizes the largest amount of variance in the data along the first principal component (PC) vector, and the second largest variance along an orthogonal second PC, until all the variance can be explained with the same number of PCs as there are variables. For the breast data, the first two principal component vectors ϕ_1 and ϕ_2 accommodate typically >95% of the data variance. We take the estimate of the original matrix \mathbf{D} by projecting it on the first two principal components:

$$\hat{\mathbf{D}} = \mathbf{D} \times [\phi_1 \ \phi_2] \quad (2)$$

where $\hat{\mathbf{D}}$ ($n \times 2$) contains the compressed spectral data. The original data can now be plotted in two dimensions.

Fig. 4 shows PCA-compressed optical spectra for normal tissue data (prior to lesion entry) and data within the suspect tissue. The transition tissue is defined as the

tissue measured 1sec before and 1sec after the surgeon reported that the needle has reached the target lesion. The data plotted against the first two principal components show a separation between normal tissue and the benign and malignant areas.

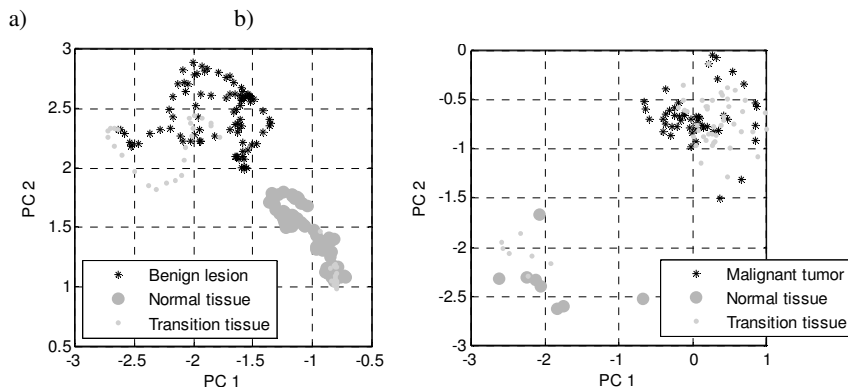


Fig. 4. Individual patient measurements showing data points plotted against the first two PCs as the needle progresses into the tissue for a) normal and benign tissue and b) normal and malignant tissue. Transition tissue data points are shown to demonstrate how the data behaves as the needle transitions from normal to abnormal tissue.

Not all data sets exhibit such clear separations between tissue states. Fig. 5 shows another two patient data sets analyzed in the same manner. Although the clusters for each type of tissue are distinct, the two clusters overlap. Blind separation algorithms such as SVMs may have difficulty in finding a boundary between such tissue states. This may explain why diagnostic approaches such as those taken by Palmer *et al* [5] result in low sensitivity rates of approximately 70%.

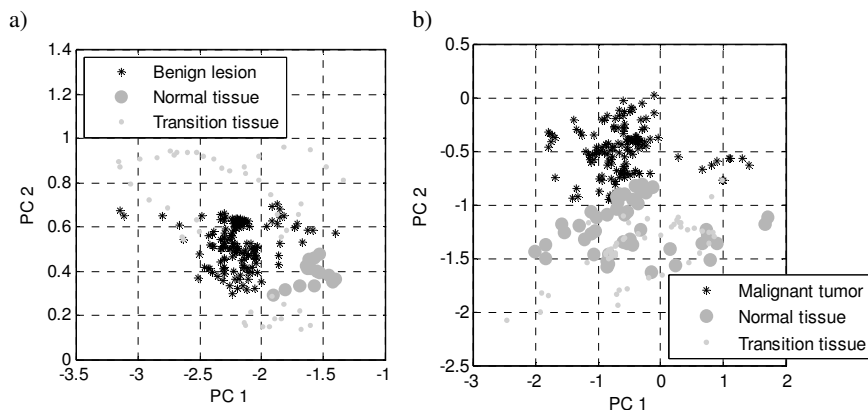


Fig. 5. Similar as the previous two figures, but with examples of normal and abnormal tissue data clusters touching. a) Normal transitioning to benign tissue and b) normal transitioning to malignant tissue plotted against the first two principal components.

4.2 Analysis Across All Patient Data Sets

Fig. 6 shows the averaged spectra among the 19 patients for normal, benign, and malignant tissues. There is significant variability in the inter-patient data set. This may be a result of the variation of hemoglobin in the tissue, due to the mechanical deformation of the tissue as the needle progresses, squeezing blood in and out of the vasculature. Engineering improvements such as a smaller needle and mechanisms for better needle control can partially solve this possible problem.

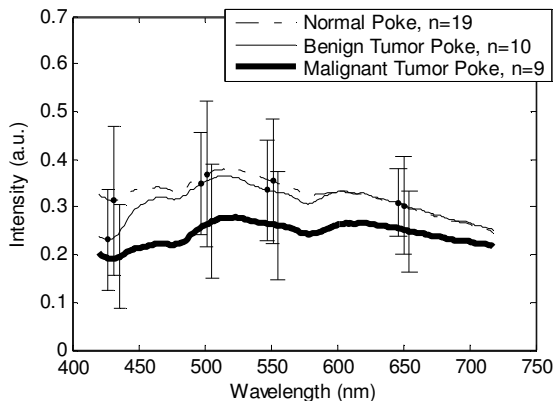


Fig. 6. Averaged spectra from a DOS collection fiber for 19 normal tissue, 10 benign, and 9 malignant measurements. The error bars represent \pm one standard deviation.

A prevailing pattern in Fig. 6 is the significantly lower amplitude of the average malignant tumor spectrum. As mentioned before, this may be indicative of lower levels of optical scattering within the tumor. The large standard deviation of the data, however, makes this observation not diagnostically significant.

The PCA data cluster analysis shows a clear difference between normal and abnormal tissues within each patient. The challenge is a large spectral variance in the inter-patient data set, hindering the development of a diagnostic algorithm. We hypothesize that significant biological markers that are diagnostic of normal and malignant tissues are being detected; however, we also hypothesize that there are also large biological factors that are non-diagnostic of disease interfering with the signal. We believe that separating these “bio-markers” with an analytical approach will enable us to keep the factors that are diagnostically significant and attenuate those that are not, establishing a pattern in the inter-patient data set.

5 Future Work

Our current direction towards reducing the inter-patient variability is to empirically and theoretically model the optical probe to extract the absorption, scattering, and anisotropy coefficients from the reflectance spectra. By separating bio-markers from the overall reflectance signal, the diagnostically important markers can be used and the insignificant markers discarded. There are two approaches being followed: an empirical model (experimental phantom work) and theoretical model (Monte Carlo

approach). Although it is possible to characterize how reflectance is related to the absorbance and scattering coefficients, as demonstrated by Bargo *et al* [6], other parameters such as average photon path length and the interrogation volume can only be reliably extracted using a theoretical approach such as Monte Carlo simulation.

6 Conclusions

Principal component analysis data reduction shows that the spectra from normal, malignant, and benign tissues are distinct from each other within a single patient. On the other hand, there is significant inter-patient variability due to the presence of non-diagnostic biological markers. Further work in this area includes modeling the optical probe to separate the absorption and scattering coefficients, and then the individual biological markers, in order to reduce the inter-patient variation. The data set will also be significantly expanded to include over one hundred patients.

7 References

1. Peters, V.G., Wyman, D.R., Patterson, M.S., Frank, G.L.: Optical properties of normal and diseased human breast tissues in the visible and near infrared. *Phys Med Biol.* (1990) 35(9): 1317-34
2. Bigio, I.J., Bown, S.G., Briggs, G., Kelley, C., Lakhani, S., Pickard, D., Ripley, P.M., Rose, I.G., Saunders, C.: Diagnosis of breast cancer using elastic-scattering spectroscopy: preliminary clinical results. *J Biomed Opt.* (2000) 5(2): 221-8
3. van Veen, R.L., Amelink, A., Menke-Pluymers, M., van der Pol, C., Sterenberg, H.J.: Optical biopsy of breast tissue using differential path-length spectroscopy. *Phys Med Biol.* (2005) 50(11): 2573-81
4. Perelman, L.T., Backman, V., Wallace, M., Zonios, G., Manoharan, R., Nusrat, A., Shields, S., Seiler, M., Lima, C., Hamano, T., Itzkan, I., van Dam, J., Crawford, J. M., Feld, M. S.: Observation of Periodic Fine Structure in Reflectance from Biological Tissue: A New Technique for Measuring Nuclear Size Distribution. *Phys Rev Letters.* (1990) 80(3): 627-630
5. Palmer, G.M., Zhu, C., Breslin, T.M., Xu, F., Gilchrist, K.W., Ramanujam, N.: Comparison of multiexcitation fluorescence and diffuse reflectance spectroscopy for the diagnosis of breast cancer. *IEEE Trans Biomed Eng.* (2003) 50(11):1233-42
6. Bargo, P.R., Prah, S.A., Goodell, T.T., Slevin, R.A., Koval, G., Blair, G., Jacques, S.L.: In vivo determination of optical properties of normal and tumor tissue with white light reflectance and an empirical light transport model during endoscopy. *J Biomed Opt.* (2005) 10(3): 034018
7. Tromberg, B.J., Shah, N., Lanning, R., Cerussi, A., Espinoza, J., Pham, T., Svaasand, L., Butler, J.: Non-invasive in vivo characterization of breast tumors using photon migration spectroscopy. *Neoplasia.* (2000) 2(1-2):26-40
8. Shah, N., Cerussi, A., Eker, C., Espinoza, J., Butler, J., Fishkin, J., Hornung, R., Tromberg, B.: Noninvasive functional optical spectroscopy of human breast tissue. *Proc Natl Acad Sci USA.* (2001) 98(8):4420-5
9. Perelman, L.T., Backman, V.: Light scattering spectroscopy of epithelial tissues: principles and applications. *Handbook of optical biomedical diagnostics* [ed. Tuchin, V.] SPIE, Bellingham WA (2002) 675-724

Optical Coherence Tomography in Dermatology

Jakob Thomsen¹, Mette Mogensen², Hanan Morsy², Thomas Martini Jørgensen¹,
Lars Thrane¹, Peter E. Andersen¹, Gregor B.E. Jemec²

1. Optics and Plasma Research Department, Risoe National Laboratory,
Frederiksborgvej 399, P.O. Box 49, DK-4000 Roskilde, Denmark

2. Department of Dermatology, Roskilde Hospital, University of
Copenhagen, Koegevej 7-13, DK-4000 Roskilde, Denmark

Abstract. Optical coherence tomography (OCT) is a non-invasive imaging method for obtaining potential high resolution (2-20 μm) images of outer layer tissue (2-3 mm penetration). Since the technique is rather new the applications are still investigated. Because of the high resolution images provided by OCT, promising results is expected within dermatology. We summarize the results from recent studies in dermatology using OCT. This includes skin cancer diagnostics, imaging of tattoos, tropical diseases and for measurement of nail thickness. Furthermore techniques for reduction of speckle noise in OCT images is discussed.

Introduction

OCT is a novel, non-invasive optical imaging technology¹. It can provide cross-sectional tomographic images of tissue pathology *in situ* and in real time, without the need for excision and processing of specimens, as in conventional histopathology. OCT use harmless, infrared light to create high-resolution images of tissue. In contrast to conventional microscopy, OCT provides cross-sectional images of structures below the tissue surface in analogy to histopathology. Hence OCT can function as an “optical biopsy” providing images of tissue structure on the micron scale. For example, OCT could be used where standard excision biopsy is hazardous or impossible, and OCT could reduce sampling errors associated with excision biopsy.

Cross-sectional OCT images are generated when an optical beam is scanned across the tissue and echo time delay and intensity of backscattered light is measured. Because the velocity of light is extremely high optical echoes cannot be measured directly. Instead OCT is based on a technique called low-coherence interferometry. The principle is, measuring light reflected or backscattered from inside a specimen by correlating with light that has travelled a known reference path. OCT is analogue to B-mode ultrasound pulse-echo imaging with an optical rather than acoustical reflectivity being measured.

There are several ways to enhance information input from OCT images. The most important are OCT Doppler function and polarization sensitivity (PS), both complementary to conventional images. Another up-coming system is molecular contrast OCT. Recent development includes fast Fourier Domain OCT systems allowing for almost realtime 3D recordings and for systems with fewer mechanically moving elements.

Here we present different applications of OCT in dermatology and evaluate the potential.

OCT in skin cancer diagnosis

Skin cancer is the most prevalent cancer in the Western World. Unfortunately it cannot always be diagnosed clinically – that is diagnosis by the naked eye only. The earlier a skin cancer is diagnosed, the better the prognosis. For that reason an extensive technological development in optical imaging technologies have proved beneficial in dermatology. OCT has a penetration of 1.5-2.0 mm in skin making it very useful for imaging of the epidermis and upper dermis, which is also the upper limit of most skin cancers.

The reference standard for skin cancer diagnosis is a skin biopsy. A biopsy may be a time-consuming, expensive and sometimes mutilating and painful experience to the patient, especially because only around 3% of presumed benign lesions are actually malignant². Furthermore whereas treatment has hitherto been almost synonymous with surgery, new non-invasive treatment strategies call for non-invasive diagnostics.

Together with the Dept of Dermatology, Roskilde Hospital, Copenhagen University we are investigating the diagnostic potential of OCT in skin cancer. Until now we have included more than 50 patients with 85 skin cancer lesions. Skin cancer are grouped in two main types: Non-melanoma skin cancer (NMSC) and cutaneous malignant melanoma (MM). NMSC have been investigated with OCT with quite promising results. The pilot studies have suggested that OCT can be used clinically in diagnosing NMSC⁴⁻¹⁰. In a study of 20 BCC lesions, there was an excellent match of histological features seen on light microscopy with OCT images of superficial, nodular, micronodular and infiltrative BCCs⁹. The actual predictive value of OCT in BCC patients could however not be calculated from this study. In three patients with superficial BCC and three patients with MM, OCT images were compared with histology. The size, allocation and form of BCC nests seemed to be similar to those in histological images¹¹.

By comparing OCT images of normal tissue with images of non-melanoma skin cancer like basal cell carcinomas (BCC) the preliminary studies reveals that normal skin exhibits a layered structure not present in either of the imaged lesions (see figure 1). Furthermore, tissue with BCC seems to be clearly less reflective than normal tissue. Polarisation sensitive-OCT may have additional advantage as BCC differ in content of birefringent collagens from normal skin. In figure 2 we show polarisation-sensitive OCT images from a BCC lesion are shown. It is evident, that PS-OCT of BCC lesions differ from normal skin. Another important issue is whether OCT can be helpful in distinguishing different types of skin cancer. This is the topic of ongoing work.

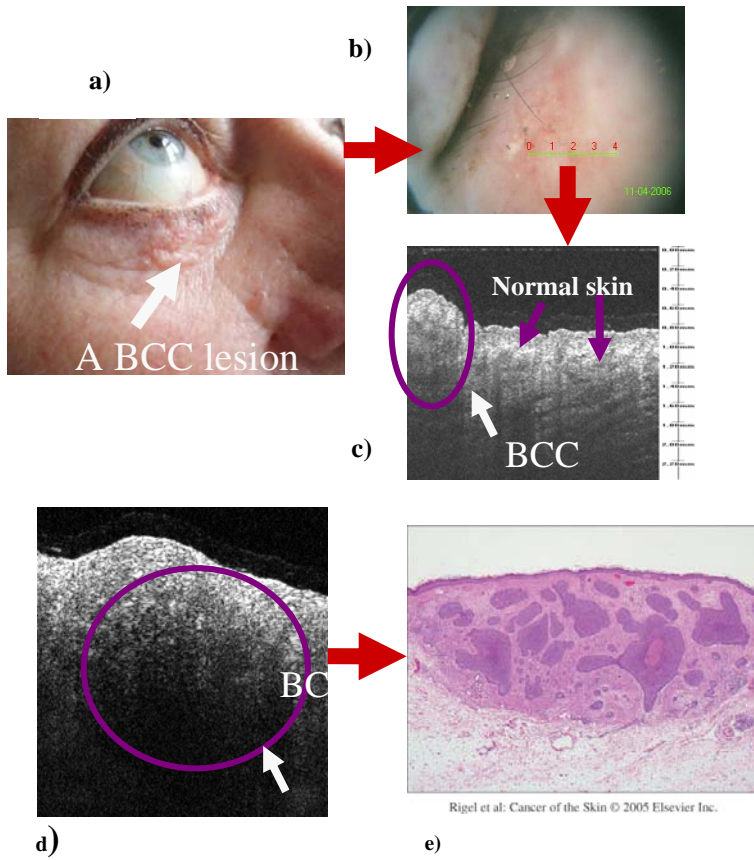


Figure 1: a) picture of a BCC lesion b) photo from the probe with the green line indicating position of the OCT scan c) corresponding OCT image d) another OCT-image from the same BCC lesion e) histopathology from a similar BCC lesion.

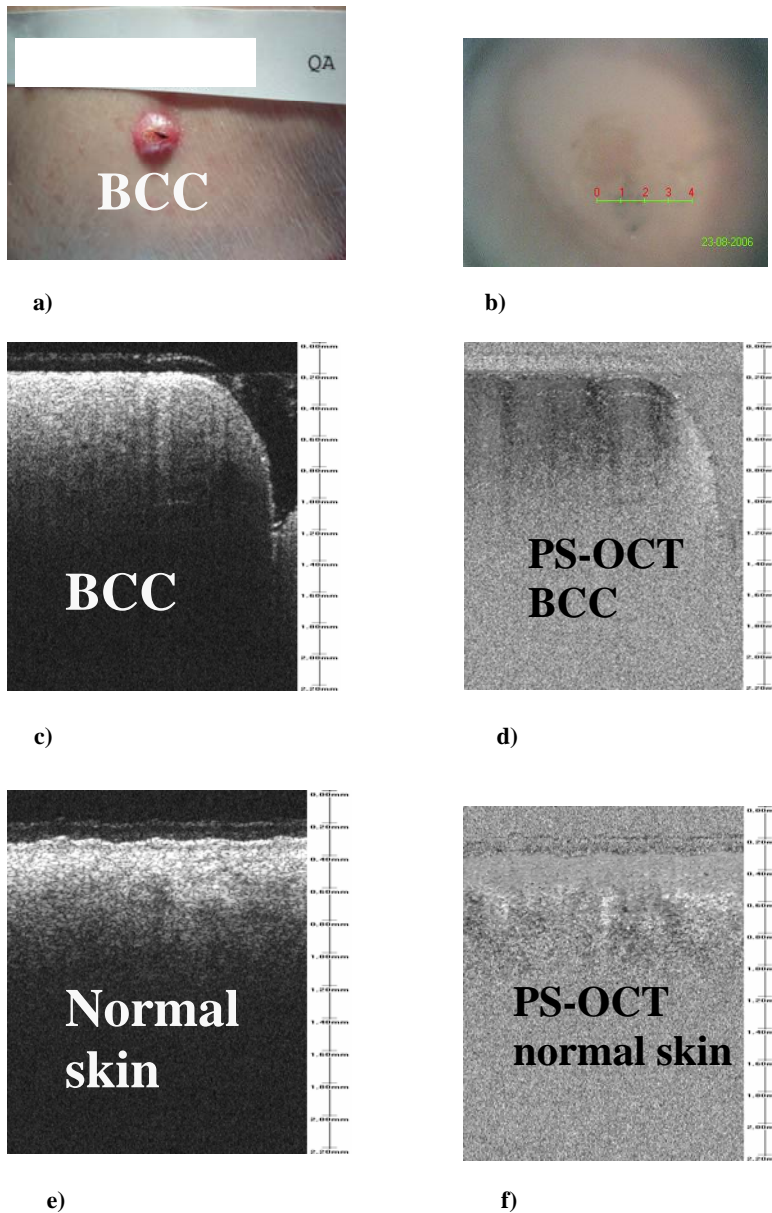


Figure 2: a) Photo of the BCC lesion b) photo from the probe with the green line indicating position of the OCT scan c) OCT image of the BCC lesion d) polarization-sensitive OCT-image from the BCC lesion e) normal adjacent skin f) polarization-sensitive OCT image from normal skin.

OCT in tattoos

Tattooing has become very common among young adults. The procedure of tattooing involves inserting pigment deep in the dermis through epidermis; the pigment distribution has been described in a previous pivotal study using electron microscopy. It was shown that tattooed skin pass through phases of inflammatory reaction and necrosis followed by the presence of ink particles in dermal fibroblasts¹⁴. The scanned tattoos showed the presence of dark structure or shadow usually below the level of dermo-epidermal junction (see fig. 3). This dark structure was organized mainly in the tattooed area, and towards the lower dermis. The epidermis was not affected by that dark structure. There was shadowing (empty depressions in between the dark structure) in the scanned tattooed skin that not appeared in clinical examination. At the same time, the scanned skin without tattoo appeared to be free of this dark structure, the demarcation between the tattooed skin and normal surrounding skin was generally clear.

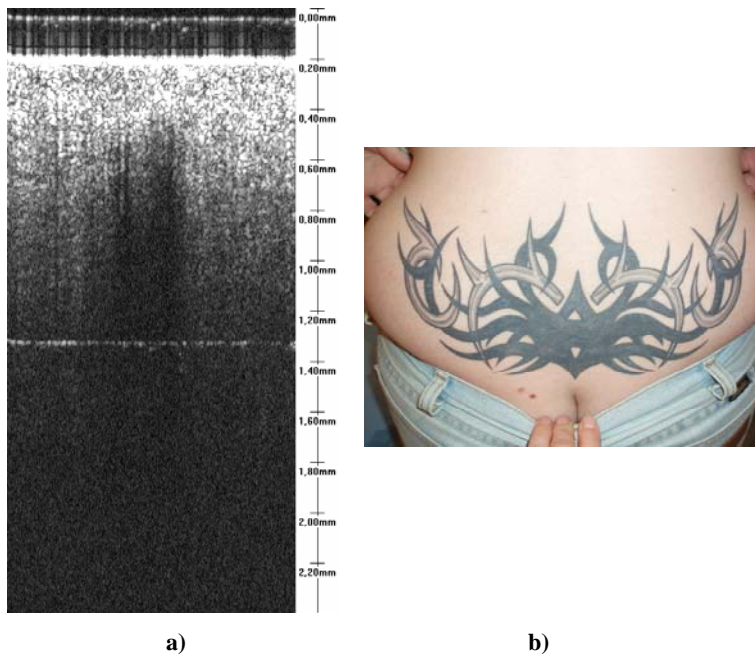


Figure 3: a) OCT image across a tattoo. The pigment absorbing the light is seen at the center, in the dermal layer of the skin b) picture of the tattoo.

OCT in tropical diseases

One of the most prevalent diseases in travellers returned from the Tropics is the Creeping Eruption also referred to as cutaneous larva migrans. Cutaneous larva migrans (CLM) is a parasitic skin eruption caused by migration of larvae of various nematodes, most commonly dog and cat hook worms (*Ancylostoma caninum* and *A. braziliense*). The infection occurs after contact with contaminated soil or animal products². The disease with its characteristic eruption arises when a hookworm erroneously enters the skin. The larva gets trapped under the skin, and digs a tunnel, which can clearly be visualized, see the OCT-images in figure 4. The width of the tunnel is $\sim 300 \mu\text{m}$.

Clinically CLM is characterized by the presence of allergic reaction as a result of the products of the larva, which is produced through its penetration into epidermis and less often the upper dermis³. The symptoms and signs of the disease are a creeping, serpiginous eruption and sometimes a severe itch from the lesion. OCT imaging was done in the larva tracks, and revealed the boundaries of the track which is located just below the dermo-epidermal junction, and the shadowing of this track is directing downwards through the dermis. The patient was successfully treated with oral ivermectin.

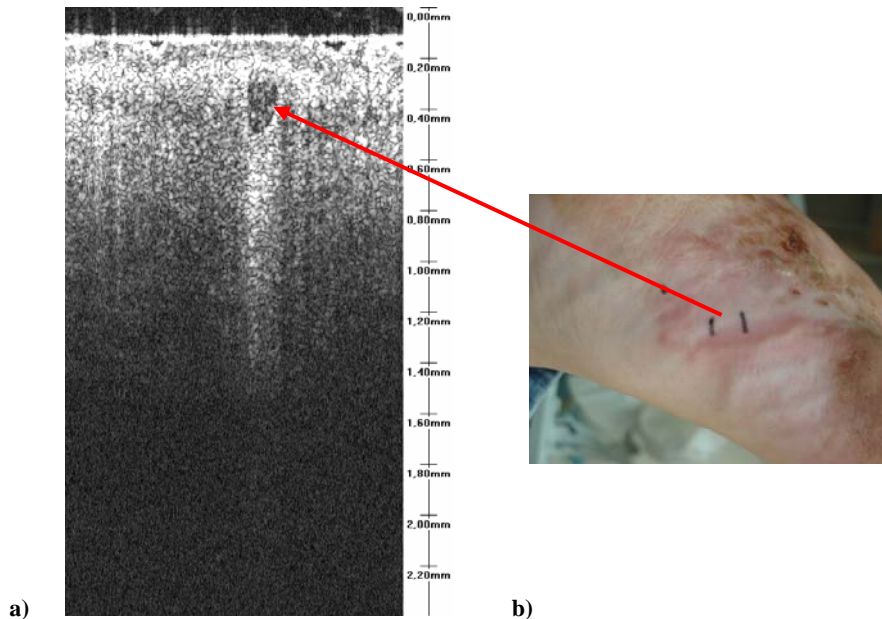


Figure 4: a) OCT image of a cross-section of the tunnel that has been digged into the skin by a larva b) picture of the patients foot with the tunnel digged by the larva.

OCT for measuring nail thickness

Currently nail diseases are diagnosed mainly based on clinical examination although biopsies and scrapings can also provide clinical significant information. Medical imaging techniques as ultrasonography (US), magnetic resonance imaging (MRI), NIR-spectroscopy and optical coherence tomography have been applied to investigate nail structure and pathology, but are, apart from US, not used routinely in the dermatology clinic. It is well established that high-frequency ultrasound (HFUS) can be used for measuring nail thickness¹⁵⁻¹⁶. Undoubtedly non-invasive imaging technologies have diagnostic potentials in nail pathology. The aim of this pilot study was to investigate the potential of optical coherence tomography for nail thickness measurement by comparing it to nail thickness measured by 20 MHz ultrasonography and caliper. Ten healthy volunteers with no clinical signs or history of nail disease were recruited from the OCT group and its collaborators. The volunteers gave written, informed consent. The study was done in accordance to Helsinki declaration. Volunteers were all Caucasians, 3 men and 7 women, aged 26-51 (mean 35.4). All 10 fingernails from the volunteers were examined by HFUS, OCT and nail thickness was measured by a caliper in the same session. We have found OCT imaging of the nail very easy to apply. The use of a non-invasive method for the study of the human nail offers several advantages over existing research methodology: allows for longitudinal studies, allows for quantification of subsurface structures, and allows for distinction between birefringent and non-birefringent tissue. Skin cancer e.g. has been demonstrated to have less birefringence than normal tissue¹³. Further studies on larger populations are needed to validate our OCT imaging and nail thickness measurements.

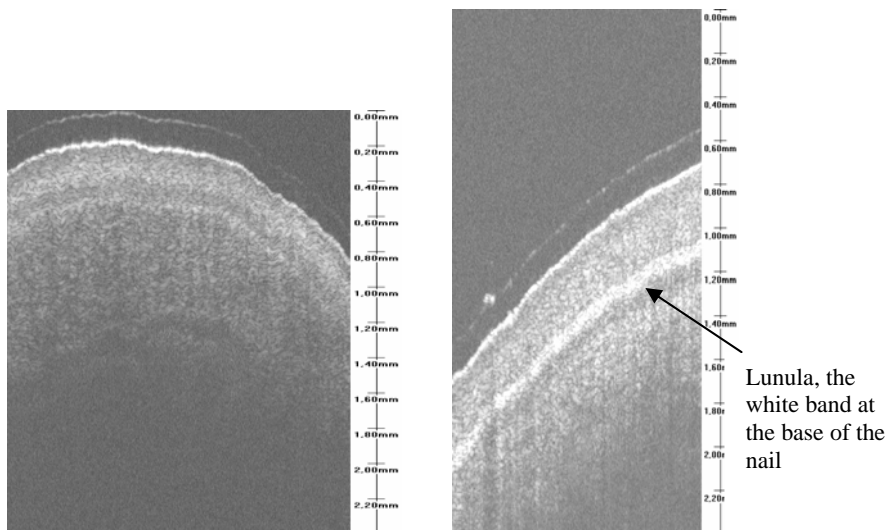


Figure 5: Typical OCT images of the nail structure.

Enhancing OCT images by speckle reduction

As the OCT technique is based on a coherent imaging principle the signal is degraded by speckle noise caused by interference of waves with random phases. In order to suppress this noise one has to generate uncorrelated speckle patterns, which in turn must be summed on an intensity basis. Time, space, frequency or polarisation diversities are ways of obtaining uncorrelated speckles, but it can often be difficult to obtain a reasonable number of uncorrelated patterns¹⁷⁻¹⁸. Recently promising results has been obtained using an angular compounding technique where scattered waves are separately detected dependent on the backscattering angle¹⁹. Postprocessing the images using denoising techniques such as wavelet filtering has also been proposed, but will often suffer from the risk of introducing artifacts in the images.

Here we illustrate how speckle noise can be suppressed using a kind of spatial compounding. The OCT scan of a fingertip in figure 6a is a single image, whereas the image in figure 6b is obtained by combining 20 recordings, where the sample has been vertically moved relative to the probe. It is clearly seen how the speckles are reduced thereby increasing the signal-to-noise ratio. Such enhancing of the signal is expected to be of great importance in dermatology as we are dealing with highly scattering tissue.

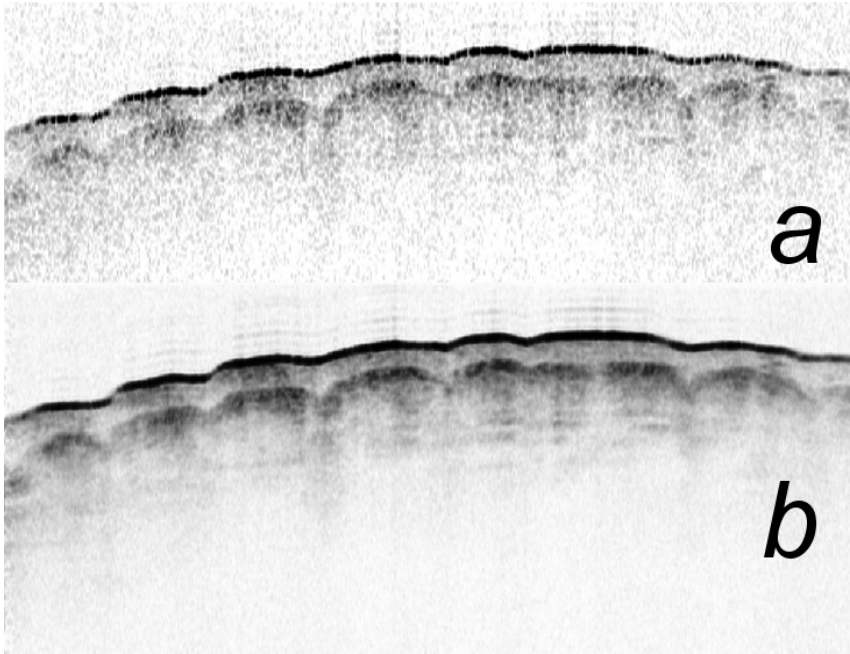


Figure 6: Inverse gray-scale image of OCT B-scan recorded at a fingertip. Single recording (a) versus average obtained by using spatial compounding (b).

Acknowledgement

This work was supported by the Danish Research Agency (BIOPHOT framework, grant no. 26-02-0020)

References

1. B. E. Bouma, G. J. Tearney, *Handbook of Optical Coherence Tomography*, 2002.
2. Tycho A, Andersen P, Thrane L *et al.* *Optical Coherence Tomography in Dermatology. Chap.31 Non-invasive Methods and the Skin*, 2nd edn. Boca Raton: CRC Press, Taylor and Francis Group, 2006.
3. Hallock GG, Lutz DA. Prospective study of the accuracy of the surgeon's diagnosis in 2000 excised skin tumors. *Plast.Reconstr.Surg.* 1998; 101: 1255-61.
4. Gambichler T, Moussa G, Sand M *et al.* Applications of optical coherence tomography in dermatology. *J.Dermatol.Sci.* 2005; 40: 85-94.
5. Pierce MC, Strasswimmer J, Park BH *et al.* Advances in optical coherence tomography imaging for dermatology. *J.Invest Dermatol.* 2004; 123: 458-63.
6. Welzel J, Lankenau E, Birngruber R *et al.* Optical coherence tomography of the human skin. *J.Am.Acad.Dermatol.* 1997; 37: 958-63.
7. Welzel J. Optical coherence tomography in dermatology: a review. *Skin Res.Technol.* 2001; 7: 1-9.
8. Steiner R, Kunzi RK, Scharffetter KK. Optical Coherence Tomography: Clinical Applications in Dermatology. *Medical Laser Application.* 2003; 18(3): 249-259: -259.
9. Olmedo JM, Warschaw KE, Schmitt JM *et al.* Optical coherence tomography for the characterization of basal cell carcinoma in vivo: a pilot study. *J.Am.Acad.Dermatol.* 2006; 55: 408-12.
10. Gambichler T, Boms S, Stucker M *et al.* Comparison of histometric data obtained by optical coherence tomography and routine histology. *J.Biomed.Opt.* 2005; 10: 44008.
11. Bechara FG, Gambichler T, Stucker M *et al.* Histomorphologic correlation with routine histology and optical coherence tomography. *Skin Res.Technol.* 2004; 10: 169-73.
12. Strasswimmer J, Pierce MC, Park B *et al.* Characterization of basal cell carcinoma by multifunctional optical coherence tomography. *J.Invest.Dermatol.* 2003; 121: 0156.
13. Strasswimmer J, Pierce MC, Park BH *et al.* Polarization-sensitive optical coherence tomography of invasive basal cell carcinoma. *J.Biomed.Opt.* 2004; 9: 292-8.

14. Lea PJ, Pawlowski A. Human tattoo. Electron microscopic assessment of epidermis, epidermal-dermal junction, and dermis. *Int.J.Dermatol.* 1987; 26: 453-8.
15. Finlay AY, Western B, Edwards C. Ultrasound velocity in human fingernail and effects of hydration: validation of in vivo nail thickness measurement techniques. *Br.J.Dermatol.* 1990; 123: 365-73.
16. Jemec GB, Serup J. Ultrasound structure of the human nail plate. *Arch.Dermatol.* 1989; 125: 643-6.
17. J.W. Goodman, *Laser Speckle and Related Phenomena*, ed. J.C. Dainty (Berlin:Springer) pp. 9-75 (1984)
18. J.M. Schmitt et al., "Speckle in Optical Coherence Tomography", *J. Biomed. Opt.*, vol 4, pp. 95-105
19. A.E. Desjardins et al. , "Speckle reduction in OCT using massively-parallel detection and frequency-domain ranging," *Optics Express*, Vol. 14, pp 4736-4745, (2006)

The Intrinsic Dimension of Multispectral Images

Cicero Mota¹, Ingo Stuke², and Erhardt Barth³

¹ Departamento de Matematica, Universidade Federal do Amazonas, Manaus, Brazil *

² Institute for Signal Processing, University of Lübeck, Germany

³ Institute for Neuro- and Bioinformatics, University of Lübeck, Germany **

mota@ufam.edu.br, barth@inb.uni-luebeck.de.

Abstract. In this theoretical paper we address the question of how to encode the local signal variation of multidimensional, multispectral signals. To this end, we first extend the concept of intrinsic dimension to the case of multispectral images in a way which is not depending upon the chosen colour space. We then show how additive, multiplicative, and occluded superpositions of oriented layers can be detected and estimated in multispectral images. We expect our results to be useful in applications that involve the processing of multispectral images, e.g. for feature extraction, compression, and denoising. Moreover, our methods show how the detection and estimation of features like orientations, corners, crossing etc. can be improved by the use of multispectral images.

1 Introduction

Let a gray-scale image be modelled by a function $f : \mathbb{R}^2 \rightarrow \mathbb{R}$. Given an (open) region Ω , for all $(x, y) \in \Omega$, either (a) $f(x, y) = \text{constant}$; or (b) $f(x, y) = g(ax + by)$, for some g, a, b ; or (c) f varies along all directions. The image f is said to locally have intrinsic dimension 0, 1 or 2, respectively (0D, 1D, 2D for short) [1]. The intrinsic dimension is relevant to image coding due to the predominance of 0D and 1D regions in natural images [2] and the fact that images are fully determined by the 2D regions, i.e. the whole image information is contained in the 2D regions [3]. The concept can be expressed in a more mathematical form as follows [4]. For a given region Ω , we choose a linear subspace $E \subset \mathbb{R}^2$, of highest dimension, such that

$$f(\mathbf{x} + \mathbf{v}) = f(\mathbf{x}) \quad \text{for all } \mathbf{x}, \mathbf{v} \text{ such that } \mathbf{x}, \mathbf{x} + \mathbf{v} \in \Omega, \mathbf{v} \in E. \quad (1)$$

The intrinsic dimension of f is therefore $2 - \dim(E)$ for images (and $n - \dim(E)$ for n -dimensional signals). The intrinsic dimension can be estimated with differential methods, and we will review three such methods below. More general approaches are based on the compensation principle [1] and the Volterra-Wiener theory of nonlinear systems [5].

* CM thanks CNPq/FAPEAM for financial support.

** This work has been supported by the *Deutsche Forschungsgemeinschaft* under Ba 1176/9-3. We thank Martin Haker for comments on the manuscript.

Structure Tensor. This is a straightforward method based on the equivalence in Ω of Eq. (1) and the constraint

$$\frac{\partial f}{\partial \mathbf{v}} = 0 \quad \text{for all } \mathbf{v} \in E. \quad (2)$$

The subspace E can be estimated as the subspace spanned by the set of unity vectors that minimise the energy functional

$$\mathcal{E}(\mathbf{v}) = \int_{\Omega} \left| \frac{\partial f}{\partial \mathbf{v}} \right|^2 d\Omega = \mathbf{v}^T \mathbf{J} \mathbf{v}, \quad (3)$$

where \mathbf{J} is given by

$$\mathbf{J} = \int_{\Omega} \nabla f \otimes \nabla f d\Omega = \int_{\Omega} \begin{bmatrix} f_x^2 & f_x f_y \\ f_x f_y & f_y^2 \end{bmatrix} d\Omega. \quad (4)$$

In the above equation, the symbol \otimes denotes the tensor product, and f_x, f_y are short notations for $\partial f / \partial x, \partial f / \partial y$. Therefore, E is the eigenspace associated with the smallest eigenvalues of \mathbf{J} , and the intrinsic dimension of f corresponds to the rank of \mathbf{J} and may be obtained from the eigenvalue analysis of \mathbf{J} or, equivalently, from its symmetric invariants [6].

The Hessian. Since Eq. (1) is assumed to be valid in a neighbourhood, it follows that, in Ω ,

$$\frac{\partial^2 f}{\partial \mathbf{w} \partial \mathbf{v}} = \mathbf{0} \quad \text{for all } \mathbf{v} \in E \text{ and } \mathbf{w} \in \mathbb{R}^2 \quad (5)$$

or, equivalently,

$$\mathbf{H} \mathbf{v} = \mathbf{0} \quad \text{for all } \mathbf{v} \in E, \quad [7] \quad (6)$$

where \mathbf{H} is the Hessian of f , i.e.,

$$\mathbf{H} = \begin{bmatrix} f_{xx} & f_{xy} \\ f_{xy} & f_{yy} \end{bmatrix}. \quad (7)$$

Hence, as for the structure tensor method, both the subspace E and the intrinsic dimension can be estimated from the eigenvalue analysis of the Hessian of f [1].

The Energy Tensor. The structure-tensor and Hessian methods have similar drawbacks. The first fails at singular points, e.g., extreme points, while the second fails at inflection points of the image. Equations (2) and (5) may be combined into a phase invariant tensor, the so called *energy tensor* [8]:

$$\mathbf{B} = \nabla f \otimes \nabla f - f \mathbf{H}. \quad (8)$$

Note that the energy tensor is a combination of the structure tensor and the Hessian.

The purpose of this paper is twofold: first, we show how the above methods for the estimation of the intrinsic dimension generalise to multispectral images; second, we extend the methods to a different class of signals with fractional intrinsic dimension, which occur, for example, with multiple overlaid orientations and occlusions, see Figure 1.

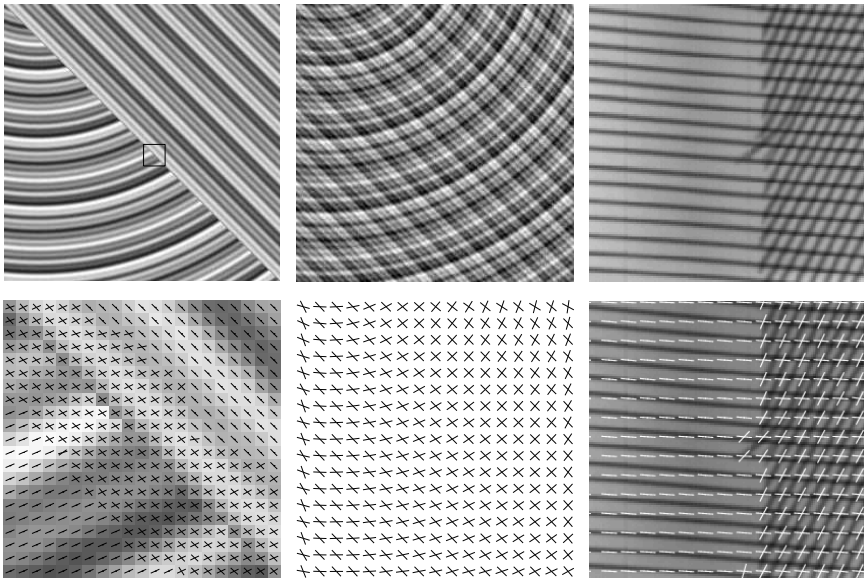


Fig. 1. Examples of images that result from combinations of locally 1D layers. Synthetic examples of occlusion (top left) and transparent overlay (top middle), and a real example of an X-ray car-tire image (top right) are shown. In the bottom row the results of estimating the orientations are shown. Results are for grey-level images and are taken from [9]. Note that in the case of multispectral images, the results will improve because the structure tensor can be built by integration in colour space instead of image space.

2 Multispectral Images and Intrinsic Dimension

Let a multispectral image be modelled by a function $\mathbf{f} : \mathbb{R}^2 \rightarrow \mathbb{R}^q$. The concept of intrinsic dimension extends straightforwardly to such images: a 0D image has constant colour; in 1D images, the colours are constant along some direction; otherwise, the image is 2D. Note that now the colours, not the grey levels, of the image must be constant in a subspace in order to have a reduced intrinsic dimension. Next, we show how to extend the three differential methods described above to the case of multispectral images. Since the coordinate system \mathbb{R}^q is mainly an artifact of the colour space definition, it seems useful to have a generalisation that does not depend on a particular choice of such a coordinate system. In particular, just working with the image components independently does not seem appropriate because they depend on the chosen colour space.

Structure Tensor. Similar to the case of scalar images, we look for the subspace E of highest dimension such that, in Ω ,

$$\frac{\partial \mathbf{f}}{\partial \mathbf{v}} = \mathbf{0} \quad \text{for all } \mathbf{v} \in E. \quad (9)$$

This leads to a system of q equations for each $\mathbf{x} \in \Omega$. Since Eq. (9) is a vectorial equation, we choose a scalar product (and its corresponding norm) in \mathbb{R}^q for $\mathbf{y} =$

(y_1, \dots, y_q) and $\mathbf{z} = (z_1, \dots, z_q)$ in \mathbb{R}^q as $\mathbf{y} \cdot \mathbf{z} = \sum_1^q a_k y_k z_k$. The positive weights a_k can emphasise some components of \mathbf{f} relative to others. We may now estimate E and the intrinsic dimension of \mathbf{f} by minimising the functional

$$\mathcal{E}(\mathbf{v}) = \int_{\Omega} \left\| \frac{\partial \mathbf{f}}{\partial \mathbf{v}} \right\|^2 d\Omega. \quad (10)$$

To find the tensor \mathbf{J} associated with \mathcal{E} , we set $\mathbf{v} = (v_x, v_y)$. Thus,

$$\frac{\partial \mathbf{f}}{\partial \mathbf{v}} = v_x \mathbf{f}_x + v_y \mathbf{f}_y, \quad (11)$$

where $\mathbf{f}_x, \mathbf{f}_y$ denote the partial derivatives of \mathbf{f} . Therefore,

$$\left\| \frac{\partial \mathbf{f}}{\partial \mathbf{v}} \right\|^2 = v_x^2 \|\mathbf{f}_x\|^2 + 2v_x v_y \mathbf{f}_x \cdot \mathbf{f}_y + v_y^2 \|\mathbf{f}_y\|^2. \quad (12)$$

Hence, Eq. (10) can be rewritten as

$$\mathcal{E}(\mathbf{v}) = \mathbf{v}^T \mathbf{J} \mathbf{v}, \quad (13)$$

where $\mathbf{J} = \mathbf{J}(\mathbf{f})$ is defined as

$$\mathbf{J} = \int_{\Omega} \begin{bmatrix} \|\mathbf{f}_x\|^2 & \mathbf{f}_x \cdot \mathbf{f}_y \\ \mathbf{f}_x \cdot \mathbf{f}_y & \|\mathbf{f}_y\|^2 \end{bmatrix} d\Omega. \quad (14)$$

Thus, as in the gray-scale case, E and the intrinsic dimension of \mathbf{f} may be estimated from the eigenvalue analysis of \mathbf{J} . Similar results have been obtained for the the gradient of colour images [10] and for motion from colour [7]. As expected, the tensor in Eq. (14) reduces to the one in Eq. (4) for gray-scale images. We relate the structure tensor of \mathbf{f} and its components by the following

Proposition 1. *Let $\mathbf{f} = (f_1, \dots, f_q)^T$, then $\mathbf{J}(\mathbf{f}) = \sum_1^q a_k \mathbf{J}(f_k)$.*

Proof. We have $\partial \mathbf{f}(\mathbf{x}) / \partial \mathbf{v} = (\nabla f_1 \cdot \mathbf{v}, \dots, \nabla f_q \cdot \mathbf{v})^T$, and consequently,

$$\left\| \frac{\partial \mathbf{f}(\mathbf{x})}{\partial \mathbf{v}} \right\|^2 = \sum_1^q a_k |\nabla f_k \cdot \mathbf{v}|^2 = \mathbf{v}^T \left(\sum_1^q a_k \nabla f_k \otimes \nabla f_k \right) \mathbf{v}, \quad (15)$$

which yields the result by use of the scalar product defined above.

The Hessian. We start by taking directional derivatives of Eq. (9) to obtain, within Ω ,

$$\frac{\partial^2 \mathbf{f}}{\partial \mathbf{w} \partial \mathbf{v}} = \mathbf{0} \quad \text{for all } \mathbf{v} \in E \text{ and } \mathbf{w} \in \mathbb{R}^2. \quad (16)$$

Let $\mathbf{H}_k = \mathbf{H}(f_k)$ be the Hessian of the component f_k , then we have

$$\frac{\partial^2 \mathbf{f}}{\partial \mathbf{w} \partial \mathbf{v}} = (\mathbf{w}^T \mathbf{H}_1 \mathbf{v}, \dots, \mathbf{w}^T \mathbf{H}_q \mathbf{v})^T. \quad (17)$$

By an abuse of notation, we denote by the Hessian of \mathbf{f} the linear mapping $\mathbf{H} : \mathbb{R}^2 \rightarrow \mathbb{R}^{2q} = \mathbb{R}^q \times \dots \times \mathbb{R}^q$ defined by

$$\mathbf{H}\mathbf{u} = (\mathbf{H}_1\mathbf{u}, \dots, \mathbf{H}_q\mathbf{u})^T. \quad (18)$$

With this notation, Eq. (16) holds if and only if

$$\mathbf{H}\mathbf{v} = \mathbf{0} \quad \text{for all } \mathbf{v} \in E. \quad (19)$$

Since the above equation is overconstrained for $q > 1$, it has to be solved in a least-squares sense, which yields E as the subspace spanned by the unity eigenvectors associated to the minimal eigenvalue of $\mathbf{H}^T\mathbf{H}$. Thus, the intrinsic dimension of \mathbf{f} may be obtained as the rank of $\mathbf{H}^T\mathbf{H}$. By choosing, in \mathbb{R}^2 , the standard scalar product and, for $\mathbf{y} = (y_1, \dots, y_q)$, $\mathbf{z} = (z_1, \dots, z_q)$ in \mathbb{R}^{2q} , the scalar product $\mathbf{y} \cdot \mathbf{z} = \sum_1^q a_k y_k \cdot z_k$, a straightforward computation gives

Proposition 2. $\mathbf{H}^T\mathbf{H} = \sum_1^q a_k \mathbf{H}^2(f_k).$

The Energy Tensor. The energy tensor method for the estimation of intrinsic dimension can be extended straightforwardly to multispectral images in analogy to the Hessian case. We define a linear mapping $\mathbf{B} : \mathbb{R}^2 \rightarrow \mathbb{R}^{2q}$ by taking into account the energy tensor for the coordinate functions of \mathbf{f} , i.e.

$$\mathbf{B}\mathbf{u} = (\mathbf{B}_1\mathbf{u}, \dots, \mathbf{B}_q\mathbf{u})^T, \quad (20)$$

where $\mathbf{B}_k = \mathbf{B}(f_k) = \nabla f_k \otimes \nabla f_k - f_k \mathbf{H}(f_k)$. Therefore, the subspace E is the kernel of \mathbf{B} , i.e.

$$\mathbf{B}\mathbf{v} = \mathbf{0} \quad \text{for all } \mathbf{v} \in E. \quad (21)$$

Thus, again, E is estimated as the eigenspace associated to the minimal eigenvalue of $\mathbf{B}^T\mathbf{B}$, and the intrinsic dimension of \mathbf{f} is computed as the rank of $\mathbf{B}^T\mathbf{B}$. As before, we have the following

Proposition 3. $\mathbf{B}^T\mathbf{B} = \sum_1^q a_k \mathbf{B}^2(f_k).$

3 Intrinsic Dimension of Multiple, Multispectral Layers

In this section, we investigate a special class of 2D images which occur when two 1D layers are combined into one 2D image, e.g. by additive superposition or occlusion. We will show that a generalised structure tensor can be used to detect such superpositions and to estimate the parameters of the 1D layers. Because such combinations of 1D layers have an intrinsic dimension greater than one, but are not really 2D, we say that they have a *fractional intrinsic dimension* between 1 and 2 and, thus, need a more refined description (in terms of the generalised structure tensor introduced below).

Pattern	rank \mathbf{J}	rank \mathbf{J}_2
○	0	0
	1	1
+	2	2
others	2	3

Table 1. The shown correspondences between the different patterns and the ranks of the two tensors define the intrinsic dimension of the components of additively overlaid images. The symbols denote $0D$ (circle) and $1D$ (bar) patterns. In general, the rank of \mathbf{J}_N , $N = 1, 2, \dots$ induces a natural order of complexity for patterns consisting of N additive layers [11].

Additive Multispectral Layers. Let \mathbf{f} be the additive superposition of two layers

$$\mathbf{f} = \mathbf{g} + \mathbf{h}, \quad (22)$$

we want to know if both layers \mathbf{g}, \mathbf{h} have intrinsic dimension lower than two, i.e., for a given region Ω , we want to know if there are subspaces E_1 and E_2 such that

$$\frac{\partial \mathbf{g}}{\partial \mathbf{u}} = \frac{\partial \mathbf{h}}{\partial \mathbf{v}} = \mathbf{0} \quad \text{for all } \mathbf{u} \in E_1, \mathbf{v} \in E_2. \quad (23)$$

By allowing more layers, we can deal with the important case where the components f_k of \mathbf{f} have intrinsic dimension lower than 2. For this, it suffices to look at $\mathbf{f} = \sum_1^q f_k \mathbf{e}_k$, where $\{\mathbf{e}_1, \dots, \mathbf{e}_k\}$ is the standard basis for \mathbb{R}^q . Taken together, Eq.s (22) and (23) are equivalent to [12]

$$\frac{\partial^2 \mathbf{f}}{\partial \mathbf{u} \partial \mathbf{v}} = \mathbf{u}^T \mathbf{H} \mathbf{v} = \mathbf{0}, \quad (24)$$

which expands to

$$c_{xx} \mathbf{f}_{xx} + c_{xy} \mathbf{f}_{xy} + c_{yy} \mathbf{f}_{yy} = \mathbf{0}, \quad (25)$$

where $c_{xx} = u_x v_x$, $c_{xy} = u_x v_y + u_y v_x$, $c_{yy} = u_y v_y$. Since the above equation is linear in the parameter vector $\mathbf{c} = (c_{xx}, c_{xy}, c_{yy})^T$, there will be a correspondence between the dimension of the subspaces E_1, E_2 and the rank of the tensor associated to the energy functional (see [11] and Table 1)

$$\mathcal{E}_2(\mathbf{c}) = \int_{\Omega} \|c_{xx} \mathbf{f}_{xx} + c_{xy} \mathbf{f}_{xy} + c_{yy} \mathbf{f}_{yy}\|^2 d\Omega = \mathbf{c}^T \mathbf{J}_2 \mathbf{c}, \quad (26)$$

where $\mathbf{J}_2 = \mathbf{J}_2(\mathbf{f})$ is given by

$$\mathbf{J}_2 = \int_{\Omega} \begin{bmatrix} \|\mathbf{f}_{xx}\|^2 & \mathbf{f}_{xx} \cdot \mathbf{f}_{xy} & \mathbf{f}_{xx} \cdot \mathbf{f}_{yy} \\ \mathbf{f}_{xx} \cdot \mathbf{f}_{xy} & \|\mathbf{f}_{xy}\|^2 & \mathbf{f}_{xy} \cdot \mathbf{f}_{yy} \\ \mathbf{f}_{xx} \cdot \mathbf{f}_{yy} & \mathbf{f}_{xy} \cdot \mathbf{f}_{yy} & \|\mathbf{f}_{yy}\|^2 \end{bmatrix} d\Omega. \quad (27)$$

Multiplicative Multispectral Layers. We now consider the multiplicative superposition of two layers, i.e.

$$\mathbf{f} = \mathbf{g} \bullet \mathbf{h}, \quad (28)$$

where the bullet denotes that for every component of \mathbf{f} , we have $f_k = g_k h_k$. A direct verification shows that Eq.s (23) and (28) imply the following constraint for \mathbf{f} :

$$\mathbf{u}^T \mathbf{B} \mathbf{v} = \mathbf{0}. \quad (29)$$

In analogy to the additive case, we can construct a tensor $\mathbf{J}(\mathbf{B}, \mathbf{f})$ for the estimation of the intrinsic dimension of the layers.

Occluded Multispectral Layers. We model occluded superposition of two images by

$$\mathbf{f} = \chi \mathbf{g} + (1 - \chi) \mathbf{h} , \quad (30)$$

where $\chi(\mathbf{x})$ is the characteristic function of some half-plane P . This model is appropriate for the local description of junction types T , L and Ψ . X -junctions fit better to a transparent model as in Subsection 3. In order to estimate the intrinsic dimension of the occlusion layers, we observe that Eq. (30) is equivalent to

$$\mathbf{f}(\mathbf{x}) = \begin{cases} \mathbf{g}_1(\mathbf{x}) & \text{if } \mathbf{x} \in P \\ \mathbf{g}_2(\mathbf{x}) & \text{otherwise.} \end{cases} \quad (31)$$

Therefore, $\partial \mathbf{f}(\mathbf{x}) / \partial \mathbf{u} = \mathbf{0}$ if \mathbf{x} belongs to P , and $\partial \mathbf{f}(\mathbf{x}) / \partial \mathbf{v} = \mathbf{0}$ if \mathbf{x} does not belong to P . From the above, we can draw the conclusion that the expressions

$$\frac{\partial \mathbf{f}}{\partial \mathbf{u}} \otimes \frac{\partial \mathbf{f}}{\partial \mathbf{v}} = \mathbf{0} \quad \text{and} \quad \frac{\partial \mathbf{f}}{\partial \mathbf{v}} \otimes \frac{\partial \mathbf{f}}{\partial \mathbf{u}} = \mathbf{0} \quad (32)$$

are valid everywhere except for the border of P where they may differ from zero. Eq. (32) may not hold at the border of P , because the derivatives of the characteristic function χ are not defined there. This is not the case if \mathbf{u} and the border of P have the same direction, e.g., in case of a T -junction. In contrast to the second order derivative approach, the equations in (32) differ. Expanding the first of these equations, we find

$$u_x v_x \mathbf{f}_x \otimes \mathbf{f}_x + u_x v_y \mathbf{f}_x \otimes \mathbf{f}_y + u_y v_x \mathbf{f}_y \otimes \mathbf{f}_x + u_y v_y \mathbf{f}_y \otimes \mathbf{f}_y = \mathbf{0} . \quad (33)$$

A direct estimation of the $u_i v_j$ will result in an overconstrained system of equations for \mathbf{u} and \mathbf{v} . This is avoided by averaging the equations in (32), i.e., by symmetrization, to obtain

$$c_{xx} \mathbf{f}_x \otimes \mathbf{f}_x + \frac{c_{xy}}{2} (\mathbf{f}_x \otimes \mathbf{f}_y + \mathbf{f}_y \otimes \mathbf{f}_x) + c_{yy} \mathbf{f}_y \otimes \mathbf{f}_y = \mathbf{0} . \quad (34)$$

Although the focus here is not on the estimation of the parameters \mathbf{u} and \mathbf{v} , the symmetrization has the extra benefit of reducing the size of the resulting tensor. The system in Eq. (34) has $q(q+1)/2$ equations, which makes the system overconstrained if $q > 2$. Note that the system is underconstrained for $q = 1$ and that a multispectral approach can overcome this problem. As in the case of transparent layers, a least-squares procedure to solve Eq. (34) will lead to the minima of the energy functional

$$\begin{aligned} \mathcal{E}(\mathbf{c}) &= \int_{\Omega} \|c_{xx} \mathbf{f}_x \otimes \mathbf{f}_x + \frac{c_{xy}}{2} (\mathbf{f}_x \otimes \mathbf{f}_y + \mathbf{f}_y \otimes \mathbf{f}_x) + c_{yy} \mathbf{f}_y \otimes \mathbf{f}_y\|^2 d\Omega \\ &= \mathbf{c} \mathbf{J}_2 \mathbf{c} , \end{aligned} \quad (35)$$

where

$$\mathbf{J}_2 = \int_{\Omega} \begin{bmatrix} \|\mathbf{f}_x\|^4 & & \|\mathbf{f}_x\|^2 \mathbf{f}_x \cdot \mathbf{f}_y & \|\mathbf{f}_x \cdot \mathbf{f}_y\|^2 \\ \|\mathbf{f}_x\|^2 \mathbf{f}_x \cdot \mathbf{f}_y & \frac{1}{2} (\|\mathbf{f}_x\|^2 \|\mathbf{f}_y\|^2 + |\mathbf{f}_x \cdot \mathbf{f}_y|^2) & & \|\mathbf{f}_y\|^2 \mathbf{f}_x \cdot \mathbf{f}_y \\ \|\mathbf{f}_x \cdot \mathbf{f}_y\|^2 & & \|\mathbf{f}_y\|^2 \mathbf{f}_x \cdot \mathbf{f}_y & \|\mathbf{f}_y\|^4 \end{bmatrix} d\Omega . \quad (37)$$

As before, a correspondence between the intrinsic dimension of the occlusion layers and the rank of \mathbf{J}_2 is given by Table 1.

4 Discussion

We have addressed the basic question of how to encode local signal variation in the case of multispectral images. The results remain valid for any vector-valued two-dimensional signal and can be extended to n -dimensional signals [9]. We have shown how the concept of intrinsic dimension and the estimation of multiple orientations can be applied to multispectral images in a way which does not depend on the chosen colour space. We expect this to be useful for those who work with multispectral images and need to extract meaningful features, compress, or denoise such images. Moreover, we expect that some may choose to use multispectral images to improve the results obtained with scalar images. This is because our results show how multiple spectral components, if they differ, can help to estimate significant image features like orientations, corners, and junctions. The estimation of local structure always requires a certain neighbourhood and multispectral images offer the possibility to trade spatial against spectral neighbourhoods. Our methods are based on derivatives, but we have discussed elsewhere, e.g. in [6, 4], that this is not a serious practical restriction. Nevertheless, a more general non-differential theory remains desirable.

References

1. Zetsche, C., Barth, E.: Fundamental limits of linear filters in the visual processing of two-dimensional signals. *Vision Research* **30** (1990) 1111–7
2. Zetsche, C., Barth, E., Wegmann, B.: The importance of intrinsically two-dimensional image features in biological vision and picture coding. In Watson, A.B., ed.: *Digital Images and Human Vision*. MIT Press (1993) 109–38
3. Mota, C., Barth, E.: On the uniqueness of curvature features. In Baratoff, G., Neumann, H., eds.: *Dynamische Perzeption*. Volume 9 of *Proceedings in Artificial Intelligence*., Köln, Infix Verlag (2000) 175–8
4. Mota, C., Aach, T., Stuke, I., Barth, E.: Estimation of multiple orientations in multi-dimensional signals. In: *IEEE Int. Con. Image Processing*. (2004) 2665–2668
5. Krieger, G., Zetsche, C., Barth, E.: Nonlinear image operators for the detection of local intrinsic dimensionality. In: *Proc. IEEE Workshop Nonlinear Signal and Image Processing*. (1995) 182–185
6. Mota, C., Stuke, I., Barth, E.: Analytic solutions for multiple motions. In: *Proc. IEEE Int. Conf. Image Processing*. Volume II., IEEE Signal Processing Soc. (2001) 917–20
7. Golland, P., Bruckstein, A.M.: Motion from color. *Computer Vision and Image Understanding* **68**(3) (1997) 346–62
8. Felsberg, M., Granlund, G.: POI detection using channel clustering and the 2D energy tensor. In: *Pattern Recognition: 26th DAGM Symposium*. Volume 3175 of *LNCS*., Tübingen, Germany, Springer Berlin (2004) 103–110
9. Stuke, I., Barth, E., Mota, C.: Estimation of multiple orientations and multiple motions in multi-dimensional signals. In: *Brazilian Symposium on Computer Graphics and Image Processing*, IEEE Computer Society Press (2006) in press
10. Di Zenzo, S.: A note on the gradient of a multi-image. *Computer Vision, Graphics, and Image Processing* **33** (1986) 116–25
11. Mota, C., Dorr, M., Stuke, I., Barth, E.: Categorization of transparent-motion patterns using the projective plane. *Int. J. of Computer & Information Science* **5**(2) (2004) 129–40
12. Aach, T., I, S., Mota, C., Barth, E.: Estimation of multiple local orientations in image signals. In: *Proc. IEEE Int. Conf. Acoustics, Speech, and Signal Processing*. (2004) 553–556